UNIVERSITÉ DU LUXEMBOURG

PhD-FSTC-2014-46

The Faculty of Sciences, Technology and Communication

DISSERTATION

Presented on 22/12/2014 in Luxembourg
to obtain the degree of

DOCTEUR DE L'UNIVERSITÉ DU LUXEMBOURG

EN PHYSIQUE

by

Muhammad ANWAR

Born on 17th September 1983 in Sargodha, Pakistan

COMPUTER SIMULATIONS OF CRYSTALLIZATION MECHANISM IN POLYMERIC MATERIALS

Dissertation defense committee:

Dr. Tanja Schilling, Dissertation supervisor
Professor, Université du Luxembourg, Luxembourg
Dr. Roland Sanctuary, Chairman
Professor, Université du Luxembourg, Luxembourg
Dr. Massimo Malvetti, Vice chairman
Professor, Université du Luxembourg, Luxembourg
Dr. Chritian Wagner
Professor, Universität des Saarlandes, Saarbrücken, Germany
Dr. René Messina
Professor, Université de Lorraine, Metz, France

Abstract

In this work, we have studied crystallization in short polymer chains using molecular dynamics simulations. We use a realistic united atom model which is able to reproduce the physical quantities related to phase transitions. We present a study of crystal nucleation from undercooled melts of n-alkanes and identify the molecular mechanism of homogeneous crystal nucleation under quiescent conditions and under shear flow. We choose n-eicosane (C20) the length of which is below the entanglement length and n-pentacontahectane (C150) the length of which is above the entanglement length so that we can compare results for unentangled and entangled polymer chains. We also provide the crystal growth mechanism of n-eicosane under quiescent conditions. For C150, we present crystal lamellae structure and compare our results with published simulation results. We use a mean first passage time analysis and a committor analysis to determine the critical nucleus size and then to compute the nucleation rate. We observe that the critical nucleus is of cylindrical shape. We report on the effects of shear rate and temperature on the nucleation rates and estimate the critical shear rates, beyond which the nucleation rate increases with the shear rate. We show that the critical shear rate corresponds to a Weissenberg number of order unity which is in agreement with previous experimental observation and theoretical work. We also show that the power law behaviour between nucleation rate and shear rate is in agreement with experiments and theory. We compute the viscosity of the system during the formation of crystalline nuclei and we show that the viscosity of the system is not affected by the crystalline nuclei. Finally, we present results of crystallization in the polyethylene (C500) melt under quiescent conditions [1].

[1] Main results of this work published in the following articles:
- The Journal of Chemical Physics, 139, 214904 (2013).
- The Journal of Chemical Physics, 141, 124910 (2014).

Contents

Abstract i

1 Introduction 1

2 Methodology 8
2.1 Molecular dynamics simulations . . . 9
2.1.1 Force calculation . . . 11
2.1.2 Integrating the equations of motion . . . 12
2.1.3 Thermostat and barostat . . . 14
2.1.4 Periodic boundary conditions . . . 15
2.2 Model . . . 17
2.3 Order parameters . . . 19
2.3.1 Local density . . . 19
2.3.2 Radius of gyration . . . 19
2.3.3 Nematic order parameter . . . 20
2.3.4 Crystallinity order parameter . . . 21
2.3.5 Bond order parameter . . . 22
2.3.6 Trans states . . . 23
2.4 Critical nucleus size . . . 24
2.4.1 Mean first passage time analysis . . . 24
2.4.2 Committor analysis . . . 25
2.5 Classical nucleation theory . . . 26
2.6 Crystallization in polymers . . . 29

3 Crystallization of n-Eicosane under Quiescent Conditions 33
3.1 Introduction . . . 34
3.2 Model & order parameters . . . 36
3.3 Thermostat and barostat . . . 37
3.4 Simulation details . . . 40
3.5 Results & discussion . . . 41
3.5.1 Nucleation rates . . . 41
3.5.2 Nucleation mechanism . . . 47

3.5.3 Growth mechanism 49
3.6 Conclusions 56

4 Crystal Nucleation of *n*-Eicosane under Shear Flow 57
4.1 Introduction 58
4.2 Molecular dynamics simulations under flow 59
4.3 Thermostatting 62
4.4 Simulation details 64
4.5 Results & discussion 66
4.5.1 Velocity profile 66
4.5.2 Nucleation rates 67
4.5.3 Nucleation mechanism 71
4.5.4 Shear viscosity 75
4.6 Conclusions 77

5 Crystallization of C150 & Polyethylene 78
5.1 Introduction 79
5.2 Model & order parameters 82
5.3 C150 under quiescent conditions 83
5.3.1 Simulation details 83
5.3.2 Results & discussion 83
5.4 C150 under shear flow 94
5.4.1 Simulation details 94
5.4.2 Results & discussion 94
5.4.3 Shear viscosity 98
5.5 Crystallization of polyethylene (C500) 101
5.5.1 Simulation details 101
5.5.2 Results & discussion 101
5.6 Conclusions 105

6 Conclusions 106

Bibliography 108

Chapter 1

Introduction

Every one of us comes in contact with polymer materials on a daily basis. It could be in the form of a plastic bag, an adhesive tape or a drink bottle. Polymers are long chain molecules consisting of a number of monomer units ranging from 1000 to 100000. They exhibit a large number of properties due to constituent variety and their architecture. Mechanical properties are among the most important aspects of polymer materials. It could be the elasticity of rubber; the toughness and the ductility of semicrystalline polymers, glass polymers or blends; or the strength of oriented semicrystalline polymers. When these mechanical properties are combined with light weight and processibility, the polymeric materials become an attractive choice for use in structural applications. The rheological properties of polymers play a paramount role in designing of processing operations such as extrusion, blow molding, and film blowing. Apart from these, they also have unique chemical, optical and electronic properties [1].

As human history is divided into era by the name of primary material used i.e. the Stone, Bronze and Iron ages, Rubinstein and Colby [2] referred to the twentieth century as the Polymer age. In the middle of nineteenth century, chemists started synthetic polymerization but they did not believe that they were producing the large macromolecules. Until the beginning of the nineteenth century macromolecules were believed to form a colloidal globule. In 1920, Staudinger proposed the macromolecular hypothesis. In his view polymers are large molecules consisting of basic units called monomers and colloidal properties are attributed to the size

of these large molecules. In the beginning, this hypothesis faced a lot of resistance. Carothers had produced different polymers till 1929 and the Polymer era started. From 1930 to 1960, the main concepts of polymer science were introduced including synthesis methods and the foundation of polymer physics. In the next 20 years the principles of modern polymer physics were established including Edwards model for the chain and its confinement [2].

Semicrystalline polymers are widely used due to their favorable mechanical properties. These mechanical properties depend on the morphology, which is linked to crystallization of the polymers [3]. The crystallization process in polymers is divided into two steps, nucleation and growth. Like monatomic systems, when a melt of polymer is cooled below its crystal-liquid coexistence temperature, small crystallites are formed. These crystallites are formed from local density and/or orientational fluctuations and they further grow to form big crystal structures. The mechanical properties of the solidified materials strongly depend on the sizes, the shapes and the distribution of these initially formed crystallites.

In spite of intensive research efforts since the early 1940s, the molecular mechanism of polymer crystallization is still not completely understood [4]. Experimental research has been carried out using a wide range of techniques both on polymers under quiescent conditions [5–14] and in external fields [15–22]. Crystallization rates and critical shear rates have been measured for different polymeric materials, the morphological features of the final crystal structure and the effect of molecular weight on the crystallization kinetics have been studied. The primary nucleation mechanism has not however been identified, because the short length- and time-scales on which it takes place are difficult to access experimentally [1].

In the early studies of polymer crystallization, the Bragg peaks were observed after the induction period in wide angle X-ray scattering(WAXS). No small angle X-ray scattering(SAXS) peak was expected before the Bragg peak. But in 1990's SAXS peaks were reported in many experiments during the induction period before the appearance of the Bragg peaks [5–7]. These SAXS peaks were claimed to be due to the presence of ordered melt before the occurrence of a nucleation event. These results were interpreted using Cahn-Hilliards(CH) theory [23]. This theory takes

[1] This paragraph is published in The Journal of Chemical Physics, 141, 124910 (2014).

only one order parameter into account and according to this theory the SAXS peaks are due to spinodal decomposition. Many theories have been proposed to explain these SAXS peaks. Doi et al. [24, 25] proposed the theory of microphase separation for polymer crystallization. Olmsted and co-workers [26] reported a theory based on spinodal decomposition of the polymer melt to explain the emergence of these SAXS peaks before the emergence of WAXS peak. Kaji [27] proposed a model for polymer crystallization based on Doi [24, 25] theory and Olmsted [26] theory to explain these SAXS peaks. Once a stable nucleus is formed, then the new chains (from melt) come to the growth front to get attach to this crystal structure. This process of attachment of polymer chains at the growth front is a complex process due to involvement of polymer diffusion, entanglement effects, transition from random coil conformation to extended or folded crystal structure and competitive absorptions and desorption at the growth front [4]. The first theory of growth of crystals was described by Lauritzen and Hoffman (LH) [28], sometimes referred as surface nucleation approach. The second theory was presented by Sadler and Gilmer (SG) [29]. Recently, Strobl [10] proposed a new route to crystallization of entangled polymer melt based on multi-stage ordering of the molecules.

The study of polymer crystallization is an attractive topic due to its wide range of industrial applications. In industry, polymer melts usually flow during processing operations. Flow can change crystal nucleation and growth mechanisms and hence can change the material properties. Therefore, technologically it would be of great importance to understand the crystal nucleation and growth processes under flow.

As the molecular length- and time-scales involved in nucleation and growth processes are below experimental resolution, and a theoretical approach is challenging because of the full non-equilibrium nature of the problem, computer simulations are a promising alternative method to solve the problem. McLeish, Olmsted and co-workers have over the past 15 years developed a comprehensive set of theoretical and computer simulation techniques and experimental model systems to study polymers under flow. To address crystallization they derived a kinetic Monte Carlo algorithm on the basis of kinetics extracted from the GLaMM model [30], embedded it in a Brownian dynamics simulation [31, 32] and extended this approach by a fast nucleation algorithm to compute nucleation rates [33]. This model captures many features of flow induced crystallization, however, parts of it are based on an effective

free energy picture i.e. on the assumption of separating relaxation time-scales and thus quasi-equilibrium [1].

Atomistic computer simulations have been used to study polymer crystallization under quiescent conditions [34–57] and under flow or large deformation [3, 58–65]. Most of these studies focus on the growth process rather than the nucleation process, because nucleation is by definition a rare event (an event that occurs on a time-scale much larger than the time-scale of the local dynamics) and therefore difficult to tackle by atomistic simulation. Nucleation in short chain alkanes under quiescent conditions has nevertheless been simulated [34–39, 41, 42] and a scenario for the nucleation mechanism has been identified. The first direct computation of homogeneous nucleation rates in long chain alkanes by means of computer simulation has recently been presented by Rutledge and co-workers [40]. Their work was focused on the nucleation and growth rates and the free energy landscape associated with the crystallization process rather than the microscopic mechanisms [1].

There are still several questions which are open or controversial in the context of polymer crystallization. These questions need to be addressed to establish complete understanding of the crystallization mechanism on a microscopic level. These questions include [66, 67]:

- Under what conditions do polymers nucleate? In the undercooled melt, it is not clear if density fluctuations induce orientation of segments of polymer chains or if the orientation of segments of polymer chains produce density fluctuations on local level and then crystallization starts. The determination of these conditions can allow one to control the start of crystallization, which consequently can provide the possibility to control the macroscopic properties of the material.

- The growth mechanism on a microscopic level is not yet understood completely. Three different theories have been proposed to describe the growth mechanism [10, 28, 29] but recent results from simulations [43, 48] do not agree with them. The factors behind spontaneous selection of lamellae thickness need to be identified. The consequences of entanglements on the nucleation and growth are also not fully understood. An explicit consideration is

required to address the regions between the purely crystalline and the purely amorphous regions.

- Most of the polymers are of semicrystalline nature, thus are non equilibrium structures. Even well below melting temperatures, relaxation leads to rearrangements and mobility of chains which subsequently change the crystal morphology. In such circumstances, are the concepts of equilibrium thermodynamics for melting and crystallization sufficient to describe the polymer crystals which are of metastable nature? One of the controversial issues [68] is whether the semi-crystal structures are thermodynamically favorable structures with global free energy minimum or if they are kinetically manifested structures and can form purely crystalline structure if enough time is given.

- How do external fields influence the polymer crystallization? Under shear conditions, shish kebab like structures are formed but the mechanism of formation of the structure is not understood yet. What are the combined effects of flow and temperature on the crystallization kinetics and what are the effects of flow on the entanglements during crystallization?

- Another important task is to identify new order parameters besides lamellae thickness, growth rates and degree of crystallinity so that polymer crystals can be characterized in a better way and some ambiguities which arise from measurements of existing order parameters like degree of crystallinity can be eliminated.

The main purpose of this work is to improve the understanding of the polymer crystallization on a microscopic level. We would particularly like to answer the following questions using molecular dynamics simulation methods:

- To sample the induction times for short chain alkanes (chains shorter than the entanglement length) and identify the molecular mechanism of nucleation and growth under quiescent conditions.

- To report on the effect of the flow and temperature on the induction times and compare these results with already available theories and experiments for short chain alkanes, then to identify the molecular mechanism of nucleation

at different shear rates and the response of the system to the formation of small clusters in terms of shear viscosity.

- To sample the induction times for long chain alkanes (chains longer than the entanglement length) and to identify the molecular mechanism of nucleation and some features related to the structure of lamellae under quiescent conditions.

- To report on the effect of the flow on the induction times and compare these results with already available theories and experiments for long chain alkanes. Then to identify the molecular mechanism of nucleation at different shear rates and the response of the system to the formation of small clusters in terms of shear viscosity.

- Validation of our results with already published simulation and experimental results. Recently, Rutledge [38–40] and his co-workers performed simulations to study the nucleation in n-alkanes and Coppola and his co-workers [19] performed experiments and reported the effects of flow and temperature on the induction time so we would like to compare our results with theirs.

We will use a united atom model introduced by the Paul et al. [69] and later on modified by Waheed et al. [70] to address the above mentioned questions. This model is able to reproduce the dynamical and structural properties, melting point and rotator phase. It has also been used for studying the crystallization of polymer melts [38–40]. We will use the ESPResSo [71] molecular dynamics simulation package to simulate the system, and implement the missing routines needed to study the crystallization mechanism. All computer simulations for this work will be carried out on the HPC facility of the University of Luxembourg [72]. This project has been financially supported by the National Research Fund (FNR) within the CORE project Polyshear.

This thesis is organized into five chapters. In chapter 2, we describe the fundamental components of the molecular dynamics simulations, the simulation model, the order parameters and the classical nucleation theory. In chapter 3, we address

the nucleation and growth mechanism on a molecular level in short chain alkanes *n*-eicosane (C20) under quiescent conditions[2]. In chapter 4, we report the effect of flow and temperature on the nucleation times and identify the microscopic mechanism at different shear rates and measure the response of the system to the formation of small clusters in terms of shear viscosity[3]. In chapter 5, we provide the induction time for long chain alkanes and identify the microscopic mechanism of nucleation under quiescent conditions. We also show the effect of flow on the nucleation times and identify the microscopic mechanism at different shear rates and measure the response of the system to the formation of small clusters in terms of shear viscosity[3]. In chapter 6, we present the conclusions of our work and some suggestions for future work to improve the understanding of polymer crystallization.

[2]Main results of this chapter published in The Journal of Chemical Physics, 139, 214904 (2013).
[3]Main results of this chapter published in The Journal of Chemical Physics, 141, 124910 (2014).

Chapter 2

Methodology

This chapter starts with a brief introduction to molecular dynamics simulation techniques. A detailed description of the simulation model which we use in this study is provided. Then, several order parameters are explained which we use to monitor the nucleation event and the growth of clusters. Next we discuss classical nucleation theory. Different methods to compute the critical nucleus size are presented. At the end of this chapter, we explain how nucleation in polymers is different from nucleation in small molecules and provide different theories which explain the growth mechanism in polymers.

2.1 Molecular dynamics simulations

Molecular dynamics simulation is one of the most widely used techniques in the statistical mechanics community to study many body systems on a microscopic level. This technique was introduced by Alder and Wainwright [73, 74]. They used it to study the phase transition in hard spheres. Subsequently, Stillinger and Rahman [75, 76] performed simulations to study liquid argon and water. In last few decades, due to advancements in computer technology and improvements in algorithms, it has become a powerful tool to study the dynamics and structure of different complex system in many areas of science and engineering [77].

The contents of this section are mostly based on the Frenkel and Smit's book "Understanding Molecular Simulation - From Alogorithms to Applications" [78]. Molecular dynamics simulation is based on the assumption that classical mechanics can be used to describe the motions of atoms and the molecules. The laws of classical mechanics are used to generate trajectories giving the microscopic information of the system in terms of the coordinates and momenta which are sufficient to describe the motion of any classical many body system. Then this microscopic information is used to compute the macroscopic properties of interest using the rules of classical statistical mechanics.

In statistical mechanics, usually we are interested in ensemble averages, which is an average over all accessible micro-states in the 6N dimensional phase space for a given set of macroscopic properties. For a system consisting of N particles, at fixed volume and at constant temperature T, the ensemble average can be computed using;

$$\langle A \rangle_{ensemble} = \frac{\iint \mathrm{d}\mathbf{r}^N \mathrm{d}\mathbf{p}^N A\left(\mathbf{r}^N, \mathbf{p}^N\right) \exp\left(\frac{-H\left(\mathbf{r}^N, \mathbf{p}^N\right)}{k_B T}\right)}{\iint \mathrm{d}\mathbf{r}^N \mathrm{d}\mathbf{p}^N \exp\left(\frac{-H(\mathbf{r}^N, \mathbf{p}^N)}{k_B T}\right)} \tag{2.1}$$

Here $A(\mathbf{r}^N, \mathbf{p}^N)$ is the macroscopic observable which is function of $\mathbf{r}$ and $\mathbf{p}$, $\mathbf{r}$ is the coordinates, $\mathbf{p}$ is momenta of particles, k_B is Boltzmann constant and H is the Hamiltonian of the system which is the sum of kinetic and potential energy of the system. The term in the denominator is referred to as the partition function which

is the sum over all possible micro-states that a system can have for a given set of macroscopic properties, and is typically very difficult to calculate analytically. In most experiments, we measure quantities of interest during a certain interval of time and compute their averages. In molecular dynamics simulations, we study an average behavior of a many body system by computing the time evolution of the system using Newtons equations of motion and average them over sufficiently long times. To compare the ensemble averages with time averages, we define the ergodic hypothesis. This hypothesis states that for a given set of macroscopic properties, if we allow a system to evolve in time for an infinite time so that it can visit all points in the ensemble then the ensemble averages are equal to the time averages. In analyzing molecular dynamics simulations we often assume that we have generated a trajectory for an infinite time and the system has visited all possible micro-states consistent with given macroscopic properties. In this case we can write:

$$\langle A \rangle_{ensemble} = \langle A \rangle_{time} = \lim_{\tau \to \infty} \frac{1}{\tau} \int_{t=0}^{\tau} A\left(\mathbf{r}^N(t), \mathbf{p}^N(t)\right) \, \mathrm{d}t \approx \frac{1}{M} \sum_{t=1}^{M} A\left(\mathbf{r}^N, \mathbf{p}^N\right) \tag{2.2}$$

Here τ is the simulation time and M is the number of time steps.

The advantage of molecular dynamics simulation over other equilibrium methods such as the Monte Carlo technique is that it can be used to study the transport properties of the system along with the equilibrium properties. It provides the dynamics of the system and is similar to real experiments in many aspects.

A simple program for molecular dynamics simulation can be written as:

- Choose the parameters that specify the conditions of run(e.g., initial temperature, number of particles, time-step etc.).
- Define initial positions and velocities.
- Compute forces on all particles.
- Integrate Newtons equations of motion to evolve the system in time.
- Analyze the data, compute the average quantities and stop the program.

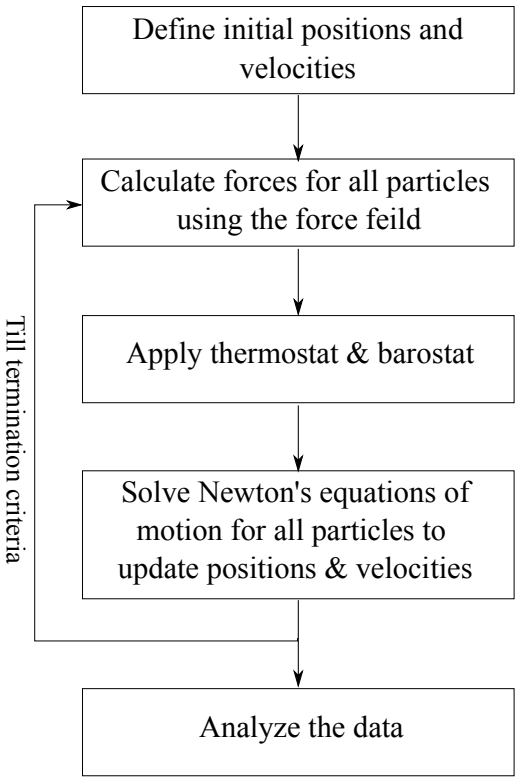

FIGURE 2.1: Schematic of molecular dynamics simulations.

This is shown schematically in FIG. 2.1. Now we discuss few important components of molecular dynamics.

2.1.1 Force calculation

In molecular dynamics simulations, we compute force for every particle at every timestep using:

$$m\ddot{\mathbf{r}}_i = \mathbf{f}_i; \quad \mathbf{f}_i = - \bigtriangledown U_i(r^N) = -\frac{\partial}{\partial \mathbf{r}_i} U(\mathbf{r}^N) \tag{2.3}$$

m is the mass of particle, $\ddot{\mathbf{r}}_i$ is the acceleration of the particle i, $\mathbf{f}_i$ is the force on the particle i, $\bigtriangledown$ is the gradient, $\mathbf{r}_i$ is the position of the particle i and U is the potential energy. This is the most time consuming part of almost all molecular dynamics simulations. If we consider a simple example of pairwise additive interaction like a Lennard Jones system, the simulation time needed would be scaled to square of the number of particles (i.e. $O(N^2)$). We can reduce this simulation time by

computing the interactions only between nearby pairs of particles. When pairwise separation(r_{ij}) between interacting particle i and j is large, the force converges to zero and we do not compute forces between particles for which $r_{ij} > r_c$, where r_c is the potential cutoff radius. The simulation time needed to compute the force can further be reduced by creating the lists of nearby pairs of particles efficiently. We list three methods which are frequently used to identify the neighbors of particles:

- Verlet neighbor list
- Cell list
- Combination of Verlet list and cell list

In the Verlet neighbor list, the simulation time scales to square of the number of particles ($O(N^2)$) and in the cell list and in the combined method, the simulation time scales to the number of particles ($O(N)$).

2.1.2 Integrating the equations of motion

After computing the forces between particles, we can now integrate the equations of motion to get the time evolution of the particles. There are several numerical algorithms which are used to integrate the Newton's equations of motion. All algorithms use finite difference methods for integration of these equations. The positions, the velocities and the accelerations of particles are approximated using Taylor series expansion. Accuracy, efficiency, conservation of physical law (e.g time reversal, conservation of energy and momentum etc.) and stability are desirable properties of the integrators.

Verlet algorithm - In the Verlet algorithm [79], we compute position of particles at every time step. By expanding the position $\mathbf{r}(t)$ forward and backward in time using a Taylor series:

$$\mathbf{r}(t + \triangle t) = \mathbf{r}(t) + \mathbf{v}(t) \cdot \triangle t + \frac{1}{2}\mathbf{a}(t) \cdot \triangle t^2 + \frac{1}{6}\mathbf{b}(t) \cdot \triangle t^3 + O(\triangle t^4) \tag{2.4}$$

$$\mathbf{r}(t - \triangle t) = \mathbf{r}(t) - \mathbf{v}(t) \cdot \triangle t + \frac{1}{2}\mathbf{a}(t) \cdot \triangle t^2 - \frac{1}{6}\mathbf{b}(t) \cdot \triangle t^3 + O(\triangle t^4) \tag{2.5}$$

Subtracting equation 2.5 from equation 2.4, we get;

$$\mathbf{r}(t+\triangle t) = 2\cdot\mathbf{r}(t) + \mathbf{r}(t-\triangle t) + \mathbf{a}(t)\cdot\triangle t^2 + O(\triangle t^4) \tag{2.6}$$

Where **r** is the position of particle, **v** is the velocity of particle, **a** is the acceleration of particle and **b** is the third derivative of the position of particle. In this algorithm the velocities are not computed directly however they can be computed using the positions of particles and the timestep as follow;

$$\mathbf{v}(t) = \frac{\mathbf{r}(t+\triangle t) - \mathbf{r}(t-\triangle t)}{2\cdot\triangle t} \tag{2.7}$$

Leap Frog algorithm - The Leap Frog algorithm [80] is a modified version of the Verlet algorithm. In this algorithm, positions and velocities are not computed at the same time so kinetic and potential energies can not be computed at same time. The velocities are computed at half time step then the positions are computed at next time step. Mathematically,

$$\mathbf{v}\left(t+\frac{1}{2}\triangle t\right) = \mathbf{v}\left(t-\frac{1}{2}\triangle t\right) + \mathbf{a}(t)\cdot\triangle t \tag{2.8}$$

$$\mathbf{r}(t+\triangle t) = \mathbf{r}(t) + \triangle t\cdot\mathbf{v}\left(t+\frac{1}{2}\triangle t\right) \tag{2.9}$$

Velocity Verlet algorithm - In the velocity Verlet algorithm [81] positions, velocities and acceleration are computed at the same time so that kinetic and potential energies can be computed at the same time. In this algorithm the velocities are computed at half time step;

$$\mathbf{v}\left(t+\frac{1}{2}\triangle t\right) = \mathbf{v}(t) + \mathbf{a}(t)\cdot\frac{\triangle t}{2} \tag{2.10}$$

then new positions are computed;

$$\mathbf{r}(t+\triangle t) = \mathbf{r}(t) + \mathbf{v}\left(t+\frac{1}{2}\triangle t\right)\cdot\triangle t \tag{2.11}$$

here forces are computed and then the acceleration as;

$$\mathbf{a}(t+\triangle t) = \frac{\mathbf{F}(t+\triangle t)}{m} \tag{2.12}$$

where m is the mass of particle. And at the end velocities are computed at $\mathbf{v}(t+\triangle t)$

$$\mathbf{v}(t+\triangle t) = \mathbf{v}\left(t+\frac{1}{2}\triangle t\right) + \mathbf{a}(t+\triangle t)\cdot\frac{\triangle t}{2} \tag{2.13}$$

The equation 2.11 and 2.13 are used to compute the $\mathbf{r}(t+\triangle t)$ and $\mathbf{v}(t+\triangle t)$ at the same time.

2.1.3 Thermostat and barostat

Thermostats are widely used in MD simulations because most of the experiments are carried out in the canonical ensemble rather than in the micro canonical ensemble [82]. We bring the system in contact with a heat bath in order to control the instantaneous temperature such that the probability to find a system in a given energy state is described by the Boltzman distribution. The instantaneous kinetic temperature of the system is measured from the kinetic energy per particle and thus fluctuates for any finite canonical system. If the instantaneous kinetic temperature does not fluctuate as in isokinetic molecular dynamic scheme or in velocity scaling algorithms then the ensemble would not be the true canonical ensemble [78].

A large variety of thermostats are available to control the temperature. They are classified into two main categories: local thermostats and global thermostats. Local thermostats dissipate energy on a local level and global thermostats dissipate energy on the system level uniformly. Local thermostats are preferable because they are usually more realistic and allow temperature control on a local level [83]. Apart from local or global nature of the thermostat, one should also consider the properties which he wants to compute when selecting the thermostat. For example if one wants to compute the dynamic properties of the system he should not use the Andersen thermostat because it disturbs the dynamics.

The most common methods to control the temperature include the velocity scaling [84, 85], stochastic [86–89] and extended system methods [90, 91].

Thermostats control the temperature by changing the velocities, and barostats control pressure by changing the dimensions of the simulation box. Berendsen [85], Andersen [86], Parrinello-Rahman barostats [92], Nose Hoover barostat [90, 91] and Langevin dynamics based barostat [93] are the commonly used barostats. We use a Langevin dynamics based thermostat and barostat in all NPT simulations and we use dissipative particle dynamics (DPD) thermostat in all NVT simulations. We provide description of these thermostats in next chapters where they are applied.

2.1.4 Periodic boundary conditions

In molecular dynamics simulations we use periodic boundary conditions to mimic a bulk systems with a system consisting of small number of particles; and to eliminate the surface effects. We show a 2D schematic of the periodic boundary condition in FIG. 2.2. The simulation cell **A** is called the primary simulation cell and all other cells are replicas of this cell. These replicas have images of the particles belonging to the primary cell. Once a particle leaves the primary cell from one face its image enters the primary cell from the opposite face. The system is isotropic and no surfaces are created.

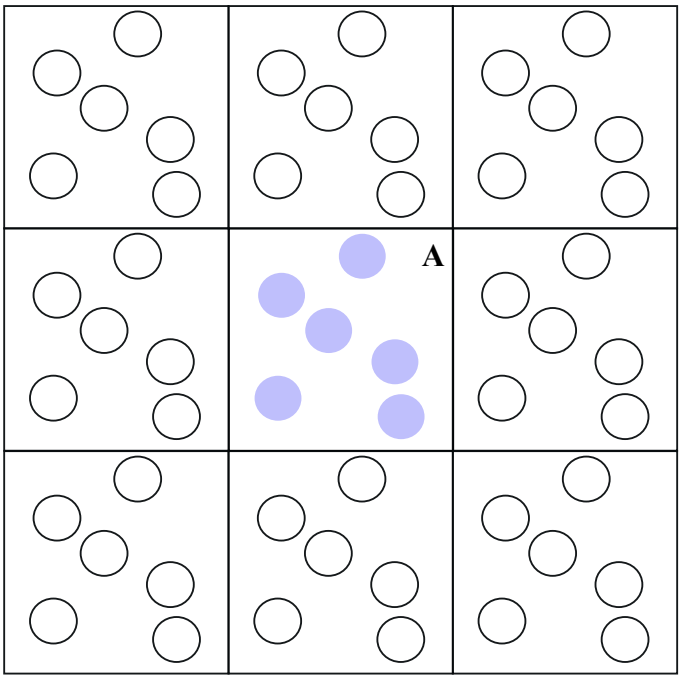

FIGURE 2.2: Two dimensional schematics of periodic boundary conditions.

2.2 Model

Like Yi and Rutledge [38–40], we use a united atom model for polyethylene that has been proposed by Paul et al. [69] and later on modified by Waheed et al. [70]. The chains consist of beads or "united atoms" that represent CH_2 and CH_3 groups. Beads interact with each other via bonded and nonbonded potentials. The non bonded interaction is of the Lennard Jones form and it acts between all pairs of monomers apart from the monomers that are directly connected along the chain. For a distance r_{ij} between monomers i and j it is given by:

$$\begin{aligned} U(r_{ij}) &= 4\epsilon_{ij}\left[\left(\frac{\sigma_{ij}}{r_{ij}}\right)^{12} - \left(\frac{\sigma_{ij}}{r_{ij}}\right)^{6}\right], r_{ij} \leq 2.5\sigma_{ij} \\ U(r_{ij}) &= 0, r_{ij} > 2.5\sigma_{ij} \end{aligned} \tag{2.14}$$

The bonded potential, which acts between monomers along the chain, consists of a harmonic bond:

$$U(r_{ij}) = \frac{1}{2}K(r_{ij} - R)^2 \tag{2.15}$$

and a harmonic bond angle:

$$U(\theta) = \frac{1}{2}K_\theta(\theta - \theta_0)^2 \tag{2.16}$$

where θ is the angle between two consecutive bonds, and a dihedral potential:

$$U(\phi) = \frac{1}{2}[K_{1\phi}(1 - \cos\phi) + K_{2\phi}(1 - \cos 2\phi) + K_{3\phi}(1 - \cos 3\phi)] \tag{2.17}$$

where ϕ is the dihedral angle defined by three consecutive bonds. All parameters for the potentials are given in the Table. 2.1. The model reproduces the dynamical and structural properties of the melt, the melting point, and the rotator phase. It does not predict the orthorhombic crystal phase.

TABLE 2.1: Parameters for the model, all parameters except the value of cutoff radius for Lennard Jones have been taken from [70], and this value have been taken from [38].

Potential	Parameters
Harmonic bond	bond length = 1.53 A° K = 700 kcal/mol $A^{\circ 2}$
Bond Angle	K_{θ} = 120 kcal/mol θ_0 = 109.5 $^{\circ}$
Dihedral	$K_{1\phi}$ = 1.6 kcal/mol $K_{2\phi}$ = -0.867 kcal/mol $K_{3\phi}$ = 3.24 kcal/mol
Lennard Jones	σ = 4.01 A° ϵ $(CH_2 - CH_2)$ = 0.112 kcal/mol ϵ $(CH_3 - CH_3)$ = 0.112 kcal/mol ϵ $(CH_2 - CH_3)$= 0.112 kcal/mol Cut off = 2.5 σ

2.3 Order parameters [1]

In order to distinguish the crystalline from the fluid-like regions of the system, we use several order parameters which we describe in following subsections.

2.3.1 Local density

The local density is measured by means of Voronoi tesselation, i.e. the density at the position of particle i is defined as the inverse of the volume of particle i's voronoi cell. In Voronoi tesselation the whole simulation box is divided into small regions such that every particle has a region. For a particle i this region consists of points which are closer to this particle than any other particle. This region is called the Voronoi cell/volume of the particle i.

2.3.2 Radius of gyration

The radius of gyration is used to measure the extension of the polymer chain. The radius of gyration for a single chain can be computed using following equation:

$$R_g^2 = \frac{1}{N}\sum_{k=1}^{N}(\mathbf{r}_k - \mathbf{r}_{cm})^2 \tag{2.18}$$

R_g is the radius of gyration, N is the number of particles in the chain, $\mathbf{r}_k$ is the position of particle k and $\mathbf{r}_{cm}$ is the center of mass of the chain.

We show this schematically in FIG. 2.3. $\mathbf{r}_{cm}$ is center of mass for the chain and $\mathbf{r}1, \mathbf{r}2, \mathbf{r}3, ...\mathbf{r}_k$ are vectors from the center of mass to the monomers of the chains.

[1] Part of this section is published in The Journal of Chemical Physics, 139, 214904 (2013).

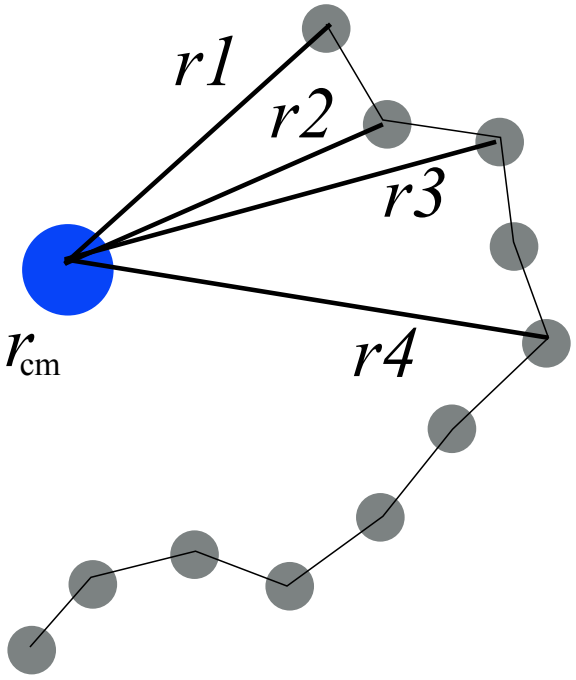

FIGURE 2.3: Schematic of the radius of gyration of the chain. $\mathbf{r}_{cm}$ is the center of mass for the chain and $\mathbf{r}1, \mathbf{r}2, \mathbf{r}3, ...\mathbf{r}_k$ are vectors from center of mass to the monomers of the chain.

2.3.3 Nematic order parameter

We measure the global alignment of chains in terms of the nematic order parameter S_2, which is the largest eigenvalue of

$$Q_{\alpha\beta} = \frac{1}{N_{\text{cn}}} \sum_{j=1}^{N_{\text{cn}}} \left(\frac{3}{2} \hat{u}_{j\alpha} \hat{u}_{j\beta} - \frac{1}{2} \delta_{\alpha\beta} \right) \quad ,$$

where N_{cn} is the number of chains for which the calculation is performed, $\hat{u}_j$ is the unit vector parallel to the end-to-end vector of chain j, δ is the Kronecker delta and $\alpha, \beta = x, y, z$. [94].

This order parameter is close to unity when all chains are parallel to each other and close to zero when all chains are oriented randomly. We show this schematically in FIG. 2.4. In FIG. 2.4(a), the chains are not oriented in any prefered direction while in FIG. 2.4(b), the chains are oriented in one direction, parallel to each other forming a nematic liquid crystal.

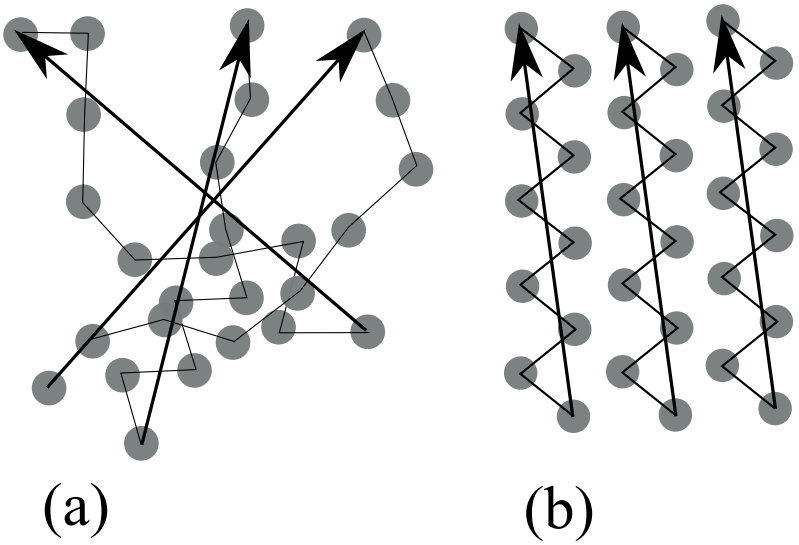

FIGURE 2.4: Schematics representation of nematic order parameter. (a): For a melt configuration. (b): For a nematic liquid crystal configuration.

2.3.4 Crystallinity order parameter

To monitor the local alignment of segments of chains, we identify for a given particle i the neighboring particles j (i.e. the particles that lie within a distance $r_c = 1.4\sigma$ from particle i). For every neighbor j we determine

$$\theta_{ij} = \arccos(\hat{e}_i \cdot \hat{e}_j) \begin{cases} \leq 10 \text{ “aligned”} \\ > 10 \text{ “non-aligned”} \end{cases} \tag{2.19}$$

where $\hat{e}_i$ are unit vectors pointing from the position of particle $i-1$ to the position of particle $i+1$ in a given chain. Particles that have “aligned” neighbors above certain threshold value are called crystalline. We obtain this threshold number from an analysis of the probability distributions of aligned neighbors in the bulk melt and the bulk crystal. It distinguishes melt-like configurations from crystals.

In order to identify crystalline clusters, we use a standard clustering algorithm. This proceeds by picking a particle and checking whether it is crystalline. If so, we count it as the first particle of a cluster and analyze its shell of neighbors, including into the cluster neighboring particles that are also crystalline. In this way, we move recursively from neighbor to neighbor to detect the complete cluster and compute

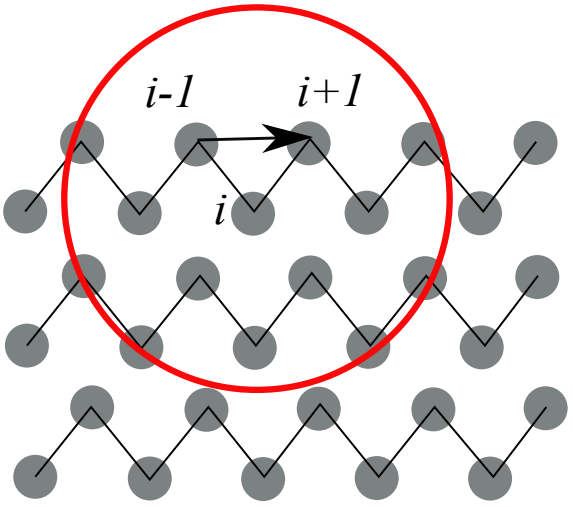

FIGURE 2.5: Schematic of crystallinity order parameter. The red circle shows the cutoff radius for particle i and the black arrow shows the vector from $i-1$ to $i+1$ which is associated with i.

its size. If no new crystalline neighbor is found, the cluster is complete and we proceed with the other particles of the system to detect further clusters.

2.3.5 Bond order parameter

To characterize crystal order in terms of particle positions rather than segment alignment, we use *local bond orientational order* parameters. (The term "bond order", which is commonly used for this type of parameter in the context of monatomic systems, might be misleading in the context of polymers. It refers to the orientation of the vector between any pair of neighbouring particles, not just to bonds along the chain.) Bond orientation parameters characterize the local positional structure by projection of the positions of a particle's neighbors onto spherical harmonics. Rather than the original definition by Steinhardt [95] we use a recent extension [96] which exploits additional information derived from the second shell of neighbors, defining the so called *averaged local bond order parameters* (ALBO). This definition requires the computation of the complex vector $q_l(i)$

$$q_{lm}(i) = \frac{1}{N_b(i)} \sum_{j=1}^{N_b(i)} Y_{lm}(\mathbf{r}_{ij}) \tag{2.20}$$

where $N_b(i)$ corresponds to the number of nearest neighbors of particle i and $Y_{lm}(\mathbf{r}_{ij})$ are the spherical harmonics. Averaging over the neighbors of particle i and particle i itself

$$\bar{q}_{lm}(i) = \frac{1}{\tilde{N}_b(i)} \sum_{k=0}^{\tilde{N}_b(i)} q_{lm}(k), \tag{2.21}$$

and summing over all the harmonics

$$\bar{q}_l(i) = \sqrt{\frac{4\pi}{2l+1} \sum_{m=-l}^{l} |\bar{q}_{lm}(i)|^2} \tag{2.22}$$

one gets the final value of the locally averaged bond order parameter $\bar{q}_l$.

2.3.6 Trans states

Another order parameter which can be used to see the phase transition in polymeric systems is the number of *trans* conformations in the system. Polymers which differ only in the rotation about a bond along the chains are called conformations of the polymers. Two different conformations of the same polymer are shown schematically in FIG. 2.6. A *trans* state is defined as a conformation in which the dihedral angle lies between $-60°$ and $60°$.

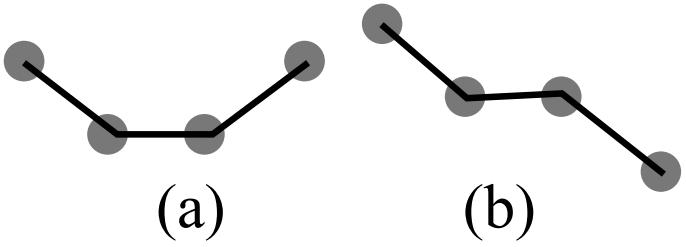

FIGURE 2.6: Schematics of two different conformations of same polymer. Left: First and last particle are on the same side of the middle bond making a dihedral angle of $0°$ about the middle bond. Right: First and last particle are on opposite side of the middle bond making a dihedral angle of $180°$ about the middle bond.

2.4 Critical nucleus size

The critical nucleus size determination is an important aspect of nucleation studies because mechanical properties of the final product depend on the size, the shape and the distribution of nuclei in the system. We use two different methods to compute the critical nucleus size. In the following subsections we describe mean first passage time analysis and committor analysis in detail.

2.4.1 Mean first passage time analysis

In order to estimate the critical nucleus size and the induction time, mean first passage time (MFPT) analyses [97] are performed on the evolution of largest cluster. The mean first passage time (MFPT) analyses are performed to define the average time of first appearance of a cluster with size n_{max}:

$$\tau(n_{max}) = \frac{1}{M}\sum_{i=1}^{M} \tau_{n_{max}}^{(i)} \tag{2.23}$$

where M is total number of trajectories and $\tau_{n_{max}}^{(i)}$ is the time when cluster with size N first appears. As nucleation is followed by fast cluster growth, $\tau(n_{max})$ has a sigmoidal shape and can be fitted by the equation:

$$\tau(n_{max}) = 0.5\tau^*[1 + \mathrm{erf}(Z\sqrt{\pi}(n_{max} - n^*))] \tag{2.24}$$

where n^* is the critical nucleus size, Z is the Zeldovich factor and the error function is $\mathrm{erf} = \frac{2}{\sqrt{\pi}}\int_0^x e^{-x^2}dx$. This method has been used in studies of glass forming systems under shear [98, 99] and n-alkanes of C8, C20 and C150 by Yi et.al [38–40]. We can compute all quantities which are needed to describe the nucleation process using the MFPT method [100]. We can determine induction time τ^*, critical nucleus size n^*, Zeldovich factor, free energy barrier and attachment rates. Once we have the induction time and volume of the system, we can compute the nucleation rate density using:

$$I = \frac{1}{< \tau^* > V} \tag{2.25}$$

Where I is nucleation rate density, τ^* is induction time and V is volume of the system. Lundrigan and Voivod [100] tested the MFPT for the crystal nucleation of the Lennard Jones fluid. They found the nucleation rate in agreement with the nucleation rate predicted by the classical nucleation theory.

2.4.2 Committor analysis

Committor analyses [101] are also performed, to compute the critical nucleus size. It has some advantages that it is based on the kinetics of the transformation process only and does not require an underlying free-energy landscape model, such as e.g. an analysis in terms of classical nucleation theory. In this method, we determine $p_{\text{crystal}}(n_c)$, the probability that a trajectory initiated from a given cluster size n_c ends in a stable crystalline state. The cluster size for which $p_{\text{crystal}}(n_c) = 0.5$ is the typical size of the *critical nucleus*.

The analyses are performed considering several independent configurations with different cluster sizes. By considering each of these independent configurations as initial configurations, we made several simulation runs using different random seeds. We randomized the velocities of these configurations several times, and thus generate several new trajectories per cluster size, which are then run until either a stable crystal or a melt configuration is reached.

2.5 Classical nucleation theory

When a melt is cooled below melting temperature, small nuclei are formed which disappear again or further grow to make stable nuclei. This process is called nucleation. The thermodynamics and the kinetics are two important aspects of study of the nucleation process. Thermodynamics describes the availability of driving force and kinetics tells us how much time is needed for the process to occur.

Classical nucleation theory (CNT) has been extensively used to study phase transitions since the 1930's after its creation by Volmer and Weber [102] and Becker and Döring [103] and further [104, 105]. In homogeneous nucleation, the thermodynamic driving force comes from the supersaturation. The free energy relationship for the homogeneous nucleation process for a spherical nucleus of radius R can be written as:

$$\triangle G = -\frac{4}{3}\pi R^3 \triangle G_v + 4\pi R^2 \sigma \tag{2.26}$$

$\triangle G_v$ - free energy gain
σ - surface free energy

If the energy released during the formation of the nucleus is larger than the energy to create the interface between liquid and solid, the process will continue otherwise the newly formed nucleus will be dissolved. A cost to continue the process is required until a nucleus of critical size is formed, the critical radius can be calculated as:

$$R^* = -\frac{2\sigma}{\triangle G_v}\frac{dG}{dR} = 0 \tag{2.27}$$

Once the cluster size reaches the critical nucleus size, energy is released from the process instead of being consumed and the cluster grows further, limited only by diffusion processes. The free energy to form nucleus of critical size:

$$\triangle G^* = \frac{16\pi\sigma^3}{3(\triangle G_v)^2} \tag{2.28}$$

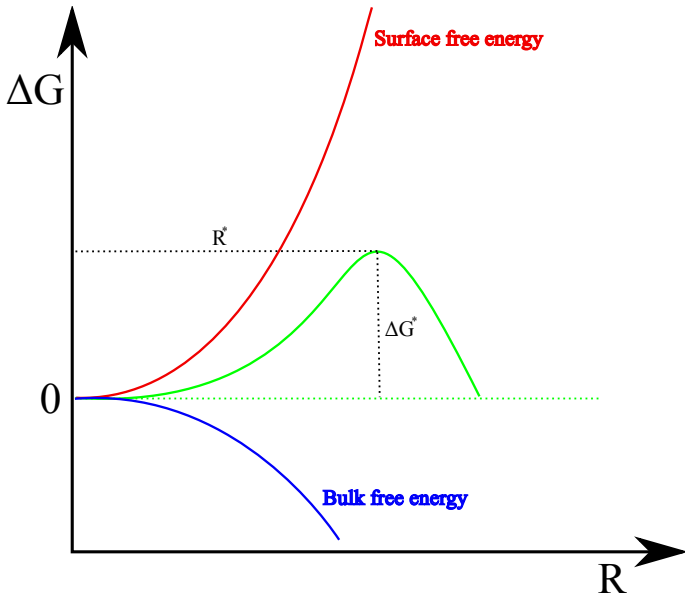

FIGURE 2.7: Representation of the free energy for homogeneous nucleation to form a spherical nucleus. The total free energy is shown with a green curve, surface free energy is shown with a red curve and bulk free energy is shown with blue color curve. $\triangle G^*$ is the free energy barrier to form a critical nucleus of radius R^*.

The thermodynamics of the nucleation process in CNT is based on the capillarity approximation. On one hand it simplifies the thermodynamics of the process to large extent by assuming that macroscopic thermo physical properties can be used to describe the nuclei: it assumes that nuclei have same density and chemical potential as of bulk liquid and have the surface tension of a macroscopic liquid-solid interface. On the other hand it is regarded as the weakest point of the classical nucleation theory, and most of the time blame goes to capillary approximation if CNT fails to produce results which are unsatisfactory to explain the experimental results [106].

In case of polymeric materials the critical nucleus is assumed to be of cylindrical shape due to the anisotropic nature of chain molecules, the free energy of formation of the critical nucleus of cylindrical shape with radius R and stem length l can be computed as;

$$\triangle G = -\frac{4}{3}\pi R^3 \triangle G_v + 2\pi R^2 \sigma_e + 2\pi R l \sigma_s \tag{2.29}$$

where σ_s and σ_e are the lateral surface free energy and the stem end surface free energy respectively. Minimizing the free energy with respect to radius R and length

l, the critical free energy barrier $\triangle G^*$, the radius of critical nucleus R^* and the length of critical nucleus l^* can be calculated as:

$$\triangle G^* = 8\pi\sigma_s^2\sigma_e / \triangle G_v^2 \quad (2.30)$$

$$R^* = 2\sigma_s / \triangle G_v \quad (2.31)$$

$$l^* = 4\sigma_e / \triangle G_v \quad (2.32)$$

The kinetics of the nucleation is described by the nucleation rate density which is related to number of nuclei formed per unit of volume and time. Nucleation rate can be expressed as:

$$I = I_0 \exp^{-\left(\frac{\triangle G^*}{k_B T}\right)} \quad (2.33)$$

Where I is the nucleation rate, I_0 is the kinetic prefactor, k_B is the Boltzmann' constant, T is the temperature of the system, $\triangle G^*$ is the free energy barrier corresponding to the critical nucleus.

2.6 Crystallization in polymers

Crystallization involves primary nucleation and growth. Nucleation is a fluctuation driven process, these fluctuations form small nuclei in the system. If the size of the newly formed nucleus is larger than the critical nucleus then the crystallization process starts by crossing the critical free energy barrier, while in growth there is no free energy barriers. The formation of a nucleus in a system of single particles is sketched in FIG. 2.8(a). In case of polymer chains (FIG. 2.8(b)) connectivity of monomers adds complexity to the system due to restrictions on the motions of the individual monomers. Due to this connectivity chains first have to reorganize themselves internally before making any ordered structure. Due to this reorganization, the free energy barrier associated with the formation of the nucleus is higher than the single particle system and many metastable states exist between isotropic and ordered crystal structures [68, 107].

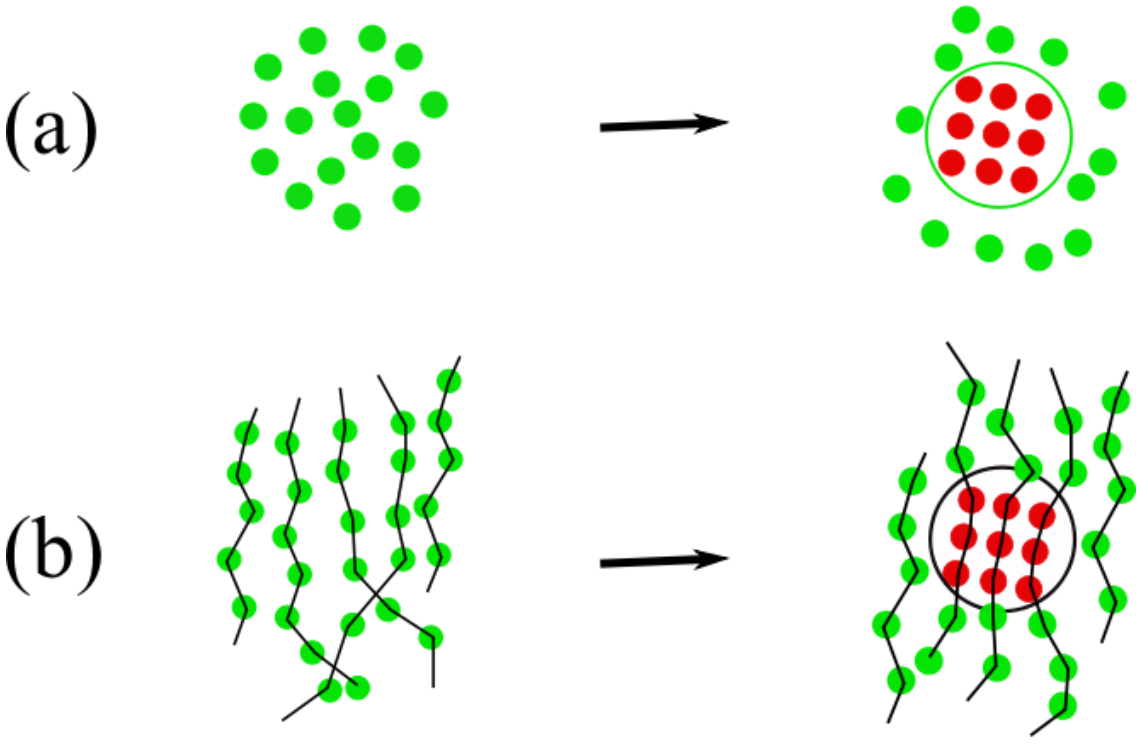

FIGURE 2.8: Sketch of formation of the critical nucleus. (a) A critical nucleus is formed in a single particle system. (b) A critical nucleus is formed in a chain molecule system. Green particles have melt (disordered) structure and red particles have ordered structure.

Once a stable nucleus is formed, the new chains come to the growth front to attach to the crystallite. The process of attaching of first stem of the new chain to the crystallite is called secondary nucleation. The free energy change for a secondary nucleation can be calculated by assuming the crystallite stem as rectangular with lateral size a and stem length l, we can write equations for free energy change, critical free energy barrier, critical size in lateral direction and critical length as [108]:

$$\begin{aligned} \triangle G &= -al \triangle G_v + 2l\sigma_s + 2a\sigma_e && (2.34)\\ \triangle G^* &= -8\sigma_e / \triangle G_v && (2.35)\\ a^* &= 2\sigma_s / \triangle G_v && (2.36)\\ l^* &= 4\sigma_e / \triangle G_v && (2.37) \end{aligned}$$

All notations in these equations are the same which we used in section 2.5. The size of crystallite in the lateral direction is well developed $a \gg l$, and the lateral surface free energy term can be neglected.

$$\triangle G = -\pi R^2 l \triangle G_v + 2\pi R^2 \sigma_e \quad (2.38)$$

We obtain same results for the stem length $l = 2\sigma_e / \triangle G_v$ from both the least stability conditions $\triangle G = 0$ and the least lateral growth conditions $\frac{\partial \triangle G}{\partial R} = 0$.

The attachment of polymer chains at the growth front is an intricate process. It involves polymer diffusion, entanglement effects, competitive absorption/desorption and other factors such as the transition from random coil conformation to extended or folded crystal structure [4]. There are two dominating approaches to study crystal growth in polymer [109]. The first theory of growth of crystals is described by Lauritzen and Hoffman (LH) theory, sometime referred as the surface nucleation approach. The LH model describes a free energy barrier for every molecule to attach at the growth front and the nucleation process associated to the lamellar growths called the secondary nucleation process. In the first step, the first stem of the molecule is placed at the growth front in the growth direction and then other stems of the same molecule are spread in a lateral direction. According to the LH model there are three regimes for secondary nucleation and growth. In the first

regime, the lateral growth rate is higher than the secondary nucleation rate. After the first stem of the molecule attaches, a complete layer is formed in the lateral direction. In this case monolayers are added one by one and the overall growth rate is controlled by the secondary nucleation rate. In the second regime, the lateral growth is comparable to or smaller than the secondary nucleation rate, so more first stems or new layers are formed before the first layer is fully formed. The overall growth rate is controlled by the lateral growth rate and the secondary nucleation. In the third regime, more and more first stems or new layers are attached and the lateral growth become irrelevant [68, 110]. Muthukumar summarized the extensions and criticisms to the Lauritzen and Hoffman theory in Advances of Polymer Sciences [110]. The main conclusions from the LH model include estimation of the minimum thickness of a stable lamellae and the computation of growth rates of polymer crystallization. It also addresses the variation of the lamellae thickness and growth rates at different degrees of supercooling. It does not address questions such as the formation of the lamellae from primary nucleation, quantitative estimation of the degree of crystallinity, bulk crystallization kinetics and many other important aspects of polymer crystallization.

The second theory was presented by Sadler and Gilmer (SG) [29]. In the SG model surface roughness and molecular pinning are considered, which create an entropic barrier. In this method units consisting of straight chain segments containing only few monomers are imagined to lay down on the growth surface parallel to pre-existing chains. These units can be attached anywhere on the growth surface even with a length shorter than the equilibrium stem length and without completing the layers. No more than one stem, either complete or partial, can attach at same position. This pinning of short stems must be removed to continue the growth process or in other words the entropic barrier due to the disorder of these short stems must be overcome for the crystallization to proceed.

Recently, Strobl [10] proposed a new route to crystallization from entangled polymer melt. According to him, blocks of mesomorphic layers of liquid are formed which are composed of chains not perfectly stretched. The density of these layers is slightly higher than the liquid. There is a minimum thickness of layer to be stable in the liquid and thickening process of these blocks of layers continues until critical thickness of layer is reached. When a block of layers of critical thickness is formed,

a higher ordered structure called a granular crystal layer is formed. This transition has relatively low free energy barriers. The last step is merging of these blocks to form homogeneous lamellar crystallites.

Chapter 3

Crystallization of n-Eicosane under Quiescent Conditions

In this chapter we study crystallization in a model system of n-eicosane (C20) by means of molecular dynamics simulation. The melting and crystallization temperatures are estimated by heating the crystal structure and cooling the melt respectively. The values of the parameters used in the crystallinity order parameter are optimized. Committor analyses are performed to find out the critical nucleus size. The nucleation rates dependence on the system size and on the temperature are shown. Then, the effective free energies related to alignment and straightening of chains have been estimated. Finally, at the end of this chapter, the microscopic mechanisms of homogeneous crystal nucleation and growth are identified.

3.1 Introduction

There is a long-standing research interest in the crystallization of polymer melts, and still there are many questions related to crystal nucleation and growth which are not answered completely [14]. Crystallization of polymers is a complex process due to the involvement of reorganization of individual chains from random coil (high entropy) states to extended or folded (low entropy) states. For long chains it becomes even more difficult due to entanglement effects. To avoid the complexity which arise from folding and entanglement, a study of how short chain alkanes crystallize should be of fundamental importance because the short chain alkanes are short versions of polymers like polyethylene. *n*-Alkanes are a basic feed stock for all chemical industries. They are also one of the basic building blocks for biological lipids and for polyethylene [111].

Experimentally nucleation is typically studied using rheometry, dilatometry and differential scanning calorimetry (DSC) measurements. Nucleation studies of n-alkanes using experimental methods has been previously reported in the literature [112–114]. These experiments are usually restricted to a spatial and temporal resolution that is too coarse to capture atomistic details of individual nucleation events. Thus molecular dynamics provides an ideal instrument to complement experiment and offer insight into the mechanisms on the atomistic scale.

Crystal nucleation in alkanes has also been addressed in several computer simulation studies in the 90s [34–37] and a scenario for the nucleation mechanism has been suggested. Due to the limited computer resources available at the time, however, these works were based on one simulation trajectory each (with the exception of ref.[34]). The first direct computations of homogeneous nucleation rates in n-alkanes by means of computer simulation were presented by Rutledge and co-workers in the past few years [38, 39]. These studies were focused on the nucleation and growth rates and the free energy landscape associated with the crystallization process rather than the microscopic mechanisms. Very recently, also simulation results on nucleation rates [40], nucleation rate and mechanism [41] and growth mechanisms [43] in systems of chains longer than the entanglement length have also been presented.

In this chapter, we present a detailed analysis of the formation of crystal nuclei from the homogeneous melt and the subsequent growth process in n-eicosane(C20). The main results of this chapter are published in The Journal of Chemical Physics [42].

3.2 Model & order parameters

We use a united atom model, this model along with all parameters was described in Chapter 2.

In order to differentiate the crystallite particles from the the melt particles and then to propose the nucleation mechanism we have described several order parameters in Chapter 2. These order parameters include the local density V^{-1} corresponding to every particle, the radius of gyration R_g of the chains, the nematic order parameter S_2 of the chains, the crystallinity order parameter and the local bond order parameter q_6q_6. For the crystallinity order parameter, the threshold values for the cut off radius r_c and the minimum number of aligned neighbors for a particle to be crystalline are computed and shown in section 3.5.1. Two neighbours i and j are considered as "aligned" if the chains they belonged to locally are almost parallel ($\theta_{ij} \leq 10$).

3.3 Thermostat and barostat

We performed molecular dynamics simulations at constant pressure, constant temperature and with fixed number of particles (NPT ensemble). The velocities of the particles were rescaled to keep the temperature constant and the dimensions of the system fluctuated by rescaling the positions of the particles. We used a Langevin dynamics based equation of motion to control the temperature and pressure of the system [93, 115]. Langevin thermostat consists of a dissipative force term and a random force term. The Langevin dynamics can be understood by considering Brownian motion in which dissipation is caused by the friction with solvent particles and random force is caused by the kicks of the solvent particles. The fluctuation dissipation theorem is used to relate dissipative and random terms through the temperature of the system. As the Langevin thermostat control the temperature by adding or subtracting the heat via the dissipative forces and the random forces on a local level, it can deal with energy source and sinks in the system. It can also be used for systems under shear flow [116].

First of all we provide the formulae to compute instantaneous pressure and difference in pressure, then we explain the implementation of this algorithm [93, 115] in the ESPRresSo package [71] step by step.

The instantaneous pressure P_{ins} of the system can be computed as:

$$P_{ins} = \rho k_B T + \frac{1}{3V} \sum_{i<j} \left\langle \mathbf{r}_{ij} \mathbf{f}_{ij}^{sr} \right\rangle \tag{3.1}$$

Where ρ is the number density of the system, V is the volume of the system, $\mathbf{r}_{ij}$ is the distance between particle i and j and $\mathbf{f}_{ij}^{sr}$ are all forces between particle i and j. The difference in the desired pressure P and the instantaneous pressure can be written as;

$$\Pi = P_{ins} - P \tag{3.2}$$

Step 1: The momentum $\mathbf{p}_i = m_i \mathbf{v}_i$ and the position $\mathbf{r}_i$ of the particles can be updated using the scheme;

$$\mathbf{p} = \mathbf{p}_i(t) + \mathbf{f}_i(t) \frac{\triangle t}{2} \tag{3.3}$$

Where $\mathbf{f}_i(t)$ is the force on particle i at time t and $\triangle t$ is the simulation time step. For the Langevin type of equations of motion, the dissipative and random force terms can be added in the force and pressure as follows:

$$\mathbf{f}_i \frac{\triangle t}{2} = \underbrace{\mathbf{f}_i \frac{\triangle t}{2}}_{\text{conservative term}} - \underbrace{\gamma_0 \frac{\mathbf{p}_i}{m_i} \frac{\triangle t}{2}}_{\text{dissipative term}} + \underbrace{\sqrt{k_B T \gamma_0 \triangle t} \mathbf{z}_i}_{\text{random term}} \tag{3.4}$$

Where k_B is the Boltzmann's constant, γ_0 is the friction coefficient of the system and $\mathbf{z}_i$ is drawn from a set of uncorrelated random numbers with zero mean and unit variance.

$$(P_{ins} - P)\frac{\triangle t}{2} = (P_{ins} - P)\frac{\triangle t}{2} - \gamma_V \frac{\Pi_V}{Q}\frac{\triangle t}{2} + \sqrt{k_B T \gamma_V \triangle t}\mathbf{z}_V \tag{3.5}$$

Where γ_V is the friction coefficient of the piston and the $\mathbf{z}_V$ is again uncorrelated random numbers with zero mean and unit variance.

Step 2: Compute the instantaneous pressure using Equation 3.1,

$$P_{ins} = P_{ins}((\mathbf{r}_i, V, \mathbf{f}_i)(t), \mathbf{p}_i) \tag{3.6}$$

the momentum of the piston Π_V,

$$\Pi_V(t + \frac{\triangle t}{2}) = \Pi_V(t) + (P_{ins}((\mathbf{r}_i, V, \mathbf{f}_i)(t), \mathbf{p}_i) - P)\frac{\triangle t}{2} \tag{3.7}$$

Step 3: Rescale the volume V of the simulation box at half time step,

$$V(t + \frac{\triangle t}{2}) = V(t) + Q^{-1}\Pi_V(t + \frac{\triangle t}{2})\frac{\triangle t}{2} \tag{3.8}$$

Where Q is the mass of the piston.

Step 4: Rescale the positions of the particles,

$$\mathbf{r}_i = \mathbf{r}_i(t) + \frac{L^2(t)}{L^2(t + \frac{\triangle t}{2})}\frac{\mathbf{p}_i}{m_i} \triangle t \tag{3.9}$$

Where L is the length of the simulation box.

Step 5: Rescale the volume V of the simulation box after complete time step,

$$V(t+\triangle t) = V(t+\frac{\triangle t}{2}) + Q^{-1}\Pi_V(t+\frac{\triangle t}{2})\frac{\triangle t}{2} \tag{3.10}$$

Rescale the positions of the particles after a complete time step,

$$\mathbf{r}_i(t+\triangle t) = \frac{L(t+\triangle t)}{L(t)}\mathbf{r}_i \tag{3.11}$$

Rescale the momenta of the particles after a complete time step,

$$\mathbf{p}_i^* = \frac{L(t)}{L(t+\triangle t)}\mathbf{p}_i \tag{3.12}$$

Step 6: Compute the new forces at $\mathbf{f}_i(t+\triangle t)$ using updated positions $\mathbf{r}_i(t+\triangle t)$ and then the compute the instantaneous pressure P_{ins},

$$P_{ins} = P_{ins}((\mathbf{r}_i, V, \mathbf{f}_i)(t+\triangle t), \mathbf{p}_i^*) \tag{3.13}$$

the momentum of the piston Π_V,

$$\Pi_V(t+\triangle t) = \Pi_V(t+\frac{\triangle t}{2}) + (P_{ins}((\mathbf{r}_i, V, \mathbf{f}_i)(t+\triangle t), \mathbf{p}_i^*) - P)\frac{\triangle t}{2} \tag{3.14}$$

Step 7: And then the momenta of the particles,

$$\mathbf{p}_i(t+\triangle t) = \mathbf{p}_i^* + f_i(t+\triangle t)\frac{\triangle t}{2} \tag{3.15}$$

In step 1 and step 2 momenta and pressure are computed, rescaling of positions and velocities is carried out from step 3 to step 5 and pressure and momenta are computed again in step 6 and step 7 to use them in next time step. We can compute position and momentum of every particle after a complete time step using Equation 3.11 and Equation 3.15. The efficiency of this algorithm has been tested on a pure Lennard-Johns fluid at constant volume and at constant pressure [115], in this latter case the computation time was increased only by 20% to 30%.

3.4 Simulation details

We simulated three different system sizes of n-eicosane (C20), and then the largest system size at three different temperatures. The system sizes were of 150, 336, 500 chains. In all these cases, we equilibrated the system at 400 K which is well above the melting temperature of eicosane (C20). The equilibrium melting temperature of n-eicosane with this model has been reported as(310±2)K by Yi et al. [39]. We quenched the three systems with 150, 336 and 500 chains from 400 K to 250 K to observe the nucleation event. We also quenched the system with 500 chains from 400 K to 240 K and 230 K. We performed all simulations under constant pressure and constant temperature conditions. In all simulations the pressure was fixed at 1 atmospheric pressure.

We used all distances in units of bead size σ, energy in k_BT and mass in units of mass of bead m. The integration timestep used in simulations was 0.005τ (with the exception of cooling and heating curves where it changes with change in temperature to keep the cooling/heating rate constant), where $\tau = \sqrt{\frac{m\sigma^2}{k_BT}}$. k_B is Boltzmann's constant and T is the temperature in Kelvin.

We used a Langevin dynamics based thermostat and barostat [93]. The friction coefficient γ used for the thermostat was $0.5\tau^{-1}$ and the piston mass for the barostat was $0.00001m$; where τ is the MD simulation time step and m is the mass of every bead. We used the ESPResSo package [71] with customized implementation of the dihedral potential based on Paul wt al. [69].

3.5 Results & discussion

3.5.1 Nucleation rates

Melting temperature

As a first step we determined the melting temperature of the n-eicosane (C20). A system consisting of 150 chains with hexagonal packing was chosen and run until melting with a heating rate of 0.0015K/ps. One of the trajectories is shown in FIG. 3.1 with a red line. With this protocol we find an average melting temperature of (340.8±0.42)K, which is comparable to data available in the literature for this model [53]. We also run simulations for crystallization at a cooling rate equal to the heating rate. Again one trajectory is shown in FIG. 3.1 with a black line. During cooling we ran the simulations at temperatures 400, 370, 330, 310, 300, 285, 270, 250 and 240 K for 66.08 ns each so that the system could relax at that temperature.

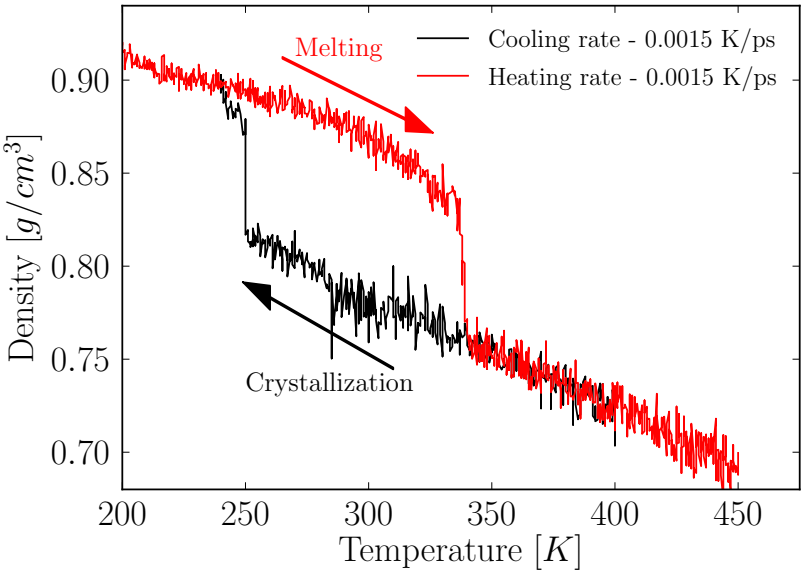

FIGURE 3.1: Cooling and heating curves for n-eicosane(C20) in terms of density temperature diagram.

Optimization of order parameter

To observe the nucleation event we first optimize parameters which we have to use in the calculations of cluster size. FIG. 3.2 shows the radial distribution function of the system at 250K. The first peak is at the distance of bond length, second peak is at the distance of every second consecutive bead along the chains and the third peak is at the nearest neighbor distance for beads belonging to different chains. We chose a cutoff of 1.4σ for counting the number of neighbors of every monomer unit in the calculations of crystallinity order parameter and averaged local bond order parameter. This chosen value is slightly larger than the third peak in FIG. 3.2.

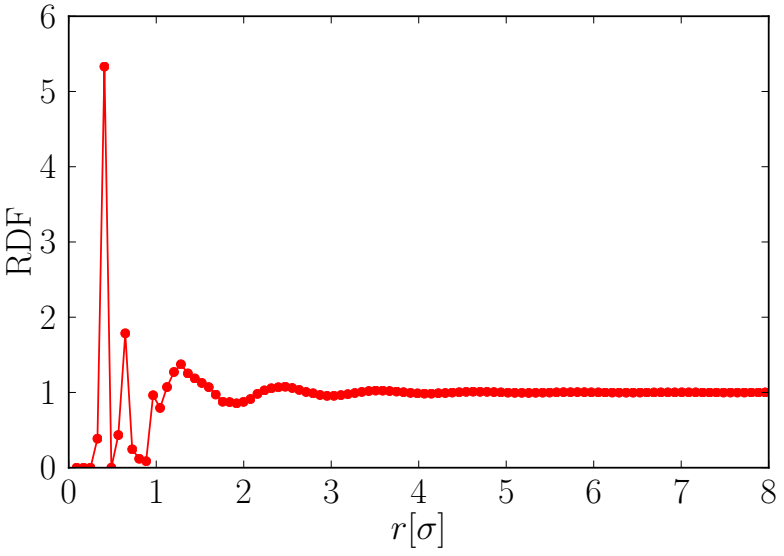

FIGURE 3.2: Radial distribution function.

To distinguish the crystal structure from the melt structure we compute the number of solid bonds for every monomer unit. We have chosen a partially crystallized system and computed the number of solid bonds for every bead. The probability density of number of solid bonds has been drawn in FIG. 3.3. The number of solid bonds to give crystallinity order parameter was selected as 13. The probability of finding solid bonds at these values is at their minimum, hence it is a dividing point between solid and liquid.

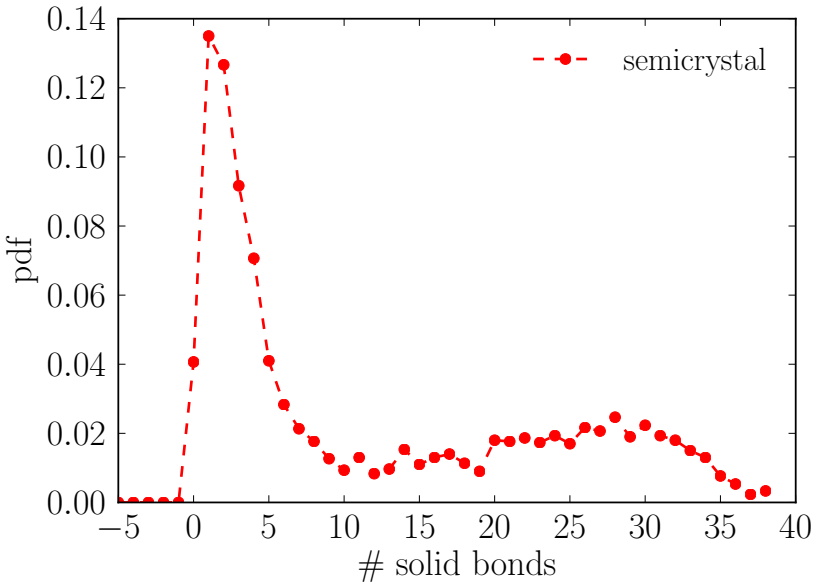

FIGURE 3.3: Probability densities of number of solid bonds for local orientational order parameter at cut off radius of 1.4σ.

FIG. 3.4 shows the number of beads in the largest cluster verses time for a system consisting of 500 chains. These crystallizing trajectories show long induction time and then nucleation event. This nucleation event is random in time and can be described by Poisson distribution. The largest cluster size has been computed using crystallinity order parameter.

Committor Analysis

To identify crystal nucleation events, we perform a *committor analysis* [101]: we determine $p_{\text{crystal}}(n_c)$, the probability that a trajectory initiated from a given cluster size n_c ends in a stable crystalline state. The cluster size for which $p_{\text{crystal}}(n_c) = 0.5$ is the typical size of the *critical nucleus*. This is shown in FIG. 3.5. In this figure, results from the systems with 150, 336 and 500 chains with black, red and green lines with circle symbols have been shown.

The analysis was performed considering 7 different cluster sizes ranging from 30 to 200 monomer units. For each of these, three independent configurations were extracted out of the 25 independent runs. We randomized the velocities of these configurations eight times, and thus generated 24 new trajectories per cluster size,

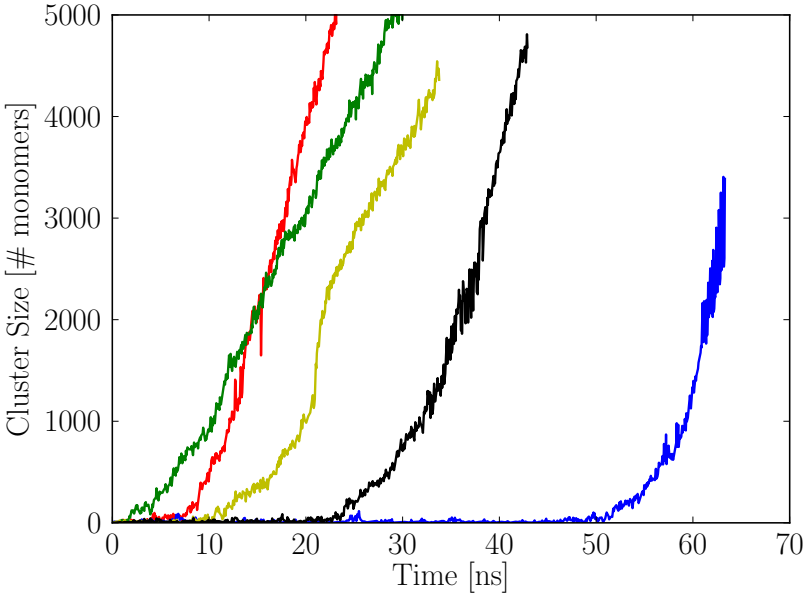

FIGURE 3.4: Number of beads in the largest cluster versus time. These curves have been shown from five different trajectories.

which were run until either a stable crystal or a melt (cluster size < 30) configuration was reached. This type of analysis has the advantage that it is based on the kinetics of the transformation process only and does not require an underlying free-energy landscape model, such as e.g. an analysis in terms of classical nucleation theory. We find that the critical nucleus has a size of 80 ± 20 particles (i.e. polymer repeat units). The uncertainty is mainly due to our choice of crystallinity parameter as the main reaction coordinate to interpret the committor analysis. This shows that additional parameters are needed to properly capture the dynamics of the crystallization process.

To compute the nucleation time and hence the nucleation rate, we use the following equation:

$$I = \frac{1}{\langle t_{ind} \rangle V} \tag{3.16}$$

Where I is the nucleation rate, V is the volume of system and t_{ind} is the induction time. The nucleation rates for three different system sizes were computed and are shown in FIG. 3.6. The system sizes are 150, 336 and 500 chains. The nucleation

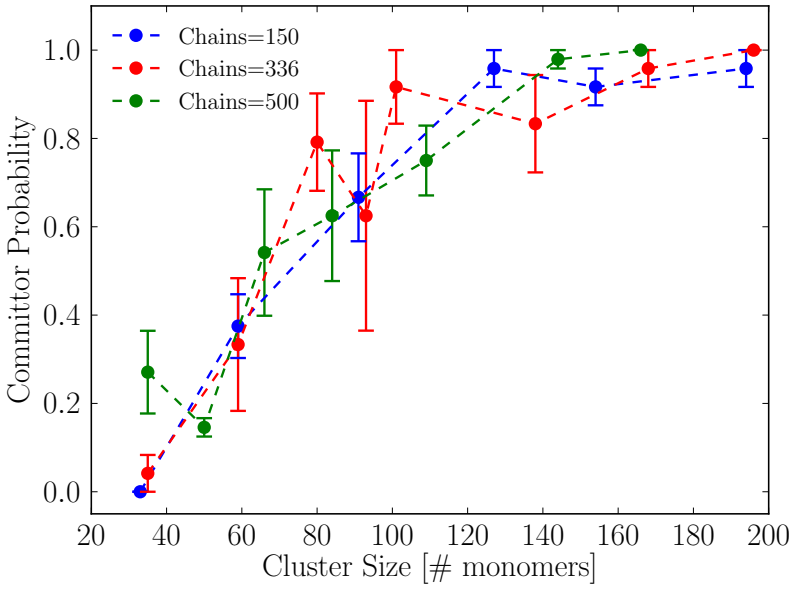

FIGURE 3.5: Committor probability versus the largest cluster size. Results from the systems with 150, 336 and 500 chains are shown in black, red and green color lines with circle symbols.

rates slightly increased with increase in system size and they are within standard error bar for two smaller systems.

FIG. 3.7 shows nucleation rate versus temperature for a system consisting of 500 chains. Nucleation rate increases with the increase in degree of supercooling because the free energy barrier decreases with the increase in degree of supercooling. We have also run simulations at 220 K but nucleation is no longer an induced event at this temperature.

Fig. 3.8 shows a system snapshot labelled according to the locally averaged bond order parameter $\bar{q}_6$. The crystallite embedded in the melt is clearly visible. It is interesting to note that the same particles have been detected as crystallite particles using crystallinity and locally averaged bond order parameter $\bar{q}_6$.

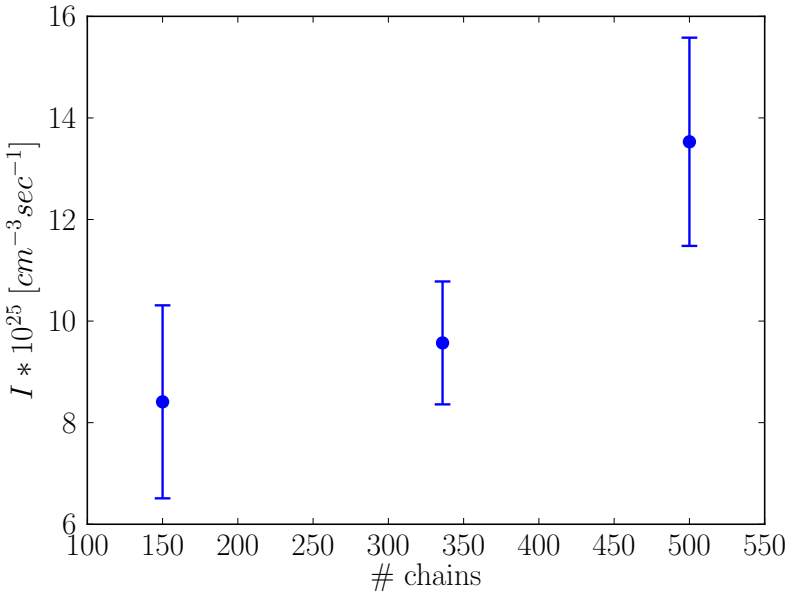

FIGURE 3.6: Nucleation rates for three different system sizes.

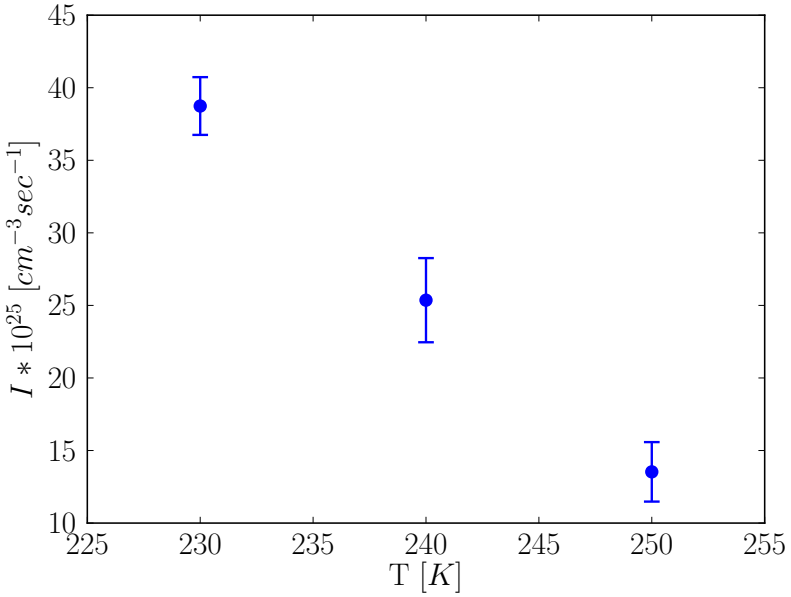

FIGURE 3.7: Nucleation rate as a function of temperature for 500 chains.

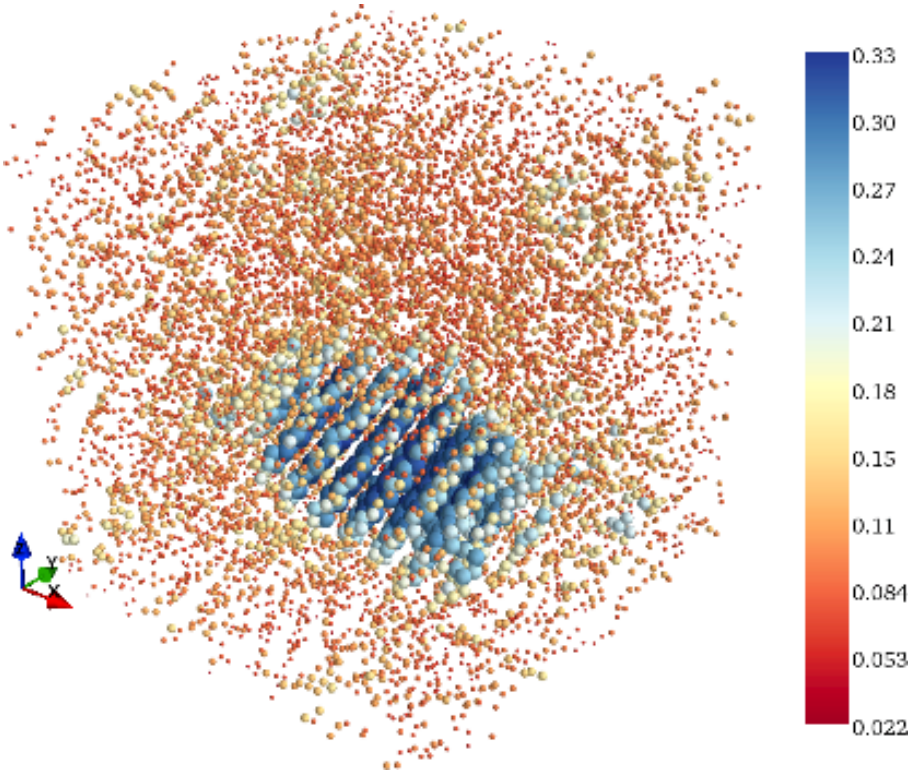

FIGURE 3.8: Use of averaged local bond order parameters in order to determine the crystalline structures. The particles in this simulation snapshot are color-coded according to $\bar{q}_6$. This graph was drawn by Francesco Turci.

3.5.2 Nucleation mechanism

To form a nucleus, a critical number of segments of neighboring chains need to align. In order to see if either the straightening of individual chains or the alignment of different chains give a higher free energy cost to form the critical nucleus we compute the probability of occurrence of such configurations in metastable melt. The circles (red) in Fig. 3.9 show the free energy change in the metastable melt associated with the occurrence of a cluster of aligned neighboring segments that belong to n different chains. Here, a segment is defined for a monomer unit i as the vector connecting the center of monomer $i-1$ to the center of monomer $i+1$. The squares (blue) in Fig. 3.9 show the free energy change associated with straightening of individual chains, i.e. with finding n aligned segments within the same chain. The relatively low free energy changes reflect the long persistence length of polyethylene which has been predicted to be of 8 monomers for this model [38, 117]. Locally aligned clusters

containing segments of more than 9 chains are extremely unlikely to appear by spontaneous fluctuation. In contrast, the melt displays a non-negligible probability to find piece-wise straightened chains, where up to 14-15 out of 20 segments can point in the same direction. Forming a locally ordered (aligned) environment is therefore much more expensive in terms of free energy than straightening individual chains. Similar observations have been made by Takeuchi [35] and by Miura and co-workers [118], who concluded that the nucleation process was initiated by chain straightening and then completed by chain orientation and crystallization. We will show in the following, that this conclusion is not completely correct.

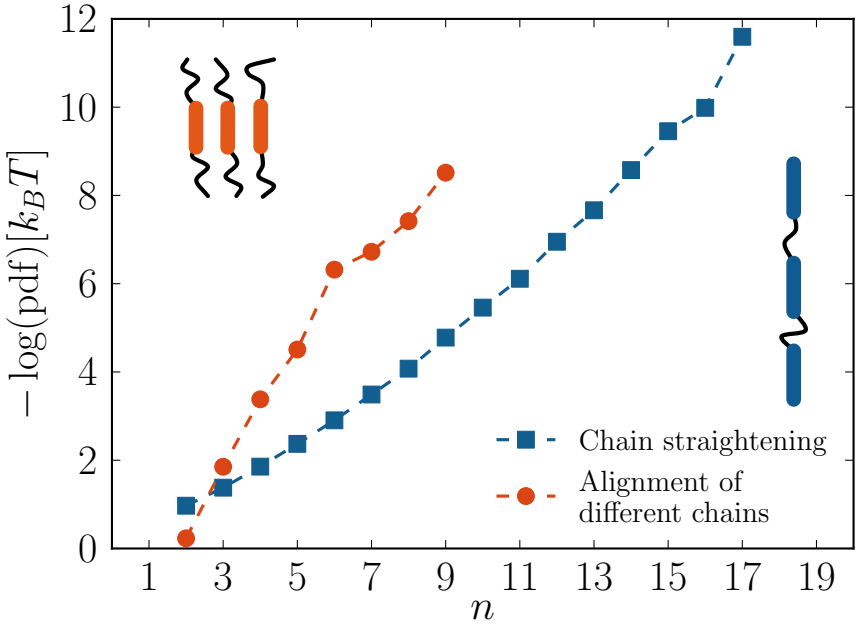

FIGURE 3.9: Effective free energies associated with straightening of individual chains (blue squares) and alignment of neighboring chains (red circles) as a function of the size of clusters of aligned segments n. The colored segments in the sketches represent the selection criteria used for the computation of the corresponding probabilities.

In order to further determine which conditions in the melt structure favor crystallization, we identify the particles that form a critical nucleus and analyze their previous pathway in time. We name t_0 the time at which a crystalline cluster of 80 particles is formed. We then proceed backwards in time in steps of $\Delta t = \tau_D/20$, where $\tau_D = 4 \cdot 10^5 dt$ is the center of mass diffusion time in the supercooled melt and dt is the simulation time step. At $-50\Delta t$ all the particles that belonged to

the nucleus at t_0 are indistinguishable from the ones of the melt according to their structural and orientational properties.

We analyze 25 independent trajectories in terms of the average radius of gyration R_g of all chains that are part of the nucleus at t_0, the global alignment S_2 of these chains, the average volume V of the Voronoi [119] cell associated to each particle that is part of the nucleus, its crystallinity order parameter and the average local bond order parameter $\bar{q}_6$.

In Fig. 3.10 we show the relative variations of these quantities with respect to the values they had at $-50\Delta t$. Approaching the formation of the critical nucleus at t_0, we observe first an increase in the global orientational order S_2, then an increase in the radius of gyration and in the local density, and finally local positional and orientational order are established. We conclude that already in the melt the chains are sufficiently prolate to undergo an ordering transition similar to the isotropic-nematic transition in liquid crystals. Only once they have formed an oriented aggregate, they start straightening. This observation stands in contrast to what has been suggested in earlier work [35, 118], but is similar to recent results of Luo and Sommer [48].

In order to see the positional order we compute the local average bond order parameter $\bar{q}_6$ for every particle that is part of nucleus at time t_0. In Fig. 3.11 we show the evolution of the entire distribution rather than just the average, because the average is still dominated by the peak at liquid-like $\bar{q}_6$ at times when there is already a clearly discernible shoulder of crystalline $\bar{q}_6$.

3.5.3 Growth mechanism [1]

Once a stable nucleus is formed, crystal growth proceeds via the successive attachment of new chains and a lamellar structure develops. We studied the growth mechanism at 250K which corresponds to 19% supercooling, the growth rate under these conditions is computed to be 25 particles $/\tau_D$.

We also present attachment mechanism for n-eicosane, to do so we consider only those parts of trajectories in which cluster size grows from 300 particles to 900

[1]For growth mechanism, except the identification of crystalline clusters in the system, the trajectories were analyzed by Francesco Turci.

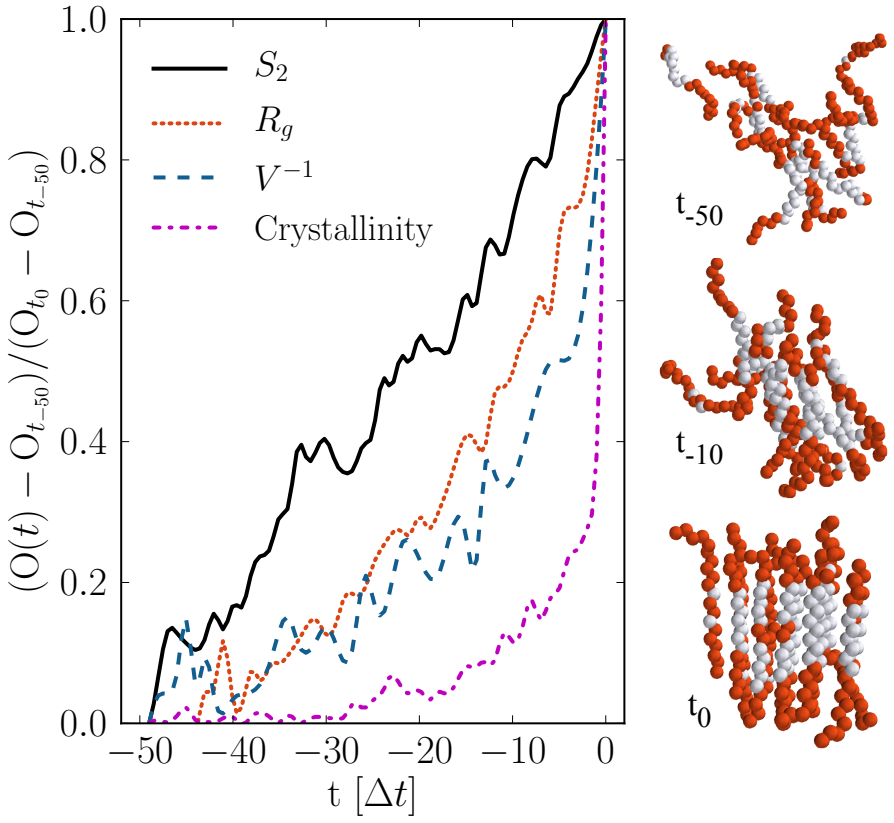

FIGURE 3.10: Relative variation of several observables (O) from the melt to the formation of a critical nucleus for the particles involved in the nucleus: the nematic order parameter S_2 (black, continuous), the radius of gyration R_g (red, dotted), the inverse of the Voronoi cell volume V (blue, dashed) and the crystallinity order parameter (purple, dash-dotted) corresponding to the largest cluster size. The curves are averaged over 25 independent trajectories progressing backward in time from the nucleation time $t = t_0$ in steps Δt to $t = -50\Delta t$. On the right side, we present three snapshots of the nucleus chains. The particles that form the nucleus at time t_0 are highlighted in grey. The chains are already prolate and undergo orientational ordering before they straighten further. Finally a cluster of aligned, hexagonally placed chains is formed.

particles. We choose this upper limit to avoid the finite size effects and the merging of different clusters into single cluster. Along every piece of trajectory, we take configuration snapshots at time intervals Δt. In each snapshot, we identify the crystallite and the "surface chains", i.e. chains that are not part of the cluster but contain at least one particle with a distance of less than 1.4σ from the cluster. Fig. 3.12(a) shows a typical system snapshot, in which all crystalline particles are labelled in blue and surface chains are labelled in red.

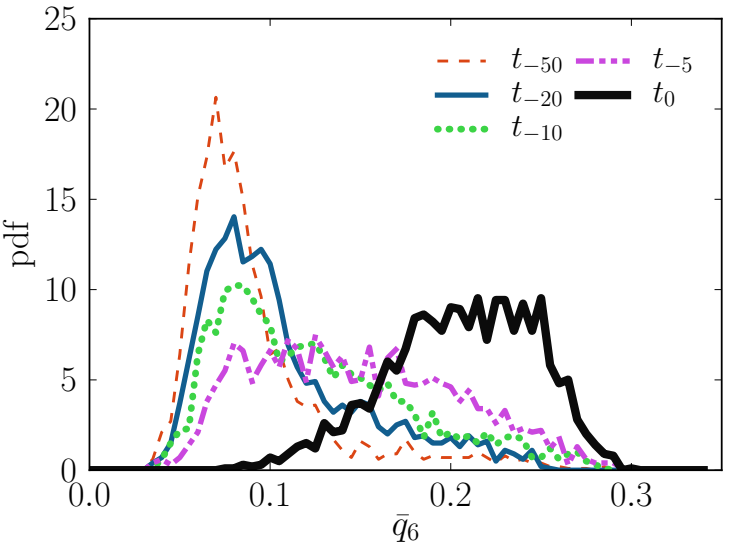

FIGURE 3.11: Probability distributions of the averaged local bond order parameter $\bar{q}_6$ computed at different times for those particles that form the crystallite at t_0.

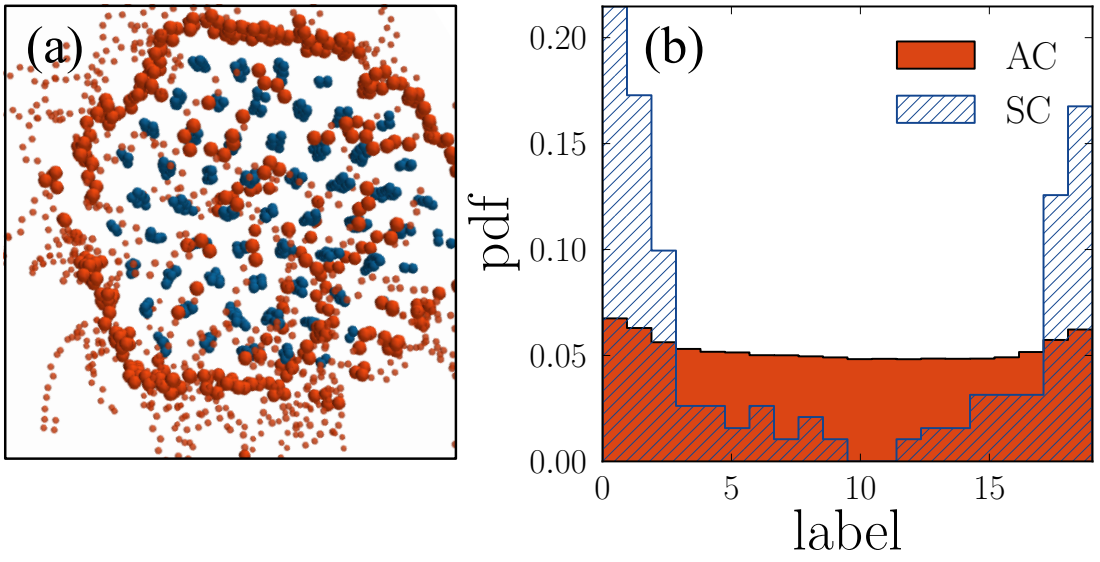

FIGURE 3.12: (a) Top view of a cluster. Crystalline particles (blue) and surface chains (red). Note the hexagonal arrangement of the chains and the relatively low coverage of the top surface by surface chains. (b) Normalized histograms of the surface particles versus label of a particle in the chain (0 to 19): all surface particles (filled histogram) and only those that belong to chains successfully attached after τ_D (dashed histogram). This graph was drawn by Francesco Turci.

After pointing out these surface chains, now we want to identify those surface chains which are attached to the cluster and remain part of the cluster (do not detach) and the properties of these attaching chains which distinguish them from those chains which do not attach to the cluster. We define an "attaching chain" as a surface chain of which at least seven repeat units will be part of the cluster within the next τ_D. The choice of this threshold value is based on our empirical observation that once a chain is attached to the cluster with more than seven particles it does not detach again.

To identify those properties of chains which distinguish attaching chains from non-attaching chains, we computed the radius of gyration R_g, end to end vector R_{ee} and $\bar{q}_6$ and did not see any difference in these properties for the two families of chains. As a further examination, we extracted the information of particle labels (indicating the position of a particle along the chain) and the distances between clusters and the particle labels. In Fig. 3.12(b) we show the distribution of particle labels of those particles that are closer than 1.4σ to the cluster when the surface chain is identified. The dashed histogram shows all surface chains and the filled histogram shows the attaching chains only. It stands out that surface chains which have an end close to the cluster are far more likely to be attached than surface chains which have their middle close to the cluster. This suggests that the initial stages of the attachment process are driven by the motion of the most mobile chain segments and that the crystallization of new chains is initiated at the ends. This mechanism is specific to short chains and it stands in contrast to folded chain crystallization for longer chains [43, 48].

With this picture in mind, we investigate how the remaining parts of a chain are attached to the cluster. Every Δt we plot $\bar{q}_6$ for each particle in an attaching chain. This gives us a "particle label versus time map" for each attaching chain (see Fig. 3.14). Based on visual inspection, we grouped these maps into classes and then compared representative maps for each class with movies of the corresponding molecular dynamics trajectories. We identify *sliding-in* motion as a dominant attachment mechanism. The end particle of the chain is attached on the lateral surface of the cluster. In Fig. 3.13(a-d), we show a trajectory of a single attaching chain. The increase of local order is accompanied by an increase of the radius of gyration, so that the chains are piece-wise straightened, often assuming L-shaped

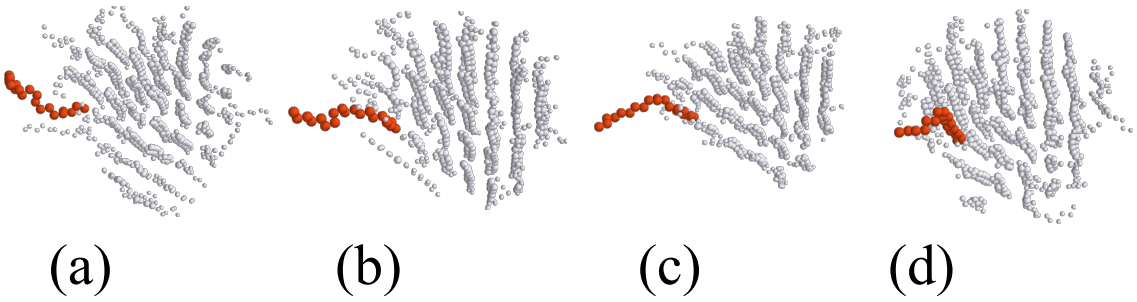

FIGURE 3.13: Trajectory of a chain attaching via the sliding process: (a-d) Snapshots of the time evolution, with big red beads representing the attaching chain, medium sized gray beads being the cluster of crystalline particles and small gray beads being particles that belong to the cluster chains but are not crystalline. Every iteration corresponds to a single $\Delta t = \tau_D/20$. This graph was drawn by Francesco Turci.

conformations. The end monomer that is attached first moves along the direction given by the nearest cluster chains, and guides the attachment of the rest of chain.

As we have shown that the *sliding-in* motion is a dominant attachment mechanism, we want to investigate if these attaching chains attach in some correlated manner or randomly. We find that the attachment process is not simply characterized by the stochastic motion of single chains in the melt that randomly attach to the cluster in an uncorrelated manner. It is a correlated process, as demonstrated in Fig. 3.15. Between all chains that were attached in a given frame, we computed the pairwise distances (where the distance between two chains was defined as the distance between the closest pair of particles of the chains). If the distance was less than 1.4σ we considered two chains as "neighbors". Fig. 3.15 shows the frequency with which clusters of neighbouring chains have been attached.

To compare this distribution with that of an uncorrelated process, we sampled the attachment statistics of non-interacting cylinders on the surface of the clusters. For each cluster configuration, we picked random sites uniformly distributed on the surface of the crystal and placed cylinders at these sites (see Fig. 3.15 (d)). The cylinders were oriented parallel to the average orientation of the chains in the crystallite. Their "contact site" with the cluster was picked uniformly distributed along their length. For each crystallite, we picked as many cylinders as attaching chains had been observed, and produced 1000 different realizations of attachment events. Then we averaged the results over all crystallites. Fig. 3.15 shows that

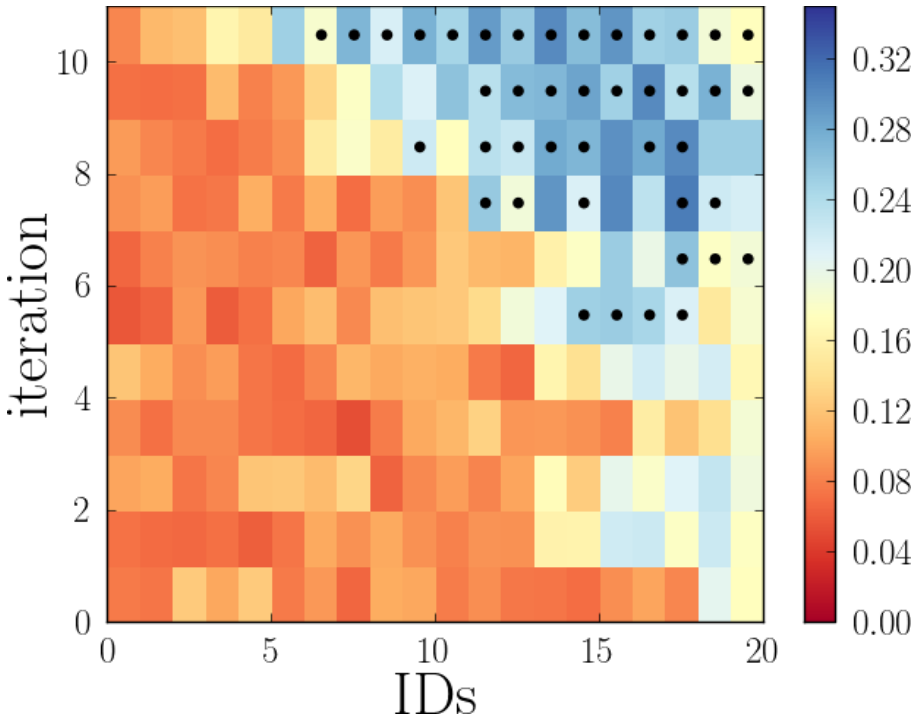

FIGURE 3.14: Time evolution of the $\bar{q}_6$ order parameter for every particle in the chain, with black dots highlighting particles that are identified as crystalline according to the alignment criterium. Every iteration corresponds to a single $\Delta t = \tau_D/20$. This graph was drawn by Francesco Turci.

about the 58% of the attaching chains in the interacting system are in contact with at least one other attaching chain, while only the 41% of the non-interacting cylinders on the same crystallite surface are. Snapshots of isolated (b) and multiple (c) attachment events are shown in the insets.

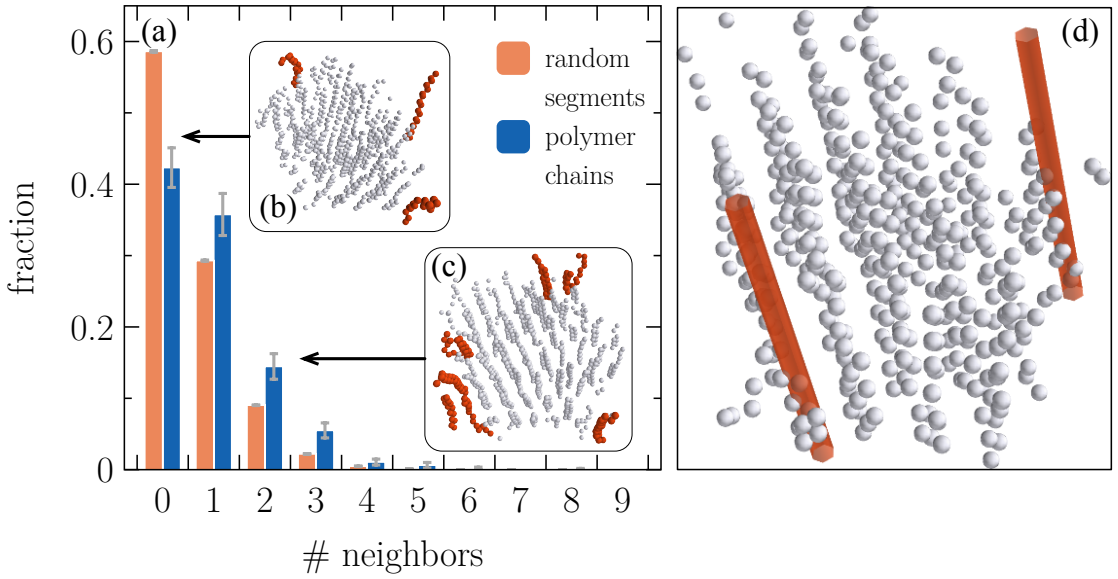

FIGURE 3.15: (a) Correlation between attachment events: The dark (blue) bars represent the distribution of neighboring attachment events as resulting from the analysis of 30 growth trajectories of length $30\Delta t$. The light (red) color bars represent the distribution of neighboring attachment events for a Monte-Carlo sampling of non-interacting cylinders attached at random sites picked uniformly on the surface of the crystal. Simultaneous attachment of neighboring chains is more likely to occur in the interacting system than in the non-interacting system. (For detailed definition of terms, please see main text.) Isolated (b) and multiple (c) attachment events are shown in the insets. (d) Schematic illustration of a configuration of random segments placed at the surface of the crystalline cluster. Their direction corresponds to the average direction of the end-to-end vectors of the cluster chains. This graph was drawn by Francesco Turci.

3.6 Conclusions

In this chapter we have presented the crystallization mechanism in short chain alkanes based on molecular dynamics simulations. We have presented the cooling and heating curves of n-eicosane and have found that n-eicosane has large hysteresis at the high cooling and heating rates applied. We computed the critical nucleus size using a committor probability method and found that the critical nucleus is of cylindrical shape and consists of 80 ± 20 monomers. We have shown that nucleation rates slightly change by changing the system size from 150 chains to 500 chains at 250 K and at 1 atmospheric pressure. The nucleation rates increase with a decreasing degree of supercooling. For primary nucleation we have shown that the chains which form the critical nucleus first align, then straighten, and finally form the local crystal structure. The growth of the crystal advances mainly through a *sliding-in* process on the lateral surface, which takes place in a correlated way, i.e. chains tend to get attached in clusters.

Chapter 4

Crystal Nucleation of n-Eicosane under Shear Flow

In this chapter, we study the homogeneous nucleation process of n-eicosane(C20) using molecular dynamics simulations under imposed shear flow conditions. Simulations were performed under constant volume and constant temperature (NVT) conditions. In the beginning of this chapter, we provide the description of the methods used to impose the shear flow and then the method of thermostatting. We make mean first passage time calculations to define the critical nucleus size at different shear rates. We report the effects of flow and temperature on the critical nucleus size and on the nucleation rates. We also illustrate the nucleation mechanism in short chain alkanes under shear conditions. At the end of this chapter, we compute the shear viscosity during the formation of the critical nucleus and a little beyond the nucleation event, to show the response of the system to the formation of the nuclei.

4.1 Introduction

The polymer science community has put a lot of effort in the last few decades in understanding the crystallization of polymers. Experimentally, crystallization of polymers has been addressed under quiescent conditions [5–14] and under the application of external fields [3, 58–65] and many features of the process have been identified. But due to resolution issues the mechanism of homogeneous crystal nucleation has not been identified yet.

Molecular dynamics simulation is a useful tool to understand the molecular mechanisms for crystal nucleation and growth. It has been extensively used to study the crystallization of polymers under quiescent conditions [43, 45–53] and under the influence of external field [3, 58–65]. When molecular dynamics simulations are used to study homogeneous crystal nucleation, one of the main problems is the long waiting time and even with today's high performance computers it is not possible to compute homogeneous nucleation rates at a low degree of supercooling. Keeping in mind this difficulty, Graham and Olmsted [31] developed a kinetic Monte Carlo method to observe homogeneous nucleation within an accessible time limit at a lower degree of supercooling. Unfortunately there are two remarkable deficiencies in this model. Under shear, the model gives an ensemble averaged chain stretch, whereas occasional rare fluctuations of high stretch could have a significant effect on the nucleation rate. Secondly, it can not handle polydispersity which is important from experimental point of view [33]. An analytic model for calculations of nucleation rates is also proposed [120] which supports the Graham and Olmsted kinetic Monte Carlo model [31]. Graham [121] has reviewed the molecular modeling of the flow induced crystallization and Benjamin et al. [122] has reviewed the formation of precursor structure during the flow induced crystallization in polymer from different experimental techniques in a very comprehensive way.

It is believed that the flow imposed by the external field (shearing or elongation) stretch and orient the polymer molecules in a specific direction. This orientation of molecules in a specific direction promotes alignment. This alignment then increases the number of stable nuclei and enhances the crystallization kinetics [16, 121]. The main results of this chapter are published in The Journal of Chemical Physics [123].

4.2 Molecular dynamics simulations under flow

There are two main issues in molecular dynamics simulations under flow. The first is the imposition of shear mechanically and pumping of energy into the system constantly to enforce the shearing. The second issue is extraction of the heat generated by the friction from the system using an appropriate thermostat. There are three main recognized techniques to impose the shear on the system.

Surface driven method

This method is used to induce flow in a fluid confined between two parallel plates. If one of these parallel plates moves with respect to the other, then the flow induced in this way is called planar Couette flow. If the flow is generated by a pressure gradient then the flow is called planner Poiseuille flow. One of the drawbacks of these methods is surface effects. In simulations we need very large system to avoid finite size effects when using surface driven methods.

Reverse non equilibrium molecular dynamics

In this method the cause and effect picture which is customarily used in non equilibrium molecular dynamics is reversed. The momentum flux or stress, which is the 'effect' in non equilibrium simulations is imposed; whereas the velocity gradient or shear rate which is the 'cause' in non equilibrium simulations is calculated from the simulation [124]. This method involves exchange of particles' momenta, therefore the total energy and linear momenta can be conserved. This method does not need coupling to an external temperature bath.

Homogeneous shear method

In molecular dynamics simulations, small systems are simulated using periodic boundary conditions to eliminate surface effects and to mimic the bulk material.

Lees and Edwards [125] proposed a method by using the periodic boundary conditions to study the system under flow conditions.

To simulate the system under shear, we use Lees Edwards boundary conditions [125]. When using standard periodic boundary conditions, the simulation box called the primary cell is surrounded by its own replicas. The boxes surrounding the primary cells have images of the same particles and once a particles leaves the primary simulation cell from one face, its image particle enters from the opposite face. A 2D figure that illustrates the Lees Edwards periodic boundary conditions is shown in FIG 4.1.

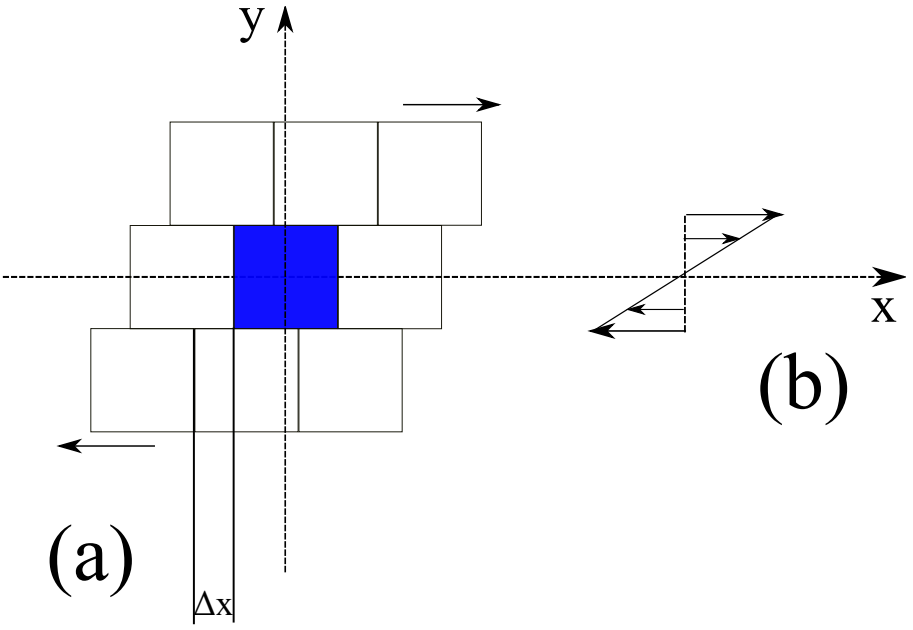

FIGURE 4.1: 2D sketch of Lees Edwards periodic boundary conditions. (a): Lees Edwards periodic boundary conditions, (b): Time averaged velocity profile generated by the shear flow.

This works in the same way as standard periodic boundary conditions in the x and z directions but is different from standard periodic boundary conditions in the y-direction, in that replica particles are also displaced with a distance and velocity U_x given by the

$$\triangle x = \dot{\gamma} L_y \triangle t, \tag{4.1}$$

$$U_x = \dot{\gamma} L_y \tag{4.2}$$

$\triangle x$ the displacement of y-direction replicas along the x-direction, $\dot{\gamma}$ is the applied shear rate, L_y is the box size in the y-direction and $\triangle t$ is the simulation timestep. The linear velocity profile is induced by the motion of the particles above and below the primary cell. If the particles have positions $(\mathbf{r}_x, \mathbf{r}_y, \mathbf{r}_z)$ and velocities $(\mathbf{v}_x, \mathbf{v}_y, \mathbf{v}_z)$, and the box dimensions are (L_x, L_y, L_z), then the new positions $(\mathbf{r}_x^{'}, \mathbf{r}_y^{'}, \mathbf{r}_z^{'})$ and velocities $(\mathbf{v}_x^{'}, \mathbf{v}_y^{'}, \mathbf{v}_z^{'})$ can be written as:

$$r_x^{'} = \begin{cases} (\mathbf{r}_x + \triangle x) \bmod L_x, \ \mathbf{r}_y \geq L_y, \\ \mathbf{r}_x \bmod L_x, \ 0 \leq \mathbf{r}_y < L_y, \\ (\mathbf{r}_x - \triangle x) \bmod L_x, \ \mathbf{r}_y < 0, \end{cases} \tag{4.3}$$

$$\begin{aligned} \mathbf{r}_y^{'} &= \mathbf{r}_y \bmod L_y, \\ \mathbf{r}_z^{'} &= \mathbf{r}_z \bmod L_z, \end{aligned} \tag{4.4}$$

$$\mathbf{v}_x^{'} = \begin{cases} (\mathbf{v}_x + U_x), \ \mathbf{r}_y \geq L_y, \\ \mathbf{v}_x, \ 0 \leq \mathbf{r}_y < L_y, \\ (\mathbf{v}_x - U_x), \ \mathbf{r}_y < 0, \end{cases} \tag{4.5}$$

$$\begin{aligned} \mathbf{v}_y^{'} &= \mathbf{v}_y, \\ \mathbf{v}_z^{'} &= \mathbf{v}_z. \end{aligned} \tag{4.6}$$

4.3 Thermostatting

We used the dissipative particle dynamics (DPD) thermostat to control the temperature. Dissipative particle dynamics was first presented by Hoogerbrugge and Koelman [89]. It is a combination of molecular dynamics, lattice gas atomata and Langevin dynamics. The system evolves in time in the same way as in molecular dynamics simulations described by Newton‘s equations of motion:

$$\begin{aligned} \dot{\mathbf{r}}_i &= \mathbf{v}_i \\ \dot{\mathbf{v}}_i &= \frac{\mathbf{f}_i}{m_i} \end{aligned} \tag{4.7}$$

where $\mathbf{r}_i$, $\mathbf{v}_i$, m_i and $\mathbf{f}_i$ are position, velocity, mass and force respectively of particle i, i = 1 to N denotes the number of particles. This is the same as normal molecular dynamics. The force $\mathbf{f}_i$ in the case of dissipative particle dynamics consists of three parts:

$$\mathbf{f}_i = \sum_{j \neq i} (\mathbf{F}_{ij}^C + \mathbf{F}_{ij}^D + \mathbf{F}_{ij}^R) \tag{4.8}$$

$$\mathbf{F}_{ij}^D = -\gamma \omega^D(r_{ij})(\hat{r}_{ij}.\mathbf{v}_{ij})\hat{r}_{ij} \tag{4.9}$$

$$\mathbf{F}_{ij}^R = -\sigma \omega^R(r_{ij})\xi_{ij}\hat{r}_{ij} \tag{4.10}$$

where $\mathbf{F}_{ij}^C$ is a conservative force, $\mathbf{F}_{ij}^D$ is a dissipative force, $\mathbf{F}_{ij}^R$ is a random force, where γ is frictional force, σ is stochastic force, $\mathbf{r}_{ij} = \mathbf{r}_i - \mathbf{r}_j$ is relative position, $\hat{r}_{ij} = \mathbf{r}_{ij}/|\mathbf{r}_{ij}|$, $\mathbf{v}_{ij} = \mathbf{v}_i - \mathbf{v}_j$ is relative velocity, ξ_{ij} are symmetric Gaussian random variables with zero mean and unit variance and ω^D and ω^R are weight functions.

For a Boltzmann distribution to be the stationary distribution we have to fulfill the following two conditions, first one is the relationship between stochastic and dissipative terms via temperature described by the fluctuation dissipation theorem.

$$\sigma^2 = 2\gamma k_B T \tag{4.11}$$

where k_B is the Boltzmann constant and T is temperature of the system.

and the second condition is for the weight functions,

$$\omega^D(r_{ij}) = \left[\omega^R(r_{ij})\right]^2 \tag{4.12}$$

$$\omega^R(\mathbf{r}_{ij}) = \begin{cases} 1 - r_{ij}/r_c, & \text{for } \mathbf{r}_{ij} \leq r_c \\ 0, & \text{for } r_{ij} > r_c \end{cases} \tag{4.13}$$

Where r_c is cut-off radius.

As thermostatting is done on relative velocities, Galilean invariance is satisfied. Consequently, the total momentum is also conserved.

When the DPD thermostat is used with Lees Edwards periodic boundary conditions, the velocities of particles which are modified by the Lees Edwards boundary conditions are changed by the dissipative force term of DPD thermostat. As a consequence, the flow velocity does not correspond to the given shear rate. In order to avoid this problem, the dissipative force F_{ij}^D term in DPD thermostat was modified as [126]:

$$\mathbf{v}_{ij}^{*\alpha} = \mathbf{v}_{ij}^{\alpha} - \frac{\dot{\gamma}}{L}\mathbf{r}_{ij}^{\beta} \tag{4.14}$$

$$\mathbf{F}_{ij}^D(\mathbf{v}_{ij}^{\alpha}) := \mathbf{F}_{ij}^D(\mathbf{v}_{ij}^{*\alpha}). \tag{4.15}$$

Where $\mathbf{v}_{ij}^{*\alpha}$ is laminar flow velocity, $\mathbf{v}_{ij}^{\alpha}$ is the pairwise velocity parallel to the laminar flow field, $\mathbf{r}_{ij}^{\beta}$ is the component of pairwise separation perpendicular to the flow field in the shear plane and L is the length of simulation box. This modification preserves the linear velocity profile in the system which corresponds to the given shear rate.

4.4 Simulation details

We performed molecular dynamics simulations of a system consisting of 500 chains of n-eicosane (C20). We equilibrated the system at 450 K which is well above the melting temperature of n-eicosane (C20). The equilibrium melting temperature of n-eicosane (C20) in this model has been reported 310 ± 2 K by Yi et.al [39], which is in agreement with experimentally observed melting temperature of n-eicosane (C20). We choose the density of metastable melt n-eicosane (C20) at 1 atm pressure and at corresponding temperature given in Table 4.1. We performed all simulations under constant volume and constant temperature conditions.

To study the effects of flow on the crystallization, we quenched these configurations from 450 K to 250 K and applied a shear rate $\dot{\gamma}$ to observe the nucleation event. We ran simulations at seven different shear rates ranging from $0.000001\tau^{-1}$ to $0.01\tau^{-1}$ ($0.95 * 10^{10} sec^{-1}$ to $0.95 \times 10^{6} sec^{-1}$). We also performed simulations at zero shear rate for comparison, we find no difference in the nucleation rate at the lowest shear rate and at zero shear rate.

To see the temperature effects on the nucleation rate under shear flow, we run simulations at seven different temperatures ranging from 250 K to 280 K at shear rate of $0.95 \times 10^{9} sec^{-1}$. In all these cases we quenched the system from 450 K to a given temperature and the density corresponding to every temperature at 1 atm pressure is given in the Table. 4.1.

TABLE 4.1: Density of metastable melt of n-eicosane at 1 atmospheric pressure and at given temperature. These densities were used for NVT simulations.

Temperature $[K]$	Density $[g/cm^3]$	Reference
250	0.836	*
255	0.833	**
260	0.830	**
265	0.828	*
270	0.825	**
275	0.822	**
280	0.819	*

* These densities are taken from Yi et al. [39]
** These densities are calculated by linear interpolation using data from [39].

We used the DPD thermostat [127] with the friction coefficient $\gamma = 1.0\tau^{-1}$; where τ is the MD simulation time step. We used the ESPResSo package [71] for simulations and implemented as custom features the dihedral potential, the Lees-Edwards periodic boundary conditions and crystallinity order parameter which were not present in the package by default.

4.5 Results & discussion

4.5.1 Velocity profile

As we mentioned before that there are two main concerns in NEMD simulations, first the method of enforcement of shear flow and secondly the extraction of heat using an appropriate thermostat. We ran simulations of an n-eicosane melt of density 0.836 g/cm^3 at 450 K at $\dot{\gamma} = 0.01\tau^{-1}$. We show the velocity profile of the system, the linear velocity profile verifies the homogeneous nature of the flow. This is shown on left side of FIG. 4.2. The blue circles show the data points from the simulations and the red line is a linear fit to these points. On right side of the FIG. 4.2, we show the temperature of the system as it evolves, this curve shows that the DPD thermostat is effectively controlling the temperature of the system.

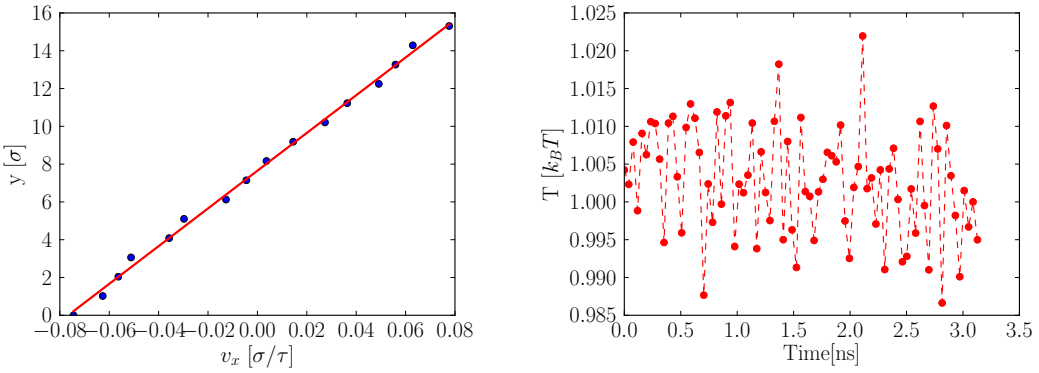

(A) (B)

FIGURE 4.2: Left: The velocity profile of the system is shown on left side. Blue points are from the simulations and red line is from linear fitting. Right: Temperature of the system is shown as the system evolves in time.

4.5.2 Nucleation rates

To monitor the nucleation event we used the crystallinity order parameter. We made a mean first passage time (MFPT) analysis [97] in order to estimate the induction time, this approach is an alternative equivalent to the growth probability/committor analysis [101] also used to analyze the cluster growth history [97]. We have provided detailed description of the mean first passage time in Chapter 2. MFPT has been used in studies of glass forming system under shear [98, 99] and n-alkanes of C8, C20 and C150 by Yi et.al [38–40].

We compute the induction time at different shear rates and show this in FIG. 4.3. The induction time and the visualization of the critical nucleus formed at different shear rates show that there are two different regions (see FIG. 4.3). We divide the effects of the shear rates on the induction time and orientation of critical nucleus in two regions. In first region, the shear rate has no effect on the induction time and the chains which form the critical nucleus are not oriented in the direction of flow, instead they are oriented in random direction, as for nuclei under quiescent conditions. In this region the flow is not strong enough that it can have any effect on the induction time. In the second region, the shear rate has a significant effects on the induction time and the nuclei formed in this region are oriented in the direction of flow. In this region, the induction time decreases as a power law in the shear rate. This observation agrees with experimental results [19, 128] as well as with the theoretical work by Grizzuti and coworkers [19, 129]. Based on the assumption that shear can only affect nucleation if the sheared chains do not have enough time to relax back into their equilibrium structure, the crossover is expected to occur at Weissenberg number $\tau_{\max}\dot{\gamma}_c \approx 1$, where $\tau_{\max}$ is the longest relaxation time in the system, and $\dot{\gamma}_c$ is the critical shear rate, at which the induction time begins to drop. In our simulation data (see in fig. 4.3) $\dot{\gamma}_c$ can be estimated from the intersection of the line (continuous) drawn through the induction time data at high shear rates and a horizontal line (dashed) at the value of the induction time under quiescent conditions ($\dot{\gamma} = 0$). If we assume that the center of mass diffusion of a chain across its own radius of gyration is the slowest relevant process in the system, we find $\tau_{\max}\dot{\gamma}_c = 0.6$ (where $\tau_{\max} = 1.26 \times 10^7\tau$), which confirms the assumption (Here, we have used the time a chain needs to diffuse over the length of its radius of gyration as an estimate of $\tau_{\max}$.). This region can further be divided into two subregions, at

the highest shear rate $0.01\tau^{-1}$ ($0.95 \times 10^{10} sec^{-1}$), a nucleus of up to few hundred monomers (maximum 12 hundred monomer units in one trajectory is observed) is formed and then just break down and again a nucleus of few hundred monomers forms and breaks. This formation and breaking can be seen in the FIG. 4.4, the black curve shows the formation and breaking of the cluster at this shear rate. At all other shear rates, the cluster continued growing to the end of the simulations.

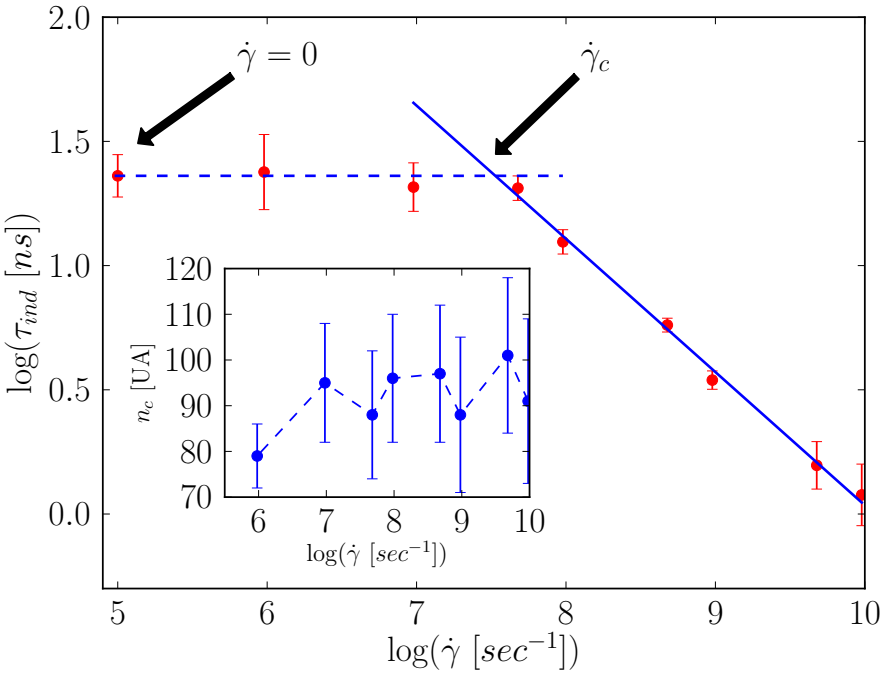

FIGURE 4.3: In the main figure log-log of induction time vs shear rate is shown and in the inset critical nucleus size against log of shear rate is shown.

In the inset of FIG. 4.3, the critical nucleus size against different shear rates is shown, which appears unchanged. In a single component glass forming system Mokshin et al. [99] observed that at low shear rates critical nucleus size remains unchanged, at higher shear rates the nucleus shape becomes prolate and the size of the nucleus increases with increase in shear rates. In our case because the nucleus is already of a cylindrical shape, its size does not increase with the increase in shear rate.

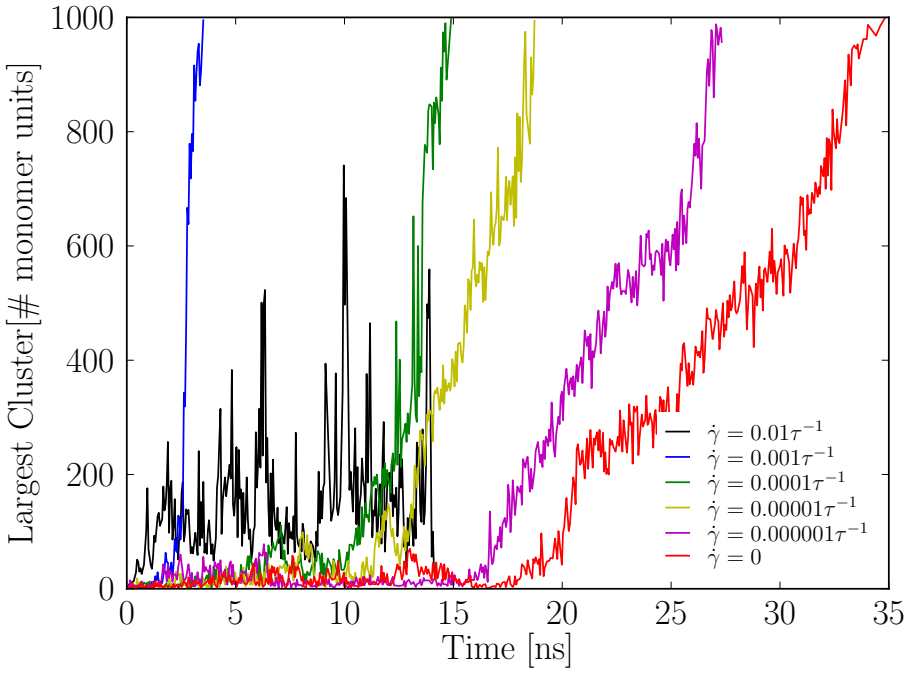

FIGURE 4.4: Evolution of the largest cluster size at different shear rates. The evolution the largest cluster size from a single trajectory at every shear rate is shown. The black curve shows the evolution of the largest cluster size at the highest shear rate and the red curve shows the evolution of the largest cluster under quiescent conditions.

In order to see the effect of temperature on the nucleation rate and on the critical nucleus size, we performed simulations at seven different temperatures ranging from 250 K to 280 K at shear rate of $\dot{\gamma} = 0.001\tau^{-1}$ $(0.95 \times 10^9 sec^{-1})$. We show the nucleation rates versus temperature in the main FIG. 4.5. The nucleation rate decreases with increase in temperature. The nucleation rate increases from $(21.63 \pm 6.4) \times 10^{25}$ $cm^{-3}sec^{-1}$ to $(102.85 \pm 4.26) \times 10^{25}$ $cm^{-3}sec^{-1}$ when we change temperature from 275 K to 250 K, which is only factor of 5. The flow effect on the nucleation rate is dominant over temperature effects and this observation is similar to that of experimental observations [19, 128] at higher shear rates. The chains align primarily because they are sheared, and only secondarily because of the chemical potential difference between the bulk crystal and the bulk metastable melt.

In the inset of FIG. 4.5 we show the critical nucleus size at different temperatures.

The critical nucleus size remains constant within statistical uncertainties at this shear rate and for this range of degree of supercooling. We have also run simulations at 280 K but we did not see nucleation events at this lower degree of supercooling and this shear rate. As shear is the dominating driving force for crystallization at $\dot{\gamma} = 0.001\tau^{-1}$ $(0.95 \times 10^9 sec^{-1})$, the size of the critical nucleus depends only weakly on temperature.

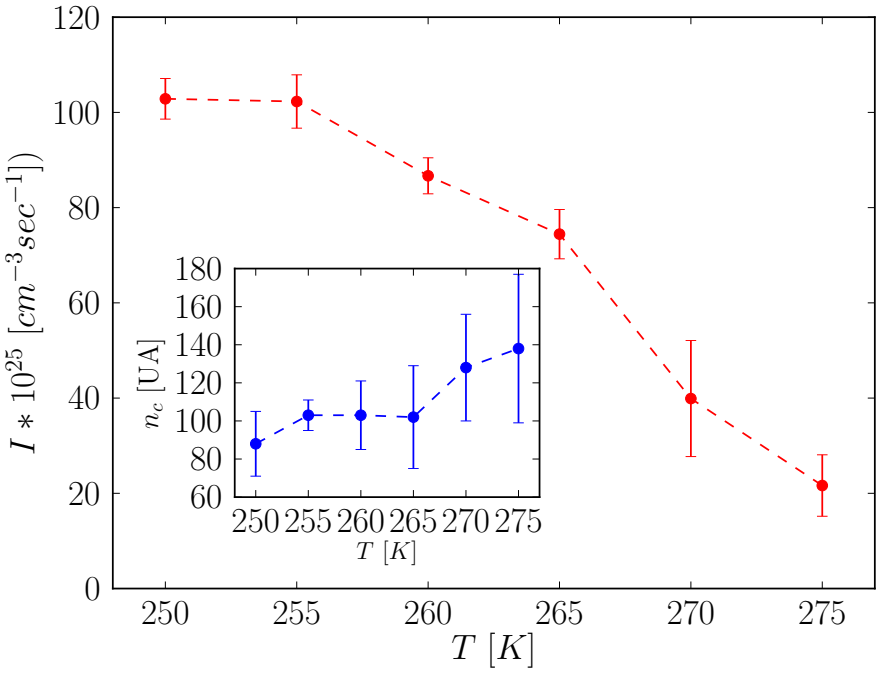

FIGURE 4.5: Nucleation rate versus temperature under shear flow is shown in the main figure. In the inset critical nucleus size against temperature is shown at the same shear rate.

4.5.3 Nucleation mechanism

To study the nucleation mechanism we analyze 10 independent trajectories for every shear rate in terms of the average radius of gyration R_g of all chains that are part of the nucleus at t_0, the global alignment S_2 of these chains, the average volume V of the Voronoi [119] cell associated to each particle that is part of the nucleus, its crystallinity order parameter and the average local bond order parameter $\bar{q}_6$.

In Fig. 4.6 we show the relative variations of these quantities with respect to the values they had at $-100\Delta t$, $-70\Delta t$, $-35\Delta t$ and $-10\Delta t$ at shear rates $\dot{\gamma} = 0.00001\tau^{-1}(0.95 \times 10^8 sec^{-1})$, $\dot{\gamma} = 0.0001\tau^{-1}(0.95 \times 10^9 sec^{-1})$, $\dot{\gamma} = 0.001\tau^{-1}(0.95 \times 10^9 sec^{-1})$ and $\dot{\gamma} = 0.01\tau^{-1}(0.95 \times 10^{10} sec^{-1})$ respectively.

Approaching the formation of the critical nucleus at t_0, at $\dot{\gamma} = 0.00001\tau^{-1}$, we observe first an increase in the global orientational order S_2, then an increase in the radius of gyration and in the local density, and finally local positional and orientational order are established. When we compare these results with our previous results for short polymer chains [42] under quiescent conditions, we find that the nucleation mechanism is initiated by the global alignment of the chains under quiescent and under shearing conditions.

At $\dot{\gamma} = 0.0001\tau^{-1}$ and at higher shear rates, we observe an increase in the global orientational order S_2 and an increase in the radius of gyration R_g simultaneously. Once chains are straightened and aligned, with an increase in local density the local positional and the orientational order are established. We conclude that the nucleation mechanism is the same under quiescent conditions and at low shear rates but at higher shear rates the straightening and alignment occur simultaneously instead of sequentially.

We compute *averaged local bond order* (ALBO) *parameters* to see the positional order and we show the evolution of the entire distribution of $\bar{q}_6$ rather than just the average in Fig. 4.7, because the average is still dominated by the peak at liquid-like $\bar{q}_6$ at times when there is already a shoulder showing crystalline-like $\bar{q}_6$. We show this at $\dot{\gamma} = 0.001\tau^{-1}$.

In Fig. 4.8 we show the snapshots of the time evolution of the critical nucleus at shear rate of $\dot{\gamma} = 0.001\tau^{-1}$. The critical nucleus is formed at $t = t_0$. At time

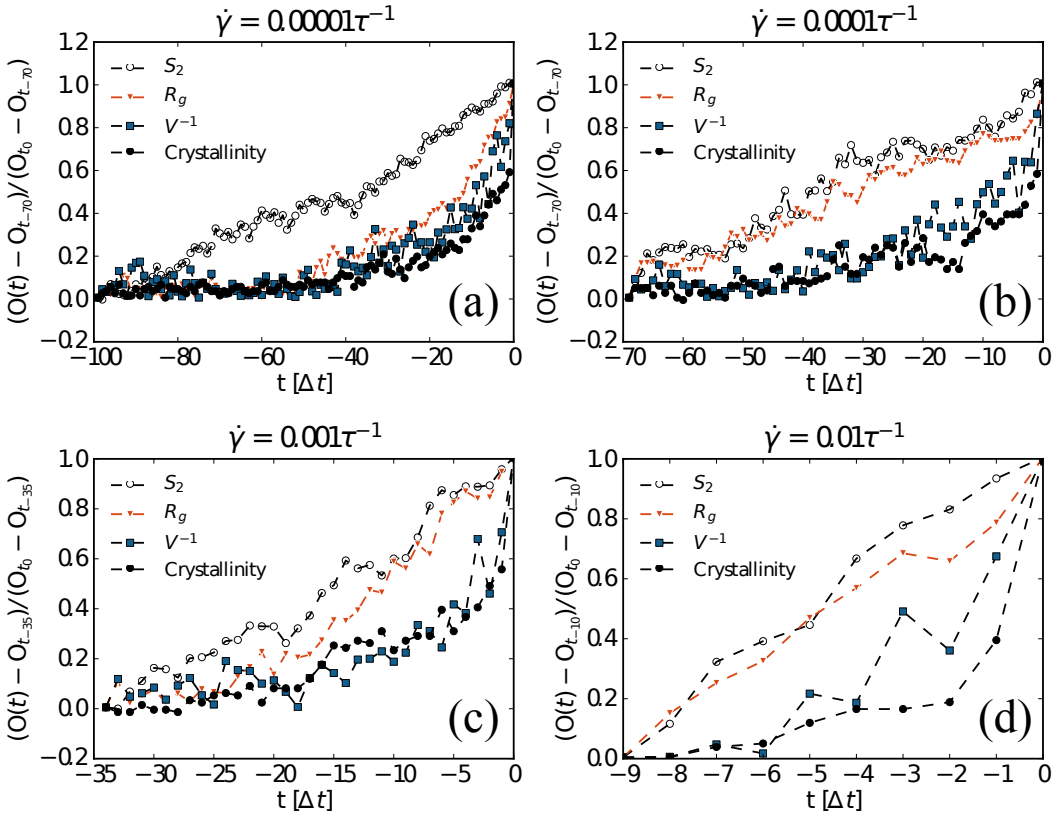

FIGURE 4.6: Relative variation of several observables (O) from the melt to the formation of a critical nucleus for the particles involved in the nucleus: the orientation order parameter S_2 (black, open circle), the inverse of the Voronoi cell volume V (blue, square) and the crystallinity order parameter (black, closed circle). (a) : $\dot{\gamma} = 0.00001\tau^{-1}$, (b) : $\dot{\gamma} = 0.0001\tau^{-1}$, (c) : $\dot{\gamma} = 0.001\tau^{-1}$, (d) : $\dot{\gamma} = 0.01\tau^{-1}$. The curves are averaged over 10 independent trajectories progressing backward in time from the nucleation time $t = t_0$ in steps Δt to $t = -100\Delta t$, $t = -70\Delta t$, $t = -35\Delta t$ and $t = -10\Delta t$ at $\dot{\gamma} = 0.00001\tau^{-1}$,$\dot{\gamma} = 0.0001\tau^{-1}$, $\dot{\gamma} = 0.001\tau^{-1}$ and $\dot{\gamma} = 0.01\tau^{-1}$ respectively.

$t = t_{-35}$, the chains are not aligned with each other and then at time $t = t_{-5}$, the chains are aligned with each other but not packed closely, which occur in last steps and critical nucleus is formed.

Under shear flow, the chains are straightened on the local level and are oriented in the direction of flow. We find that at $\dot{\gamma} < \dot{\gamma}_c$ the nuclei are oriented in any random direction, while at $\dot{\gamma} > \dot{\gamma}_c$ the nuclei are oriented on average in the direction of flow, i.e. the stems are parallel to the flow field. In Fig. 5.5, we show the average tilt angle of the critical nucleus with respect to the flow field at different shear rates. With

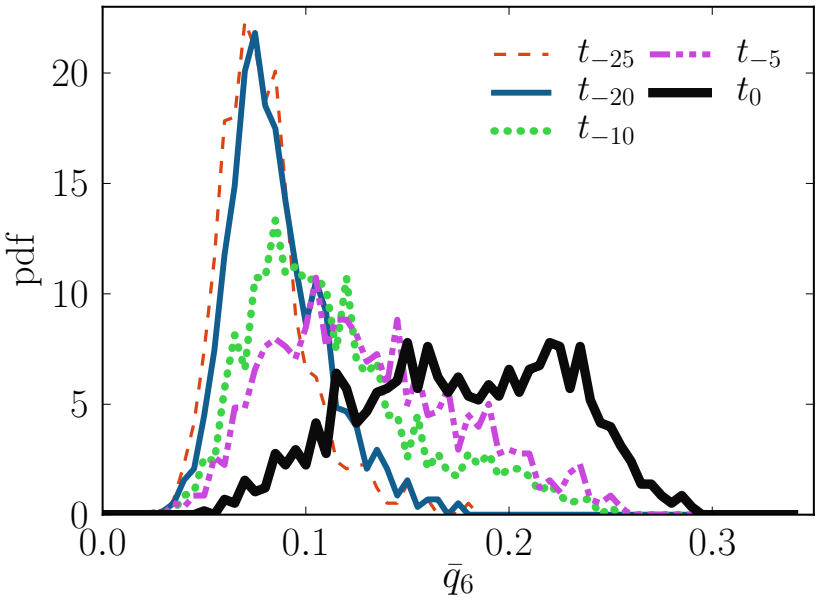

FIGURE 4.7: Probability distributions of the averaged local bond order parameter $\bar{q}_6$ computed at different times for those particles that form the crystallite at t_0.

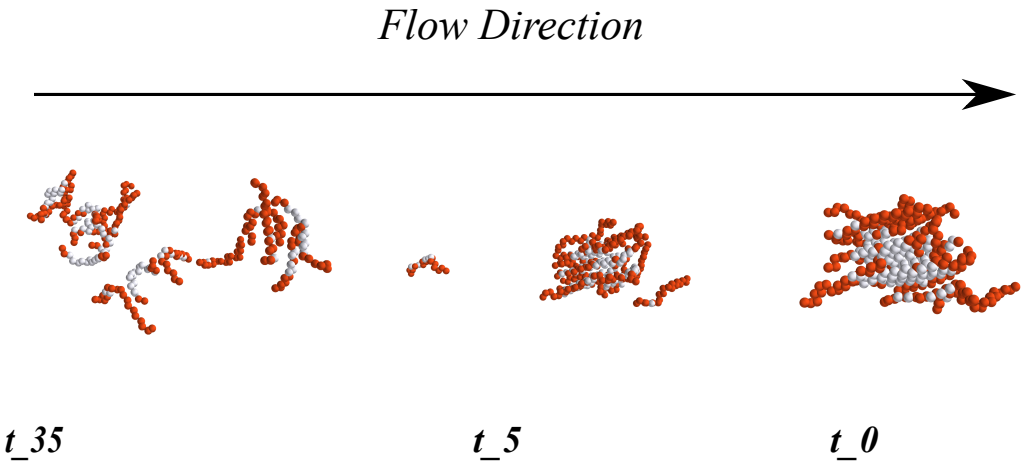

FIGURE 4.8: Time evolution of a critical nucleus at $dot\gamma = 0.001\tau^{-1}$. Red monomers are those monomers which themselves do not participate in the critical nucleus but belong to the chains which participate in critical nucleus, the gray monomers are monomers which participate in the formation of the critical nucleus.

increasing shear rate the alignment becomes stronger, this observation is similar to findings in studies by others of short polymer chains [130, 131].

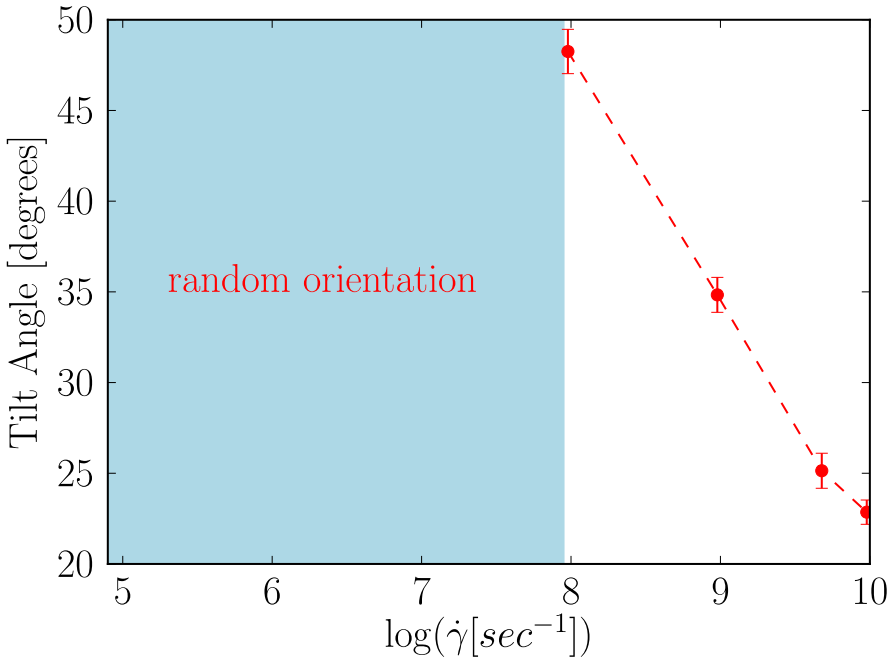

FIGURE 4.9: Average tilt angle between the critical nucleus and the flow direction versus the logarithm of the shear rate. The light blue rectangle shows that the critical nuclei are oriented in random directions, as for quiescent conditions

In order to see the structure of the nuclei formed we visualize the critical nucleus at different shear rates and observe no significant difference in the snapshots at the studied shear rates. We show snapshots of the critical nuclei at shear rates of $(a) : \dot{\gamma} = 0\tau^{-1}$, $(b) : \dot{\gamma} = 0.00001\tau^{-1}$ and $(c) : \dot{\gamma} = 0.001\tau^{-1}$ in Fig. 4.10. We do not see any elongated nuclei at any shear rate.

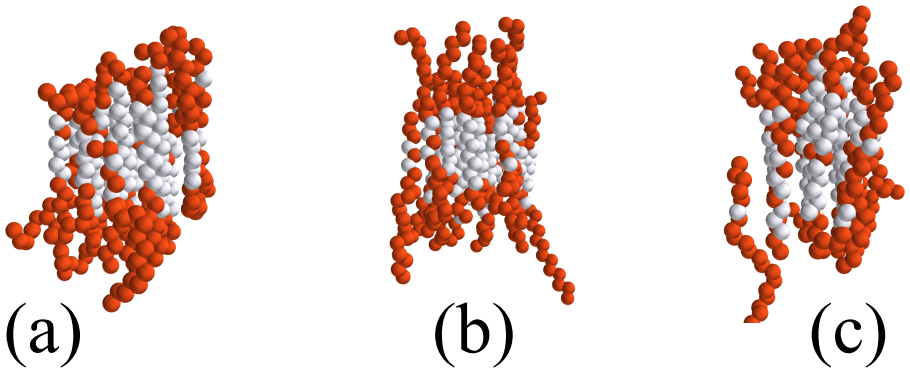

FIGURE 4.10: Snapshots of critical nuclei at different shear rates. The red monomers are those monomers which themselves do not participate in the critical nucleus but belong to the chains which participate in critical nucleus, the gray monomers are monomers which participate in the formation of the critical nucleus. $(a) : \dot{\gamma} = 0.0\tau^{-1}$, $(b) : \dot{\gamma} = 0.00001\tau^{-1}$ and $(c) : \dot{\gamma} = 0.001\tau^{-1}$.

4.5.4 Shear viscosity

We measure the response of the flowing fluid during the formation of clusters in terms of the shear viscosity. In molecular dynamics simulations under flow, the shear viscosity can be computed using the following relationship;

$$\eta = -\frac{\langle \mathbf{P}_{xy} \rangle}{\dot{\gamma}} \tag{4.16}$$

Here η is the shear dependent viscosity, $\mathbf{P}_{xy}$ is the xy component of the pressure tensor and $\dot{\gamma}$ is the imposed system average shear rate. The pressure tensor for a molecular system can be written as;

$$\mathbf{P}_{\alpha\beta}(t) = \frac{1}{V}\left[\sum_{i}^{N} m\ \mathbf{v}_{i\alpha}(t)\mathbf{v}_{i\beta}(t) + \sum_{i}^{N}\sum_{j>i}^{N} \mathbf{r}_{ij\alpha}(t)\mathbf{f}_{ij\beta}(t)\right] \tag{4.17}$$

On the right hand side of the Eq. 4.17, the first summation term is the kinetic contribution and the second term is the potential contribution to the pressure tensor. The i represent the particles index, $\alpha$and β represents the x, y and z components in the cartesian system. m_i is the mass of particle i, $\mathbf{v}_{i\alpha}$ and $\mathbf{v}_{i\beta}$ are the peculiar velocity (laboratory velocity minus mean flow velocity) components of particle i in

the α and β directions respectively. In the second summation term $\mathbf{r}_{ij\alpha}$ represents the α component of the distance vector between particle i and j and $\mathbf{f}_{ij\beta}$ is the β component of the force exerted on the particles i by the particle j.

We show the trace of the pressure tensor (scalar pressure) as a function of cluster size in Fig. 4.11(a) and we show the shear viscosity as a function of cluster size in the Fig. 4.11(b) for a system consisting of 500 chains of C20, at 250 K and at shear rate of $0.001\tau^{-1}$. The black dots represent the simulation data points, the red dashed line shows the critical nucleus size, the white line represents the mean value of the viscosity and the green envelope around the white line represents the standard deviation in the shear viscosity. We do not observe any significant change in the viscosity during the formation of nucleus and growth up to cluster size of 450 monomers. After this cluster size scalar pressure started decreasing due to fact that the phase transition is occurring in the NVT ensemble. In rheometery experiments, an increase in the viscosity is considered as an indication of the onset of crystallization in polymer melt. It might be possible that small size crystallites are not detected by rheometery experiments and onset of crystallization is detected for the larger crystallites with an increase in the viscosity.

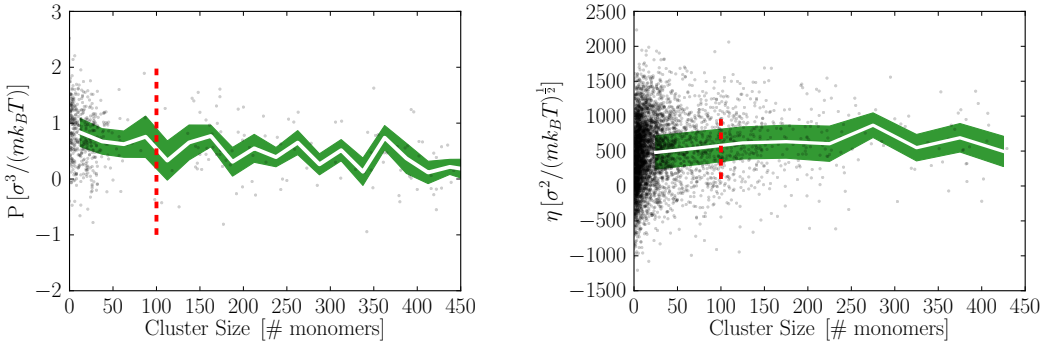

FIGURE 4.11: Left: Trace of the pressure tensor (scalar pressure) as a function of cluster size. Blue points are from the simulations and red line is from linear fitting. Right: Shear viscosity as a function of cluster size. The black dots represent the simulation data points, the red dashed line shows the point of critical nucleus, white line represents the mean value of the viscosity and the green envelop around the white line represents standard deviation in the shear viscosity.

4.6 Conclusions

We have studied the effect of flow and temperature on the nucleation rates and critical nucleus size. We have also analyzed the formation of the critical nucleus in a short chain alkane n-eicosane under shear flow. We have determined critical nucleus size via mean first passage time analysis and we compute induction time at different shear rates and at different temperatures, our results are in agreement with experimental results qualitatively. The critical nucleus size remains unchanged at different shear rates. The nucleation rates decreases with a decrease in degree of supercooling and the critical nucleus size remains constant within statistical uncertainties. The effects of flow on the nucleation mechanism has been studied and we observe that the nucleation mechanism at low shear rates is identical to what we observe under quiescent conditions and at higher shear rates an increase in the alignment and the stretching of chains occur together, then the local density is increased and the crystal structure is formed. We also compute the shear viscosity during the formation of critical nucleus and a little beyond the nucleation event and we do not observe any change in the shear viscosity as it is observed in rheometery experiments.

Chapter 5

Crystallization of C150 & Polyethylene

In this chapter, we study the homogeneous nucleation process in n- pentacontahectane (C150) and C500 under quiescent conditions, and C150 under shear conditions using molecular dynamics simulations. We perform simulations of n-pentacontahectane (C150) at a 30% degree of supercooling. We compute the critical nucleus size using a mean first passage time analysis. We find that the critical nucleus is of cylindrical shape and consists of straightened parts from a number of chains. We identify the microscopic mechanisms of homogeneous crystal nucleation under quiescent and shear conditions and we observe that chain segments first align and then straighten. The local density then increases, and finally the monomer units become ordered positionally. We show the nucleation rate dependence on the shear rate and estimate the critical shear rate. We also compute the shear viscosity of the system during the formation of clusters to see the response of the system to the formation of clusters. At the end of this chapter, we provide some results of crystallization of polyethylene (C500).

5.1 Introduction

Polymer crystallization involves the organization of chains from a coil like conformation to a folded crystal structure. In the last few decades, many theories have been proposed to address structure formation during the early stages of this process.

Doi et al. [24, 25] proposed the theory of micro-phase separation for polymer crystallization. This theory states that when a polymer melt is quenched, the conformations of chains change from *gauche* to *trans* states. This increases the persistence length of chains, which increases the excluded volume of the system and destabilizes the system. The system is stabilized by orienting the chain segments parallel to each other to minimize the excluded volume of the system. These orientational fluctuations induce the micro-phase separation.

After the observation in the 1990s of small angle X-ray scattering (SAXS) peaks during the induction time [5–7], a new debate about the presence of ordered melt before the onset of the nucleation event developed in the polymer science community. These peaks were first interpreted using Cahn Hilliard (CH) theory [23] and to the effect that these SAXS peaks were due to spinodal decomposition.

Olmsted and co-workers [26] reported a theory based on spinodal decomposition of the polymer melt to explain the emergence of these SAXS peaks before the emergence of a wide angle X-ray scattering (WAXS) peak. They coupled the two order parameters. These order parameters describes the density and the conformation of the polymer chains. They proposed a phase diagram and possible primary nucleation mechanism. The free energy consists of a density dependent and a conformation dependent term. In their proposed nucleation mechanism, an isotropic melt separates into a dense and more ordered melt and a less dense and less ordered melt. The dense and more ordered melt has lower free energy barrier for crystallization. They referred to phenomenon as “spinodal assisted nucleation”.

This idea of coupling of density and conformation is further extended by Hongge Tan et. al [132]. They added coupled terms of the density fluctuations and the conformation fluctuations via a mixed derivative term and a cross gradient term in Olmsted’s proposed model. They calculated structure factors using this model and found their results in close agreement with experimental results.

Kaji [27] proposed a model for polymer crystallization based on Doi [24, 25] theory and Olmsted [26] theory to explain these SAXS peaks. According to him, when a polymer melt is quenched below its melting temperature, the conformation of chains changes from the *gauche* to *trans* state. This change increases the persistence length (length of rigid segment/rod) of the chains which increases the excluded volume and destabilizes the system. To minimize the excluded volume and stabilize the system, these rigid segments then tend to align themselves. He characterizes the polymer crystallization as a two step process, in the first step the isotropic melt is separated into dense and more ordered (nematic) and less dense and less ordered domains. Depending on temperature this micro phase separation can be like a nucleation event or like a spinodal decomposition. In the second step a transition from nematic to smectic phase occurs. This second step corresponds to the SAXS peaks seen in the experiments.

Today, with the availability of high performance computers and the development of efficient algorithms, molecular dynamics simulations are being used extensively to understand the molecular mechanism of polymer crystallization under quiescent conditions [43, 45–53] and under flow or large deformation [3, 58–65], but most of these studies focus on the growth process under deformation. None of them provide the nucleation rate dependence on the shear rate or the temperature effects on the nucleation rates under flow or the nucleation mechanism under shear.

Muthukumar and his co-workers [54–56] performed Langevin dynamics simulations under quiescent conditions to study the early stages of crystallization of polymer. They observed the simultaneous development of local orientational ordering everywhere in the system followed by global restructuring. The thickening of lamellae was observed after formation of a single crystal. However, they studied crystallization from solution not from the melt.

Yamamoto and his co-workers [44] reported the primary nucleation mechanism under quiescent conditions for long chain alkanes C100, using molecular dynamics simulations. They studied the nucleation mechanism from a supercooled melt. They focused on the transformation of the random-coil into the folded chain conformations and on the structure of the supercooled melt.

Recently, Rutledge and co-workers [40] performed molecular dynamics simulations under quiescent conditions to study the crystallization in long chain alkanes and polyethylenefrom melt. However, they calculated the nucleation and growth rates and focused on the free energy landscape associated with the crystallization process rather than the microscopic mechanisms.

Graham and Olmsted [31] developed a kinetic Monte Carlo method to observe the homogeneous nucleation within accessible time limit at lower degree of supercooling. An analytic model for calculations of nucleation rates is also proposed [120] which supports the Graham and Olmsted kinetic Monte Carlo model [31].

In our previous chapters we studied the microscopic mechanism of primary nucleation and growth in short chain alkanes [42] under quiescent and shear conditions. In this chapter we study the primary nucleation mechanism in *n*-pentacontahectane (C150) under quiescent and shear conditions. We chose C150 because it is the minimum length for which we can capture the effects of entanglements [133–136] on crystallization and also for which a folded chain crystal structure can be observed. The main results of this chapter are published in the Journal of Chemical Physics [123].

5.2 Model & order parameters

We have used the same model that was used for n-eicosane (C20) and provided in Chapter 2. In order to apply the same order parameters described in Chapter 2, we first define the *chain segment*, which we use to compute the radius of gyration and nematic order parameter in this chapter. In our previous study of short chain alkanes (C20), we chose a complete chain as a single segment for computation of the average radius of gyration R_g and the global alignment S_2 but in the case of long chain alkanes it makes more sense to divide the whole chain in small segments as nucleation is a local event. Therefore, by considering every monomer unit i as a middle monomer unit we take seven monomer units on both sides. In this way every segment consists of 15 monomer units. We refer these segments as *chain segments* for further discussion. The order parameters which we use to present the nucleation mechanisms include the local density V^{-1} corresponding to every particle, the radius of gyration R_g of the *chain segment*, the nematic order parameter S_2 of the *chain segment*, the crystallinity order parameter and the local bond order parameter $q_6 q_6$. For the crystallinity order parameter, the threshold values for the cutoff radius r_c and the minimum number of aligned neighbors for a particle to be crystalline were computed and are shown in section 5.3.2. Two neighbors i and j are considered as "aligned" if the chains they belonged to locally are almost parallel ($\theta_{ij} \leq 10°$)).

5.3 C150 under quiescent conditions

5.3.1 Simulation details

We simulated a system of 100 chains of n-pentacontahectane (C150) at 280 K, which corresponds to a 30% degree of supercooling. We equilibrated the system at 500 K which is well above the melting temperature of n-pentacontahectane(C150). After equilibration we quenched these configurations from 500 K to 280 K to observe the nucleation event. The equilibrium melting temperature of n-pentacontahectane (C150) has been calculated by extrapolating the experimental data and reported as 396.4 K by Yi et.al [40].

We performed simulations under constant pressure and constant temperature conditions. In all these simulations pressure was fixed at 1 atmospheric pressure.

We use same units which we used for C20 under quiescent conditions in Chapter 3 and the integration timestep used in simulations is 0.006τ. We use a Langevin dynamics based thermostat and barostat which we used before in Chapter 3. We chose friction coefficient $\gamma = 1.0\tau^{-1}$ for the thermostat, and the piston mass for the barostat to be $0.00001m$.

We used the ESPResSo package [71] for simulations and implemented the dihedral potential, tail correction in both potential energy and pressure calculation and crystallinity order parameter; which were not present in the package by default.

5.3.2 Results & discussion

To observe the phase transition, we compute the *trans* states fraction in the whole system. The time evolution of the number of *trans* states is shown in FIG. 5.1. The dark gray line shows the simulation data. The number of *trans* states in the system first increases from 0.459 to 0.472 after quench from 500 K to 280 K and is shown with green line which is fit to the simulation data. The number of *trans* states in the system increases slightly from 0.472 to 0.476 during the induction time shown with a blue line which is a fit to simulation data and then it increases during the

crystal growth from 0.476 to 0.541 shown with red line fit. This figure (fig. 5.1) shows that when we change the temperature of the system, the number of *trans* states increases and reaches to a value which corresponds to the lower temperature, and then the number of *trans* states start increasing on the onset of crystallization. Therefore, the number of *trans* states can be used as an order parameter to identify the start of crystallization during the simulations.

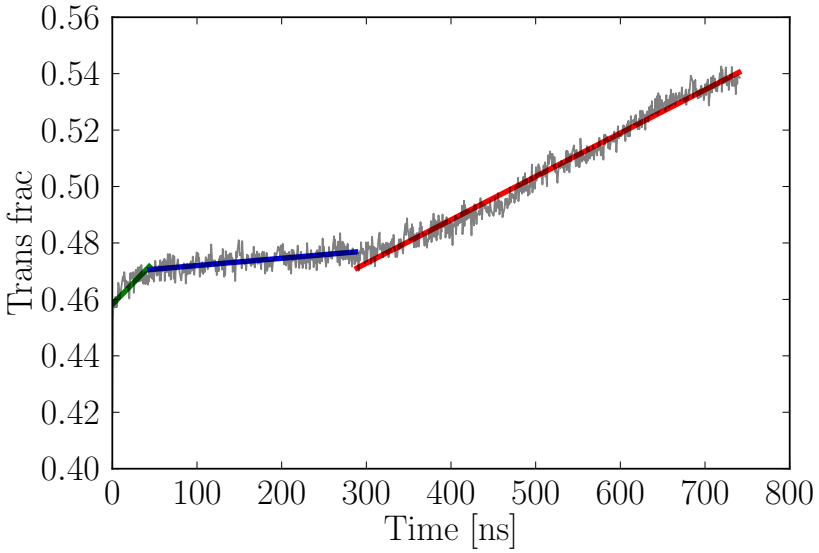

FIGURE 5.1: Time evolution of fraction of the number of *trans* states in the system. The dark gray line shows the simulation data, green line is a linear fit until the system stabilizes to 280 K after quench from 500 K, the blue line is a fit to the waiting time to nucleation event, in this region number of *trans* states in the system slightly increases and the red line shows the fit to the data when nucleation event occurs and number of *trans* states in the system increases.

Mean first passage time analyses (MFPT) [97] were performed on all trajectories to compute the nucleation time. The growth of the largest cluster size was computed using the crystallinity order parameter described in Chapter 2.

To observe the nucleation event we first optimized the parameters used in the calculations of cluster size. FIG. 5.2 shows the radial distribution function of the system at 280K. The first peak is at the distance of bond length, the second peak is at the distance of every second consecutive bead along the chains and the third peak is at the nearest neighbor distance for beads belonging to different chains.

We chose a cutoff of 1.4σ for counting the number of neighbors of every monomer unit in calculations of crystallinity order parameter and averaged local bond order parameter.

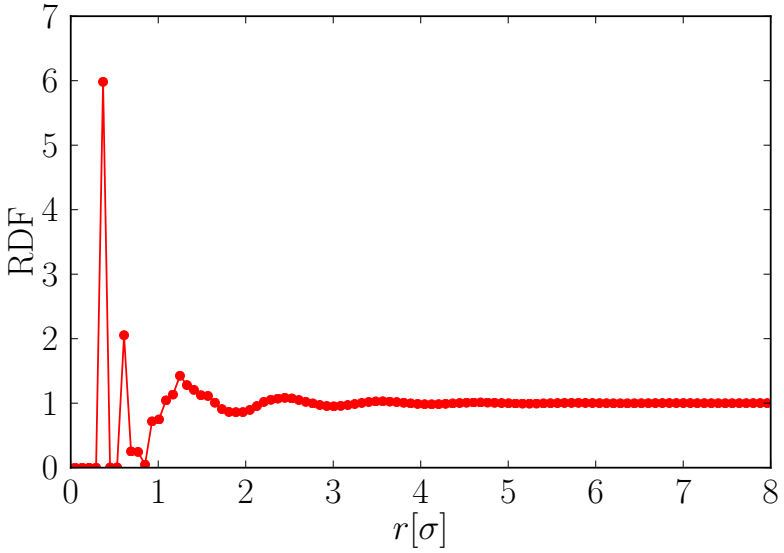

FIGURE 5.2: Radial distribution function.

To distinguish the crystal structure from the melt structure we computed the number of solid bonds for every monomer unit. We chose a melt and a partially crystallized configuration and computed the number of solid bonds for every monomer unit. The probability of finding solid bonds versus number of solid bonds is drawn in FIG. 5.3. We select 12 solid bonds as a threshold value for crystallinity order parameter. At this threshold value the probability to find a solid bond in the melt configuration goes to zero and we can separate the melt and crystal structure.

After optimizing the crystallinity order parameter, we show evolution of the largest cluster size from one trajectory in FIG. 5.4(A), and the mean first passage time in FIG. 5.4(B). The estimated values for induction time τ^* and the critical nucleus size n^* are given in Table 5.1. We find the nucleation rates to be in rough agreement with the results of Yi et al. [40]. As we were using slightly different system sizes, different barostats and thermostats, small differences in the results were expected.

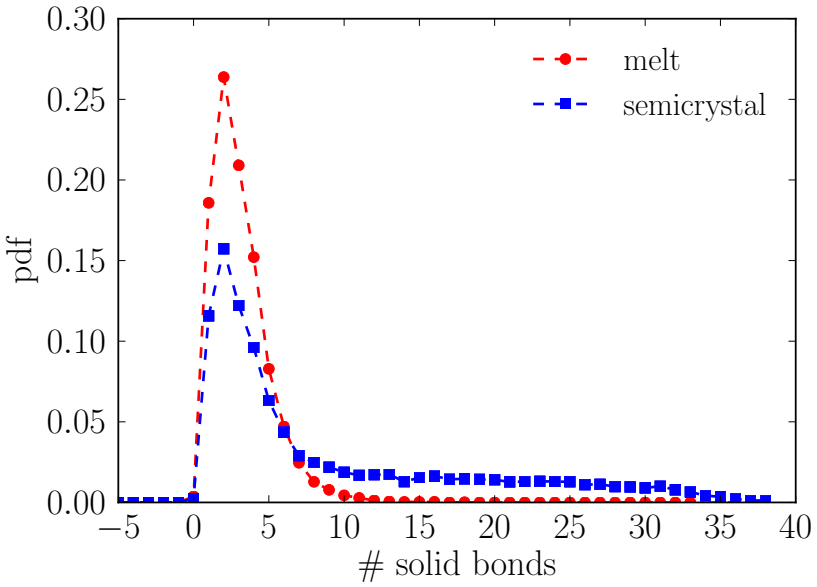

FIGURE 5.3: Probability distribution to find solid bonds for every particle. The red curve with circle symbol shows the probability of finding solid bonds in the melt configuration and the blue curve with square symbol shows the probability of finding solid bonds in the semicrystalline configuration.

TABLE 5.1: Fitting results of mean first passage time for C150.

System	Chain length	n^*(UA)	τ^*(ns)	$I(10^{25} cm^{-3} s^{-1})$
Yi.et .al [40]	150	143±14	293±19	1.47±0.10
Our Simulations	150	87±9	354±41	0.72±0.08

To analyze the nucleation mechanism, we identify in each trajectory those particles that are part of the critical nucleus at the nucleation time t_0. We then trace them backwards in time and compute their structural and orientational properties. We proceed backwards until structural and orientational properties of these particles are indistinguishable from the melt particles.

We analyzed 20 independent trajectories in terms of the average radius of gyration R_g of all *chain segments* that were part of the nucleus at t_0, the global alignment S_2 of these *chain segments*, the average volume V of the Voronoi[119] cell associated to each particle that is part of the nucleus, its crystallinity order parameter and the average local bond order parameter $\bar{q}_6$.

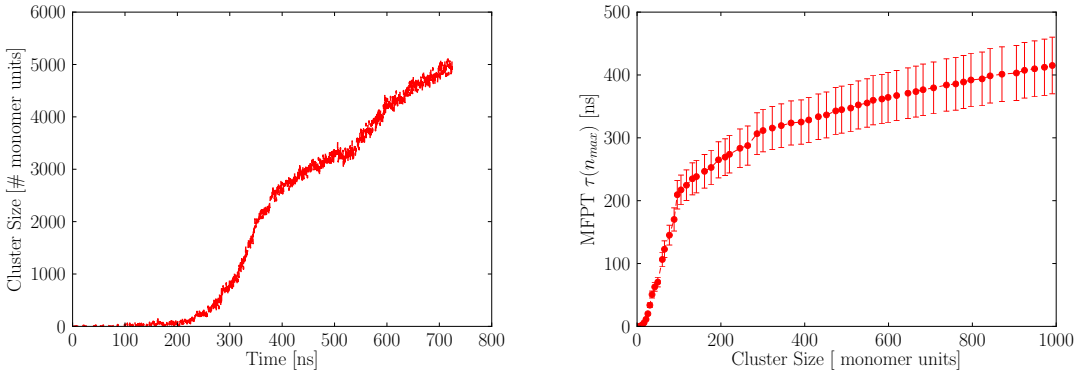

(A) (B)

FIGURE 5.4: Time evolution of the largest cluster size. Left: the evolution of the largest cluster size from a single trajectory. Right: the mean first passage time for the largest cluster size at 280 K averaged over 20 independent trajectories.

In Fig. 5.5 we show the relative variations of these quantities with respect to the values they had at $-100\Delta t$, where $\Delta t = 100000\tau$. When we advance from the supercooled melt towards the formation of the critical nucleus at t_0, we observe first an increase in the global orientational order S_2, then an increase in the radius of gyration of the segments and in the local density, and finally the crystal structure is formed. Due to the persistence length of the molecules, *chain segments* are sufficiently prolate to undergo an ordering transition similar to the isotropic-nematic transition in liquid crystals. Only once they have formed an oriented aggregate, they start straightening. This observation is similar to recent results of Luo and Sommer [48]. To test the Olmsted's [26] proposed nucleation mechanism based on spinodal decomposition. We divided the whole system into two types of monomers, those which participate in the critical nucleus at time t_0 and those which do not. We computed the average monomer volume at time $t = t_{-30}$ and before for these two types of monomers. We found that the average monomer volume for both type of monomers to be the same ($0.408567\sigma^3$) and it is also evident from Fig. 5.5 that the Voronoi volume per particle in the nucleus does not deviate from its melt value until the very late stages of the nucleation process.

The *chain segments* which form the critical nucleus at time t_0 are partially orientated at the time $t = t_{-30}$,(fig. 5.5). We confirm that this is not spinodal assisted decomposition and one reason for this could be that the temperature at which we

simulated is above the spinodal temperature. The Doi theory [24, 25] states that crystallization process proceeds by an increase in persistence length, followed by alignment of these chains. Our results stand in contrast to Olmsted [26] and Doi et.al [24, 25] proposed mechanisms for primary nucleation in polymers, because according to our observations the nucleation mechanism proceeds by aligning of the chain segments, followed by straightening and compaction and then formation of hexagonally packed structure of *chain segments*. It is interesting to mention that these results are similar to our previous work for short polymer chains [42] provided in Chapter 3 of this thesis. It shows that nucleation is a local event, and that does not depend on the chain length at 280 K and we do not observe any effects of entanglements on the nucleation mechanism at this degree of supercooling. This result might seem to be in contradiction with the work of Luo and Sommer [57] who have recently reported that nucleation preferably takes place in regions with a long entanglement length. However, their simulations have been carried out at lower degrees of undercooling than ours. We have shown results for 30% undercooling, thus the critical nuclei are relatively small compared to the entanglement length. For lower degrees of undercooling and larger critical nuclei, entanglement may come into play.

The positional order of the formation of the critical nucleuswas monitored using *averaged local bond order parameters* (ALBO). For $\bar{q}_6$ we show the evolution of the entire distribution rather than just the average (fig. 5.6), because the average is still dominated by the peak at liquid-like $\bar{q}_6$ at times when there is already a clearly discernible shoulder at crystalline $\bar{q}_6$.

We present snapshots of formation of the critical nucleus in FIG. 5.7 at different times from $t = t_{-100}$ to $t = t_0$. The monomers that form the critical nucleus at time t_0 are highlighted in gray. The red color shows the *chain segments* which participate in the formation of critical nucleus with a single stem while the blue, green and orange colors show those chains which fold back and participate in the formation of the critical nucleus with more than one stem. For the case of folded chains we show complete chains instead of segments so that the fold and tails can be seen. These snapshots show that *chain segments* first align themselves, followed by straightening and packing of these *chain segments* and finally an aligned, hexagonally packed crystal is formed. The visualization of formation of the nucleus is consistent what

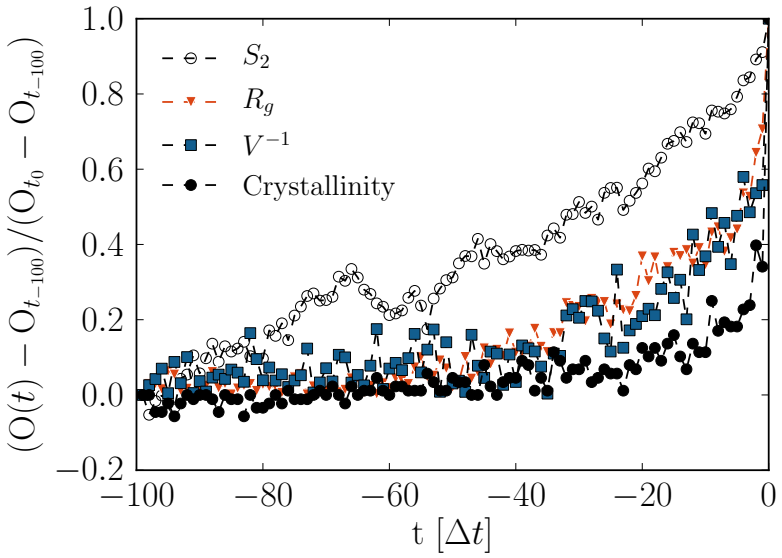

FIGURE 5.5: Relative variation of several observables (O) from the melt to the formation of a critical nucleus for the particles involved in the nucleus: the orientation order parameter S_2 (black, open circle), the radius of gyration R_g (red, triangle), the inverse of the Voronoi cell volume V (blue, square) and the crystallinity order parameter (black, close circle). The curves are averaged over 20 independent trajectories progressing backward in time from the nucleation time $t = t_0$ in steps Δt to $t = -100\Delta t$.

we find from computation of the global alignment S_2 of all *chain segments* that are part of the nucleus at t_0, the average radius of gyration R_g of these *chain segments*, the average volume V of the Voronoi cell associated to each particle that is part of the nucleus, its crystallinity order parameter (fig. 5.5) and the average local bond order parameter $\bar{q}_6$ (fig. 5.6).

The critical nuclei consist of *chain segments* (stems) from different chains and from same chains (folded). We characterize the primary nucleation as a combination of intra-molecular and intermolecular mechanisms. FIG. 5.8 shows that the ratio of the number of stems to the number of chains is always larger than unity which indicates the presence of combination of folded and non-folded chains in the critical nuclei. This is also evident from the snapshots of the critical nucleus in FIG. 5.7. This result agrees with the observations made by Yi et al. [40].

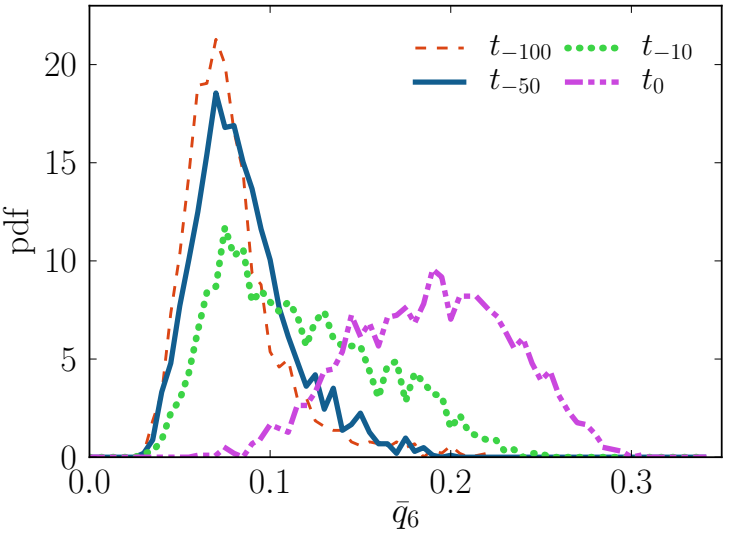

FIGURE 5.6: Probability distributions of the averaged local bond order parameter $\bar{q}_6$ computed at different times for those particles that form the crystallite at t_0.

The shapes of the nuclei play an important role in the mechanical properties of polymeric materials. To observe the evolution of cluster size and shape we calculated the average stem length against cluster size. FIG. 5.9 shows that fitting this data to a power law produces an exponent of 0.32 which is very close to 1/3. This closeness shows that small clusters grows equally in all three directions. This observation is similar to Yi et al. [40].

A number of models have been proposed to study the structure of lamellae. The adjacent re-entry or regular folded and the random re-entry or switchboard models are two main structures and the exact structure is still a controversial issue [137]. To study the structure of lamellae, we chose well developed lamellae and then computed the probability distribution of the inter-stem distances between the ends of the folds. We find that the adjacent re-entry or 'tight' folding is dominant. FIG. 5.10 shows that 58 % of folds are tight folds. This observation is in agreement with Yamamoto and coworkers [43, 46].

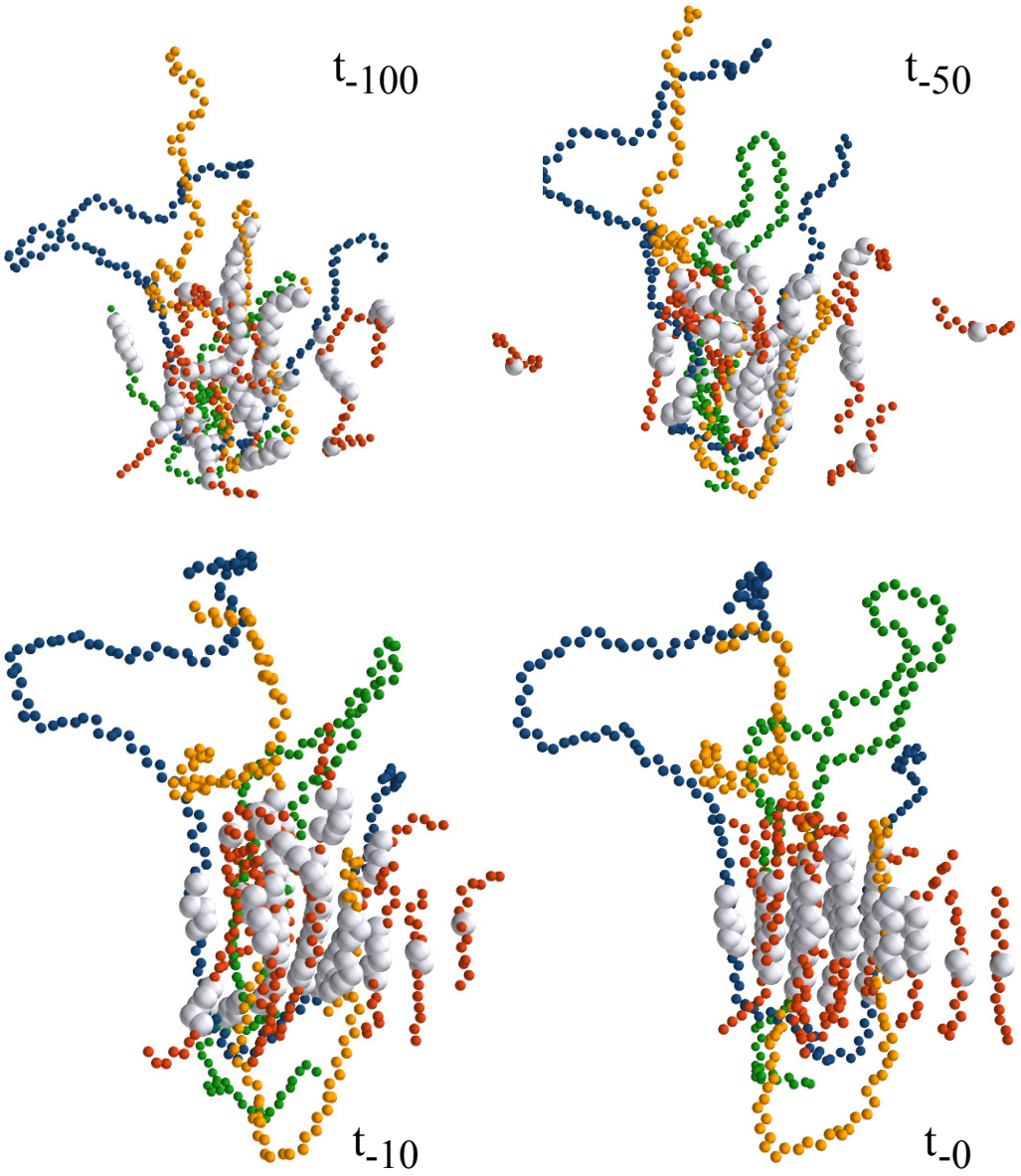

FIGURE 5.7: Snapshots illustrating the nucleation mechanism. Large gray beads: monomers that form the critical nucleus at t_0. Red: segments of chains that participate with a single stem in the formation of the critical nucleus. Blue, green and orange: chains which fold back and participate in the formation of the critical nucleus with more than one stem. For the case of folded chains we show complete chains instead of segments so that folds and tails can be identified.

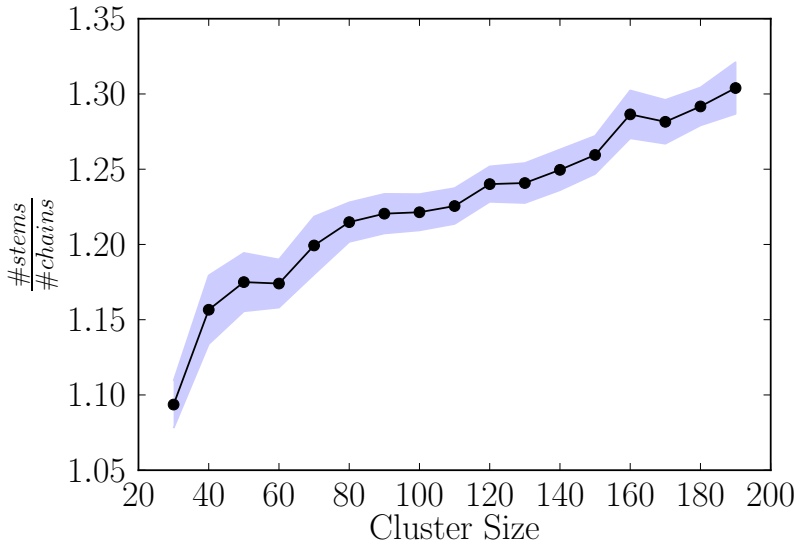

FIGURE 5.8: Ratio of number of stems to number of chains participating in the cluster against cluster size. The black curve with circle symbols shows the mean value and the light blue envelope around this mean value shows the standard deviation.

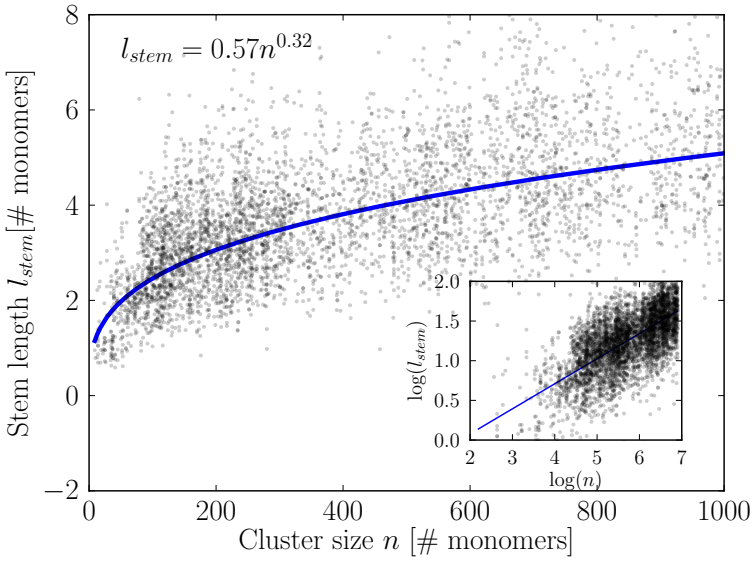

FIGURE 5.9: Stem length against cluster size. In the main figure, a black dot shows a simulation data point, the blue curve shows the mean value. In the inset the same thing is shown on log – log scale.

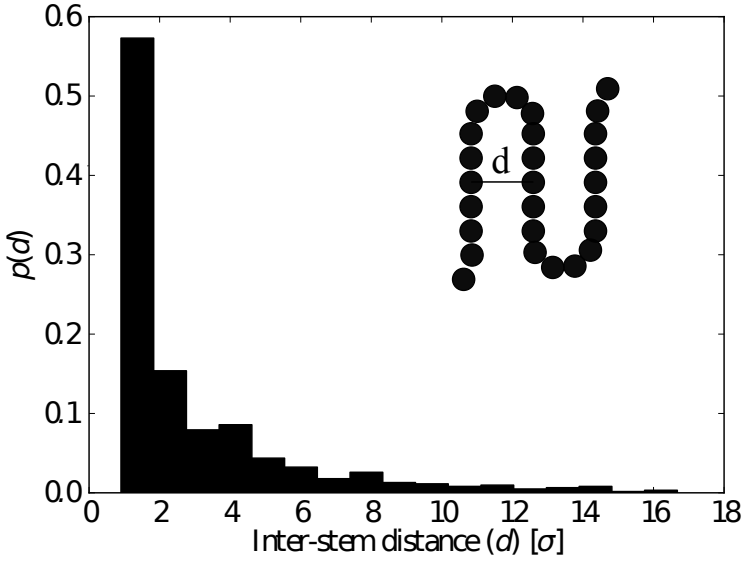

FIGURE 5.10: The probability distribution of the inter-stem distance between the ends of the folds of the chains is shown. A schematics of the inter-stem distance in the folded crystal structure is shown in the inset.

5.4 C150 under shear flow

5.4.1 Simulation details

We have carried out molecular dynamics simulations of n-pentacontahectane (C150) under shear flow. The system consists of 100 chains of C150, we equilibrated the system at 500 K which is well above the melting temperature of C150. The equilibrium melting temperature of n-pentacontahectane (C150) has been reported as 396.4 K by Yi et al. [40]. We chose the density of metastable melt n-pentacontahectane (C150) 0.89 g/cm^3. We performed all molecular dynamics simulations under constant volume and constant temperature conditions. To study the effects of flow on the crystallization, we quenched these configurations from 500 K to 280 K and applied a shear rate $\dot{\gamma}$ to observe the nucleation event. We ran simulations at four different shear rates ranging from $0.0001\tau^{-1}$ to $0.005\tau^{-1}$ ($1.012 \times 10^8 sec^{-1}$ to $5.06 \times 10^9 sec^{-1}$).

We used the DPD thermostat [127], and the friction coefficient γ used for the thermostat was $1.0\tau^{-1}$; where τ is the MD simulation time step.

5.4.2 Results & discussion

In order to monitor the effects of shear rate on the nucleation rate we computed the induction time at different shear rates and show this in FIG. 5.11. There is a critical shear rate above which flow has an effect on the induction time, and this critical shear rate can be estimated by the intersection of the line (continuous blue line) drawn by fitting the induction time data at higher shear rate and a line (dashed blue line) showing the induction time under quiescent conditions ($\dot{\gamma} = 0$). Thus all results are qualitatively the same as those for C20 presented in Chapter 4. Quantitatively, however, there is a difference: if we take the time the center of mass of a chain needs to diffuse across its radius of gyration to estimate the Weissenberg number at the critical shear rate, we obtain $\tau_{\max}\dot{\gamma}_c = 0.41$ which is close to 1.

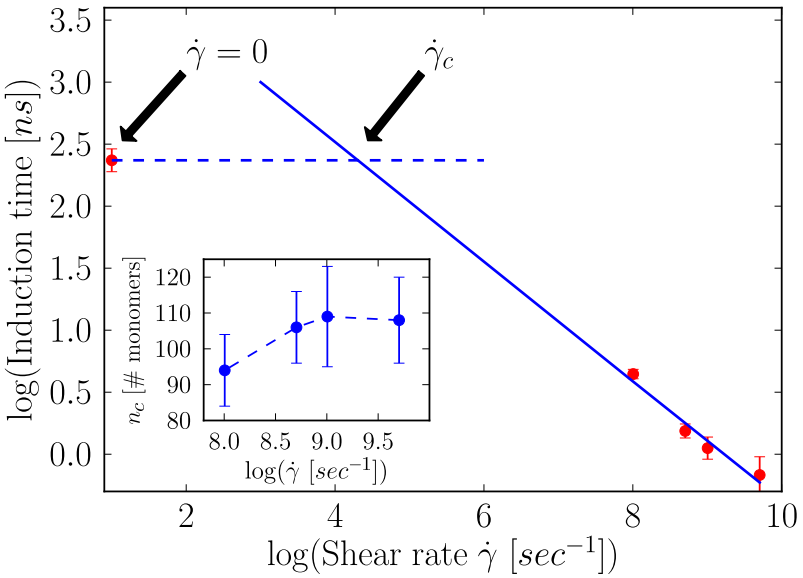

FIGURE 5.11: Induction time against shear rate. In the main figure log-log of induction time vs shear rate is shown, the circle symbols in red color represent the simulation data points and the blue curve shows the fitting line. In the inset, critical nucleus size against log of shear rate is shown.

We compute the longest relaxation time $\tau_{\max}$ as the time the center of mass of a chain needs to diffuse across its radius of gyration. The mean square displacement msd of the chain center of mass is given as:

$$msd(t) = \frac{1}{M} \left\langle |\mathbf{r}_{cm}(t) - \mathbf{r}_{cm}(0)|^2 \right\rangle \tag{5.1}$$

Where $\mathbf{M}$ is number of chains in the melt, $\mathbf{r}_{cm}(t)$ is the position of center of mass of chain at time t and $\mathbf{r}_{cm}(t)$ is the position of center of mass of chain at time 0. The self diffusion constant D for a chain in polymer melt can be computed using the Einstein relation.

$$D = \lim_{t\to\infty} \frac{1}{6t} msd(t) \tag{5.2}$$

In FIG. 5.12, we show mean square displacement of the center of mass of polymer chains as a function of time of C150 at 280 K. Blue circles shows data from the

simulations and the red line shows a fit. The longest relaxation time $\tau_{\max} = 2.2 \times 10^9 \tau$.

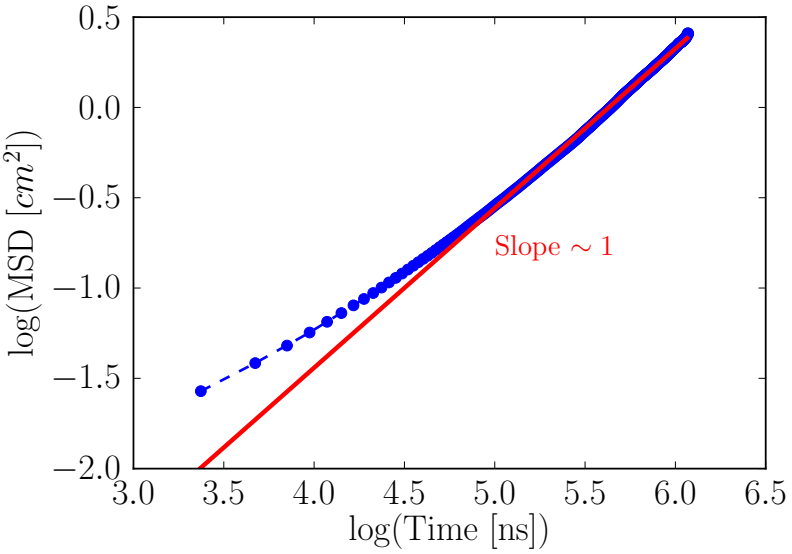

FIGURE 5.12: Mean square displacement of center of mass of polymer chains as a function of time of C150 at 280 K. Blue circles show data from the simulations and the red line shows a fit.

The slope of the continuous blue line is computed to be 0.4784, while for eicosane at 250 K, the slope was 0.5363. This shows that the slope for C20 is steeper than C150. Another interesting thing to note is that the critical shear rate for C150 (10^4 sec^{-1}) is smaller when compared with C20 (10^8 sec^{-1}). One reason for this could be the different degree of supercoolings for these system, this observation is similar to the experimental observations [19, 128].

In the inset of FIG. 5.11, the critical nucleus size against different shear rate is shown, which is practically unchanged. In a single component glass forming system Mokshin et al. [99] observed that at low shear rates the critical nucleus size remains unchanged, but at higher shear rates the nucleus shape become prolate and the size of the nucleus increases with increase in shear rate. In our case the nucleus is already of a cylindrical shape so its size does not increase with shear rate.

To study the nucleation mechanism we analyzed 10 independent trajectories for every shear rate in terms of the average radius of gyration R_g of all *chain segments*

that were part of the nucleus at t_0, the global alignment S_2 of these *chain segments*, the average volume V of the Voronoi [119] cell associated to each particle to be part of the nucleus, its crystallinity order parameter and the average local bond order parameter $\bar{q}_6$.

In Fig. 5.13 we show the relative variations of these quantities with respect to the values they had at $-300\Delta t$, $-140\Delta t$, $-70\Delta t$ and $-20\Delta t$ at shear rates $\dot{\gamma} = 0.0001\tau^{-1}(1.012 \times 10^8 sec^{-1})$, $\dot{\gamma} = 0.0005\tau^{-1}(5.06 \times 10^8 sec^{-1})$, $\dot{\gamma} = 0.001\tau^{-1}(1.012 \times 10^9 sec^{-1})$ and $\dot{\gamma} = 0.005\tau^{-1}(5.06 \times 10^{10} sec^{-1})$ respectively.

Approaching the formation of the critical nucleus at t_0, at different shear rates we observe first an increase in the global nematic order S_2, then an increase in the radius of gyration and in the local density, and finally local positional order is established. When we compare these results with our previous results for short chain alkanes [42] under quiescent conditions and long chain alkanes under quiescent conditions (Fig. 5.5), we find that the nucleation mechanism is initiated by the global alignment of the chains under quiescent and under shearing conditions for C150. For short chain alkanes (C20) under shear conditions, we observe an increase in the global nematic order S_2 and an increase in the radius of gyration R_g simultaneously which is different from long chain alkanes (C150) under shear conditions.

To monitor the crystal order in terms of particle positions rather than segment alignment we computed *averaged local bond order parameters* (ALBO). For $\bar{q}_6$ we show the evolution of the entire distribution rather than just the average (fig. 5.14), because the average is still dominated by the peak at liquid-like $\bar{q}_6$ at times when there is already a clearly discernible shoulder at crystalline $\bar{q}_6$.

When shearing is imposed on the polymeric systems, the chains are straightened on the local level and are oriented in the direction of flow by the shear flow. In Fig. 5.15, we draw the tilt angle of the critical nucleus at different shear rates. This tilt angle is reduced with increasing shear rate. This observation is qualitatively similar to what we have shown for C20 in Chapter 4 and it is also in agreement with simulation studies of polymers[130, 131].

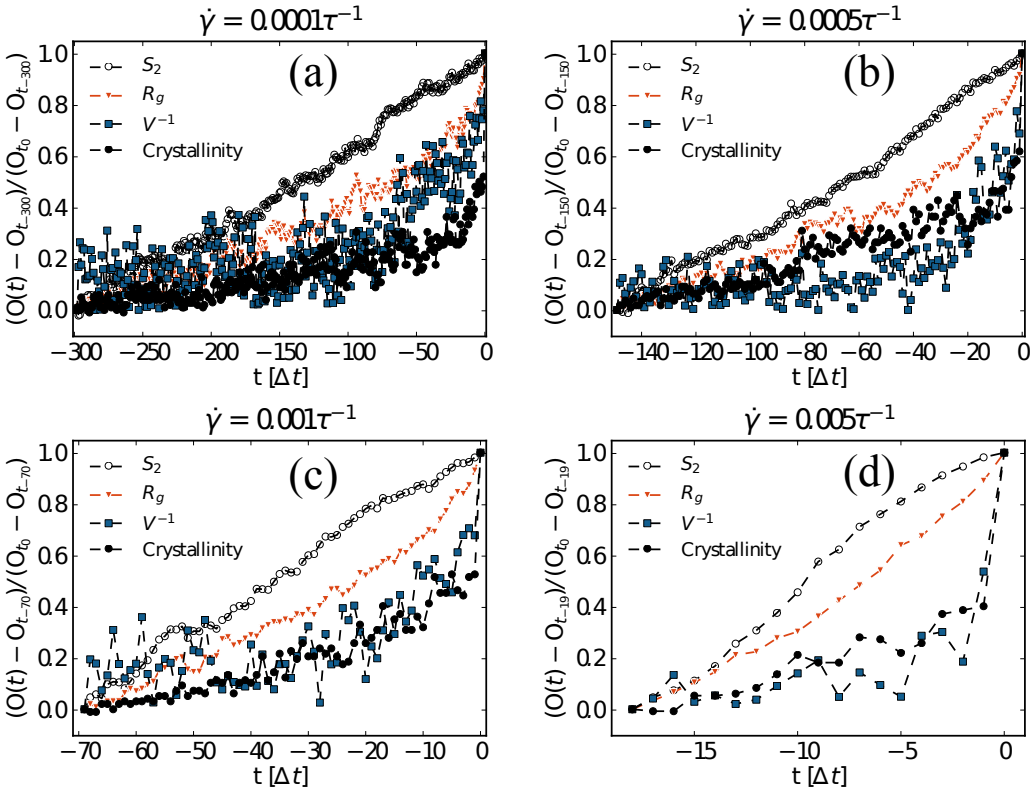

FIGURE 5.13: Relative variation of several observables (O) from the melt to the formation of a critical nucleus for the particles involved in the nucleus: the orientation order parameter S_2 (black, open circle), the inverse of the Voronoi cell volume V (blue, square) and the crystallinity order parameter (black, close circle). (a) : $\dot{\gamma} = 0.0001\tau^{-1}$, (b) : $\dot{\gamma} = 0.0005\tau^{-1}$, (c) : $\dot{\gamma} = 0.001\tau^{-1}$, (d) : $\dot{\gamma} = 0.005\tau^{-1}$. The curves are averaged over 10 independent trajectories progressing backward in time from the nucleation time $t = t_0$ in steps Δt to $t = -300\Delta t$, $t = -140\Delta t$, $t = -70\Delta t$ and $t = -20\Delta t$ at $\dot{\gamma} = 0.0001\tau^{-1}$,$\dot{\gamma} = 0.0005\tau^{-1}$, $\dot{\gamma} = 0.001\tau^{-1}$ and $\dot{\gamma} = 0.005\tau^{-1}$ respectively.

5.4.3 Shear viscosity

We have shown that the flow field has an effect on the nucleation rate. In turn, the presence of the nucleus should also have an effect on the flow field, because the mechanical properties of a crystal differ considerably from those of the melt. In FIG. 5.16 we show the shear viscosity (measured using the instantaneous system average of the stress tensor) as a function of cluster size for a system consisting of 100 chains of C150, at 280K and at a shear rate of $0.001\tau^{-1}$. The simulation data points are subject to strong fluctuations due to the small system size. We do not observe any change in the viscosity during the formation of the nucleus and growth up to

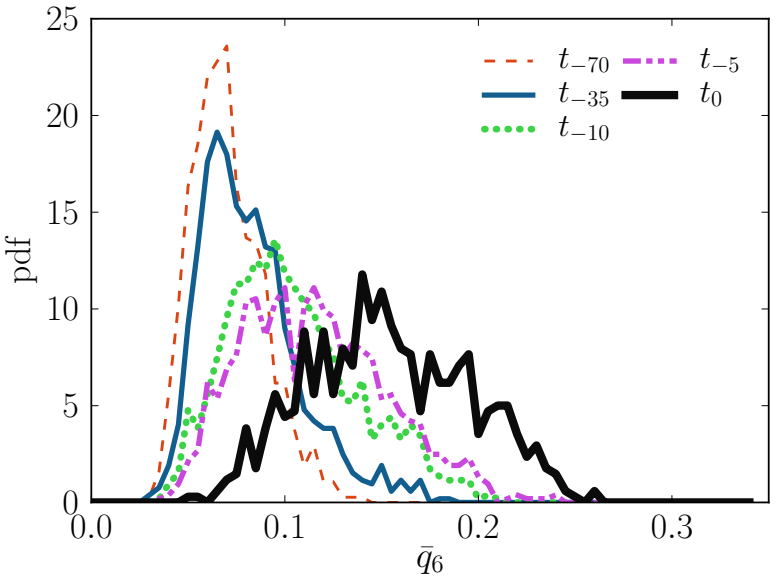

FIGURE 5.14: Probability distributions of the averaged local bond order parameter $\bar{q}_6$ computed at different times for those particles that form the crystallite at t_0.

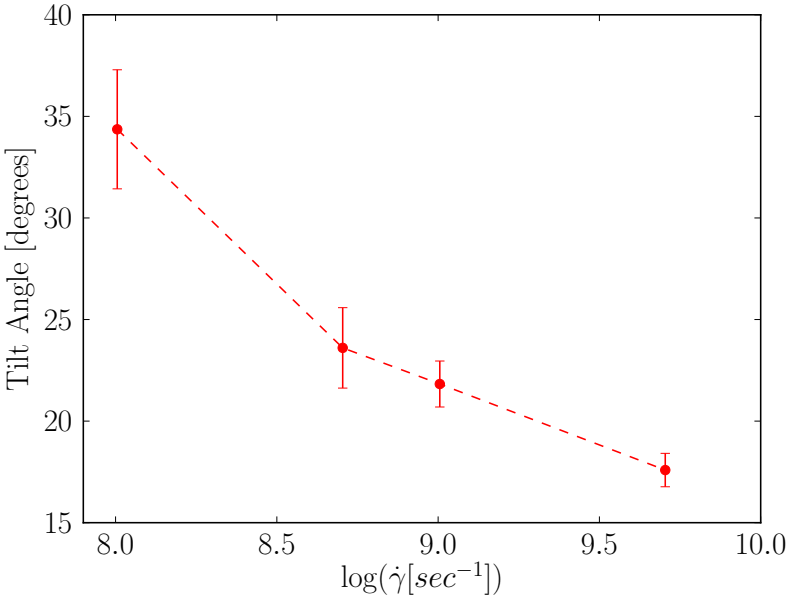

FIGURE 5.15: Tilt angle against shear rate $\dot{\gamma}$.

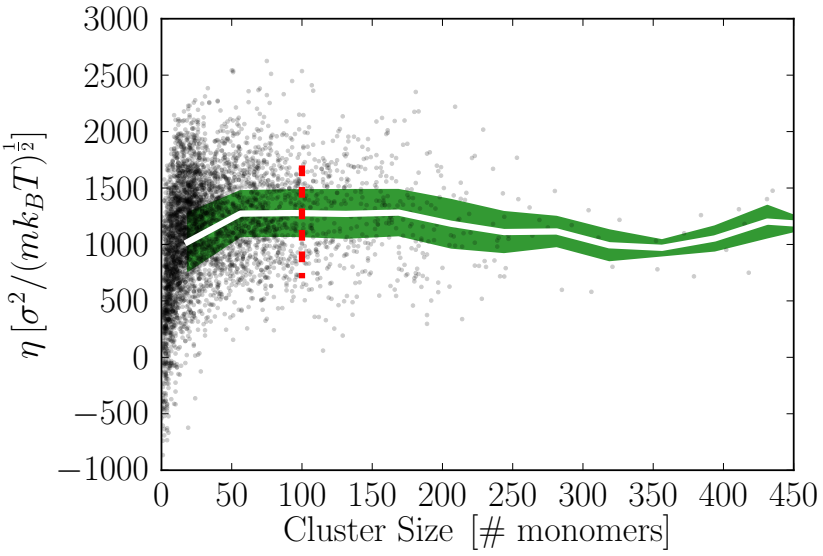

FIGURE 5.16: C20: Shear viscosity as a function of cluster size. Simulation data points (black dots), size of the critical nucleus (red dashed line), mean value of the viscosity (white line) and its standard deviation (green envelope).

a cluster size of 450 monomers. Above this cluster size the scalar pressure started to decrease, because the phase transition was simulated in the NVT ensemble. We conclude that the nucleation events do not have a significant effect on the flow field, as the nuclei are small for the temperatures that we discuss here.

5.5 Crystallization of polyethylene (C500)

5.5.1 Simulation details

We performed molecular dynamics simulations of a system consisting of 200 chains of polyethylene (C500) under quiescent conditions. We equilibrated the system at 500 K for 30 ns which is well above the melting temperature of polyethylene. We chose the density of the metastable melt polyethylene (C500) as 0.89 g/cm^3. We performed all molecular dynamics simulations under constant volume and constant temperature conditions. We used an integration time step of 0.006τ, where $\tau = \sqrt{\frac{k_bT}{m\sigma^2}}$. Where m is mass of bead, k_B is Boltzmann's constant, T is temperature in Kelvin and σ is size of bead.

After running the simulations at 500 K for 30 ns, we quenched the system to 280K to see the nucleation event and then growth. We used the DPD thermostat [127] and the friction coefficient γ used for the thermostat was $1.0\tau^{-1}$; where τ is the MD simulation time step.

5.5.2 Results & discussion

We used the crystallinity order parameter to compute the cluster sizes of different clusters forming in the system, and we show the growth of the six largest clusters in the system in FIG. 5.17. There are large fluctuations in cluster sizes due to attachment and detachment of part of clusters from one cluster to the other cluster.

In FIG. 5.18, we show the degree of crystallinity in the system. We define degree of crystallinity as the ratio of the number of crystalline particles to the total number of particle in the system. The gray monomers belong to the largest cluster in the system. We reach 24% degree of crystallinity after running the simulations for 600 ns. It is however, not clear yet, if this degree of crystallinity can reach 100% or not. In other words, it is not clear that the semi-crystallinity is a kinetic manifestation or a thermodynamically stable state representing the global free energy minimum [68].

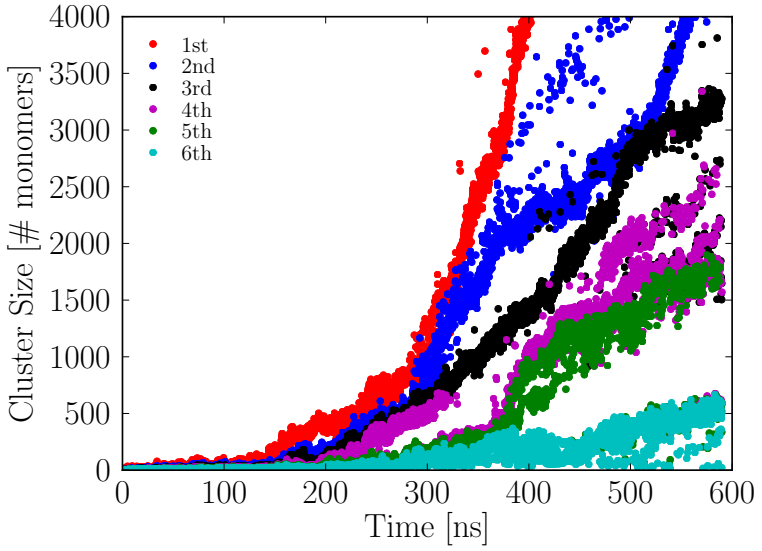

FIGURE 5.17: Growth of six largest clusters in the system at 280k. Different colors show growth of different clusters.

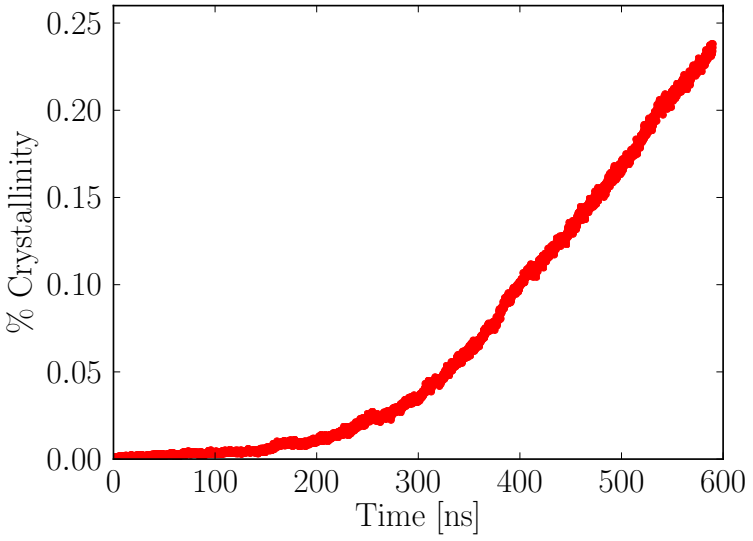

FIGURE 5.18: Degree of crystallinity in the system at 280K.

In FIG. 5.19, we show a snapshot of a complete system consisting of 200 chains of C500. Small red monomers show the amorphous region and all other colors show crystalline regions. This snapshot represents the semicrystalline nature of the

polyethylene.

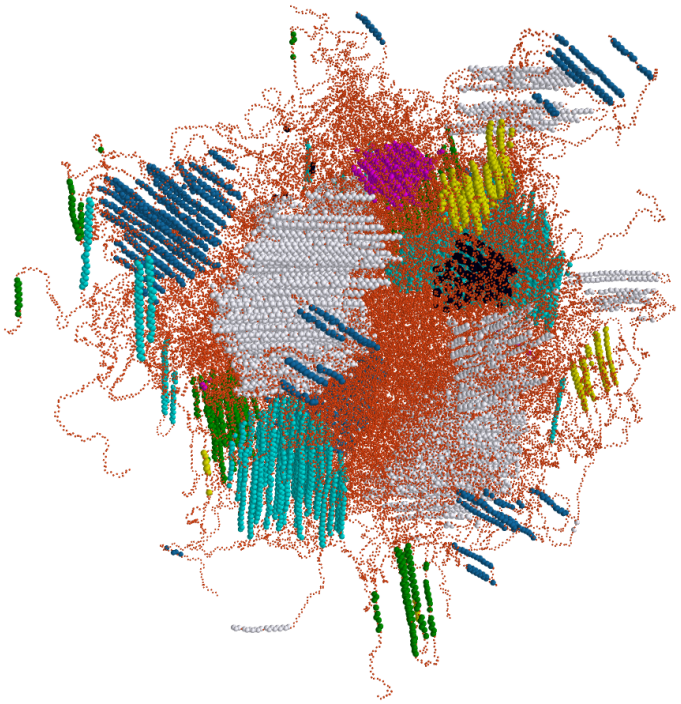

FIGURE 5.19: Snapshot of the complete system showing different clusters with different colors.

In FIG. 5.20, we show the time evolution of a single chain making the transition from a coil to a folded crystal structure. In first three snapshot at t=0 ns, t=11.8 ns and t=29.5 ns, the configuration of the chain is like a coil. At t=59 ns, a few segments of the chain become aligned with each other, at t=117.9 ns small stems are formed and after this step, the length of these stems increases (lamellae thickening). This thickening occurs by the sliding in motion of the chain segment from the amorphous to the crystal region. This folded lamellar crystal structure is a non-equilibrium structure which continues to thicken. Thickness of lamellar is selected kinetically which means if enough time is given to the thickening process, we will get extended crystal structures at the end [4].

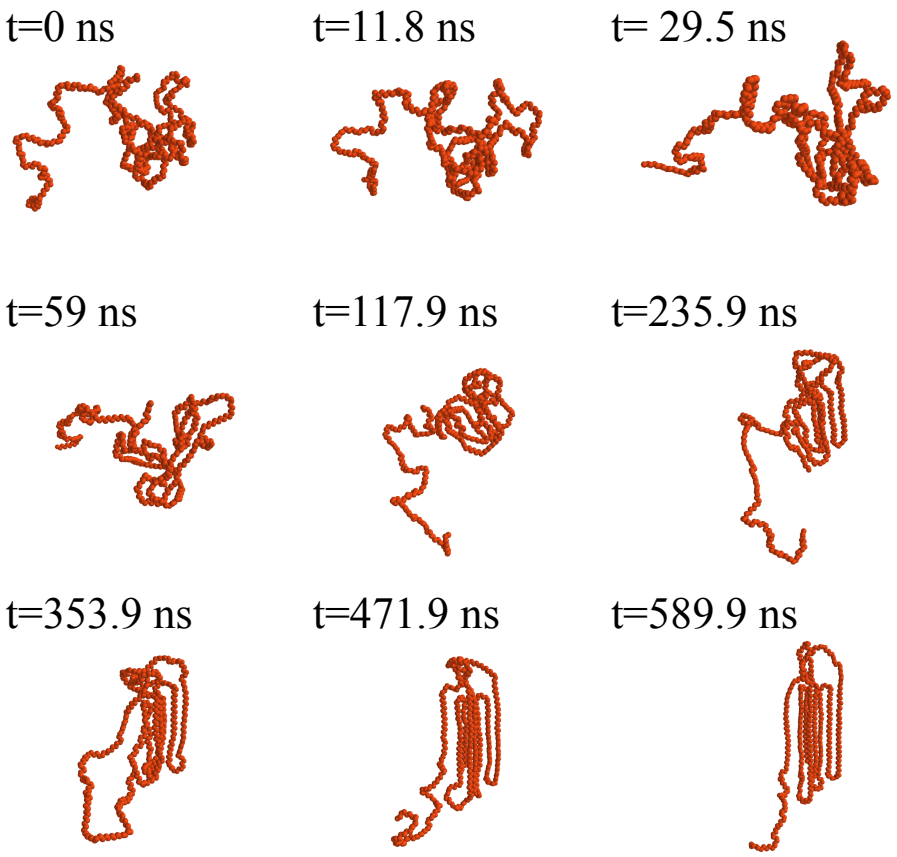

FIGURE 5.20: Time evolution of a single chain showing the transition from coil to folded crystal structures.

5.6 Conclusions

We have analyzed the formation of the critical nucleus from a supercooled melt of C150 under quiescent and shear conditions. We have determined the critical nucleus size using the mean first passage time (FIG. 5.4b). Under quiescent conditions the *chain segments* that form the critical nucleus first align, followed by straightening and compaction, and finally a hexagonally packed structure is formed (FIG. 5.5). We also find that the critical nucleus is formed by the combination of stems that belong to the same chain (folded) and from different chains (every stem from a different chain) (FIG. 5.8). The cluster grows equally in all three directions for small cluster sizes (FIG. 5.9). The tight folding (adjacent re-entry model) in the crystal structure is found to be the dominant lamellae structure rather than random re-entry (FIG. 5.10). Under shear conditions, we estimate the critical shear rates and find a power law relationship between the nucleation and shear rates in agreement with experiments and theory [19]. Under shear conditions, the nucleation mechanism is the same as under quiescent conditions. We compute the response of the system to the formation of nuclei in terms of shear viscosity and do not observe any change in shear viscosity during the formation of the nuclei. Finally, we show the degree of crystallinity, growth of clusters in the system and the transition of a chain from coil configuration to folded crystal structure for C500.

Chapter 6

Conclusions

In this work, we have studied the crystallization mechanism of short polymer chains. The main purpose of the work is to present the effects of flow and temperature on the nucleation time and then to identify the microscopic mechanisms of crystal nucleation and growth under quiescent conditions and under shear flow. We have performed molecular dynamics simulations using a realistic united atom model. As a first step, we have reproduced physical quantities related to phase transitions (i.e. melting point) to test the model and to compare these results with available published results.

In our first study, we have addressed the crystallization of n-eicosane (C20). We have presented crystal nucleation and growth mechanism in C20 under quiescent conditions. We have determined the critical nucleus size and induction times using committor analysis. We have observed that the critical nucleus is of cylindrical shape. For the nucleation mechanism, we have found that the chains which formed the critical nucleus first align, then straighten before densification occurs and the local orientational and positional orders are established. The growth mechanism proceeds through a *sliding in* motion of the chains and attachment of these chains occurs in a cooperative manner.

In our second project, we have studied the effects of flow and and temperature on the induction time and on the nucleation mechanism of C20. We have reported the effects of flow and temperature on the nucleation rates and find that they are

in qualitative agreement with experiment and theory. We have also computed the Weissenberg number at critical shear rate and find it to be 0.6, which is very close to unity. For the nucleation mechanism, at lower shear rates, we have observed the same nucleation mechanism as we observed for C20 under quiescent conditions. At higher shear rates we have found that the chains which form the critical nucleus align and straighten at the same time. We also found that the shear viscosity of the system does not change during the formation of small nuclei.

In our third project, we addressed the crystallization in n-pentacontahectane (C150) under quiescent and under flow conditions. Under quiescent condition, we have observed the same nucleation mechanism as for C20 under quiescent conditions. Under flow conditions, we find similar effects of flow on the induction time as for C20 and find the Weissenberg number equal to 0.41, which is again of order of unity. We do not see any significant difference in the nucleation mechanism under quiescent and under flow conditions for C150. Again, we found that shear viscosity of the system does not change during the formation of small nuclei. We also presented some results for the crystallization of polyethylene (C500) and showed that the degree of crystallinity reaches 24%. At the end, we showed the transition of a single chain from a coil to a folded crystal structure.

Still there are many questions which should be addressed to give a comprehensive understanding of polymer crystallization. In future the microscopic mechanism of attachment of long chains needs to be addressed and a theory which can explain this process should come out. The factors which determine the thickness of lamellae need to be deduced. Attention should be paid to the regions between purely crystal and purely amorphous regions. The effects of entanglements on the crystallization as a function of degree of supercooling should be addressed. The crystal structures formed under shear flow and elongational flow should be compared.

We think this work should be a positive contribution towards the understanding of polymer crystallization and will in particular open a door to address this question in a different way by using now the different order parameters which have been shown to be of importance.

Bibliography

[1] Michael Kotelyanskii and Doros N. Theodorou. *Simulation Methods for Polymer*. Marcel Dekker, 2004.

[2] Michael Rubinstein and Ralph H. Colby. *Polymer Physics*. Oxford university Press, 2003.

[3] A. Jabbarzadeh and R. I. Tanner. Crystallization of alkanes under quiescent and shearing conditions. *Journal of Non-Newtonian Fluid Mechanics*, 160 (1):11–21, 2009.

[4] M. Muthukumar. *Nucleation in Polymer Crystallization*, pages 1–63. John Wiley & Sons, Inc., 2004.

[5] M. Imai, K. Kaji, and T. Kanaya. Structural formation of poly(ethylene terephthalate) during the induction period of crystallization. 3. evolution of density fluctuations to lamellar crystal. *Macromolecules*, 27(24):7103–7108, 1994.

[6] M. Imai, K. Kaji, T. Kanaya, and Y. Sakai. Ordering process in the induction period of crystallization of poly(ethylene terephthalate). *Physical Review B*, 52:12696–12704, 1995.

[7] T. A. Ezquerra, E. López-Cabarcos, B. S. Hsiao, and F. J. Baltà-Calleja. Precursors of crystallization via density fluctuations in stiff-chain polymers. *Physical Review E*, 54:989–992, Jul 1996.

[8] A. Keller, M. Hikosaka, S. Rastogi, A. Toda, P.J. Barham, and G. Goldbeck-Wood. An approach to the formation and growth of new phases with application to polymer crystallization: effect of finite size,

metastability, and Ostwald's rule of stages. *Journal of Materials Science*, 29 (10):2579–2604, 1994.

[9] M. Imai, K. Mori, T. Mizukami, K. Kaji, and T. Kanaya. Structural formation of poly(ethylene terephthalate) during the induction period of crystallization:1. ordered structure appearing before crystal nucleation. *Polymer*, 33:4451, 1992.

[10] G. Strobl. From the melt via mesomorphic and granular crystalline layers to lamellar crystallites: A major route followed in polymer crystallization? *The European Physical Journal E*, 3(2):165–183, 2000.

[11] G. Strobl. A thermodynamic multiphase scheme treating polymer crystallization and melting. *The European Physical Journal E*, 18(3): 295–309, 2005.

[12] G. Strobl. Crystallization and melting of bulk polymers: New observations, conclusions and a thermodynamic scheme. *Progress in Polymer Science*, 31: 398–442, 2006.

[13] G. Strobl and T. Y. Cho. Growth kinetics of polymer crystals in bulk. *The European Physical Journal E*, 23:55, 2007.

[14] G. Strobl. *Colloquium*: Laws controlling crystallization and melting in bulk polymers. *Reviews of Modern Physics*, 81:1287–1300, Sep 2009.

[15] R. H. Somani, L. Yang, I. Sics, B. S. Hsiao, N. V. Pogodina, H. H. Winter, P. Agarwal, H. Fruitwala, and A. Tsou. Orientation-induced crystallization in isotactic polypropylene melt by shear deformation. *Macromolecular Symposia*, 185(1):105–117, 2002.

[16] Rajesh H. Somani, Ling Yang, and Benjamin S. Hsiao. Precursors of primary nucleation induced by flow in isotactic polypropylene. *Physica A: Statistical Mechanics and its Applications*, 304(1–2):145 – 157, 2002. Scattering Studies of Mesoscopic Scale Structure and Dynamics in Soft Matter.

[17] Ferass M. Abuzaina, Benjamin D. Fitz, Saša Andjelić, and Dennis D. Jamiolkowski. Time resolved study of shear-induced crystallization of

poly(p-dioxanone) polymers under low-shear, nucleation-enhancing shear conditions by small angle light scattering and optical microscopy. *Polymer*, 43(17):4699 – 4708, 2002.

[18] D. Lellinger, G. Floudas, and I. Alig. Shear induced crystallization in poly(ϵ-caprolactone): effect of shear rate. *Polymer*, 44(19):5759 – 5769, 2003.

[19] Salvatore Coppola, Luigi Balzano, Emilia Gioffredi, Pier Luca Maffettone, and Nino Grizzuti. Effects of the degree of undercooling on flow induced crystallization in polymer melts. *Polymer*, 45(10):3249 – 3256, 2004.

[20] Aadil Elmoumni and H. Henning Winter. Large strain requirements for shear-induced crystallization of isotactic polypropylene. *Rheologica Acta*, 45 (6):793–801, 2006.

[21] S. Acierno and N. Grizzuti. Flow-induced crystallization of polymer: theory and experiments. *International Journal of Material Forming*, 1(1):583–586, 2008.

[22] Ri-Chao Zhang, Ai Lu, and Zhong-Bin Xu. Effect of molecular weight on crystallization of semirigid poly(phenylene sulfide) under shear flow. *Journal of Applied Polymer Science*, 124(2):1562–1569, 2012.

[23] John W. Cahn and John E. Hilliard. Free energy of a nonuniform system. i. interfacial free energy. *The Journal of Chemical Physics*, 28(2):258–267, 1958.

[24] M. Doi and S. F. Edwards. *The Theory of Polymer Dynamics*. Oxford University Press, 1986.

[25] Takayuki Shimada, Masao Doi, and Koji Okano. Concentration fluctuation of stiff polymers. iii. spinodal decomposition. *The Journal of Chemical Physics*, 88(11):7181–7186, 1988.

[26] P. D. Olmsted, W. C. K. Poon, T. C. B. McLeish, N. J.Terrill, and A. J. Ryan. Spinodal-assisted crystallization in polymer melts. *Physical Review Letters*, 81:373–376, 1998.

[27] K. Kaji. *Handbook of Thermoplastic Polyesters: Homopolymers, Copolymers, Blends, and Composites*, chapter Structure Formation in PET during the Induction Period of Crystallization, pages 225–251. Wiley-VCH Verlag GmbH, 2002.

[28] Davis G. Thomas, Hoffman John D., and John I. Lauritzen Jr. *Treatise on Solid State Chemistry:Vol,3,Crystalline and Noncrystalline Solids*, chapter The Rate of Crystallization of Linear Polymers With Chain Folding, pages 497–614. N. B. Hannay (ed.), Plenum Press, New York, 1976.

[29] D. M. Sadler and G. H. Gilmer. A model for chain folding in polymer crystals: rough growth faces are consistent with the observed growth rates. *Polymer*, 25:1446–1453, 1984.

[30] Richard S. Graham, Alexei E. Likhtman, Tom C. B. McLeish, and Scott T. Milner. Microscopic theory of linear, entangled polymer chains under rapid deformation including chain stretch and convective constraint release. *Journal of Rheology (1978-present)*, 47(5):1171–1200, 2003.

[31] Richard S. Graham and Peter D. Olmsted. Coarse-grained simulations of flow-induced nucleation in semicrystalline polymers. *Physical Review Letters*, 103:115702, Sep 2009.

[32] Richard S. Graham and Peter D. Olmsted. Kinetic monte carlo simulations of flow-induced nucleation in polymer melts. *Faraday discussions*, 144:71–92, 2010.

[33] Kenny Jolley and Richard S. Graham. A fast algorithm for simulating flow-induced nucleation in polymers. *The Journal of Chemical Physics*, 134 (16):164901, 2011.

[34] K. Esselink, P. A. J. Hilbers, and B. W. H. van Beest. Molecular dynamics study of nucleation and melting of n-alkanes. *The Journal of Chemical Physics*, 101(10):9033–9041, 1994.

[35] Hisao Takeuchi. Structure formation during the crystallization induction period of a short chain-molecule system: A molecular dynamics study. *The Journal of Chemical Physics*, 109(13):5614–5621, 1998.

[36] Susumu Fujiwara and Tetsuya Sato. Molecular dynamics simulation of structural formation of short polymer chains. *Physical Review Letters*, 80: 991–994, Feb 1998.

[37] Susumu Fujiwara and Tetsuya Sato. Molecular dynamics simulation of structure formation of short chain molecules. *The Journal of Chemical Physics*, 110(19):9757–9764, 1999.

[38] Peng Yi and Gregory C. Rutledge. Molecular simulation of crystal nucleation in n-octane melts. *The Journal of Chemical Physics*, 131:1–12, 2009.

[39] Peng Yi and Gregory C. Rutledge. Molecular simulation of bundle-like crystal nucleation from n-eicosane melts. *The Journal of Chemical Physics*, 135:11, 2011.

[40] Peng Yi, C. Rebecca Locker, and Gregory C. Rutledge. Molecular Dynamics Simulation of Homogeneous Crystal Nucleation in Polyethylene. *Macromolecules*, 46(11):4723–4733, 2013.

[41] Hasan Zerze, Jeetain Mittal, and Anthony J. McHugh. Ab initio crystallization of alkanes: Structure and kinetics of nuclei formation. *Macromolecules*, 46(22):9151–9157, 2013.

[42] Muhammad Anwar, Francesco Turci, and Tanja Schilling. Crystallization mechanism in melts of short n-alkane chains. *The Journal of Chemical Physics*, 139(21):214904, 2013.

[43] Takashi Yamamoto. Molecular dynamics of polymer crystallization revisited: Crystallization from the melt and the glass in longer polyethylene. *The Journal of Chemical Physics*, 139(5):054903, 2013.

[44] Takashi Yamamoto. Molecular dynamics simulations of polymer crystallization in highly supercooled melt: Primary nucleation and cold crystallization. *The Journal of Chemical Physics*, 133(3):034904, 2010.

[45] Takashi Yamamoto. Molecular dynamics simulations of steady-state crystal growth and homogeneous nucleation in polyethylene-like polymer. *The Journal of Chemical Physics*, 129(18):184903, 2008.

[46] Takashi Yamamoto. Molecular dynamics modeling of polymer crystallization from the melt. *Polymer*, 45(4):1357 – 1364, 2004. Modeling of Chain Conformations and Spatial Configurations.

[47] Takashi Yamamoto. Molecular-dynamics simulation of polymer ordering. i. crystallization from vapor phase. *The Journal of Chemical Physics*, 109(11): 4638–4645, 1998.

[48] Chuanfu Luo and Jens-Uwe Sommer. Growth pathway and precursor states in single lamellar crystallization: Md simulations. *Macromolecules*, 44(6): 1523–1529, 2011.

[49] Chuanfu Luo and Jens-Uwe Sommer. Coexistence of melting and growth during heating of a semicrystalline polymer. *Physical Review Letters*, 102: 147801, Apr 2009.

[50] P. Welch and M. Muthukumar. Molecular mechanisms of polymer crystallization from solution. *Physical Review Letters*, 87:218302, Nov 2001.

[51] Hendrik Meyer and Florian Müller-Plathe. Formation of chain-folded structures in supercooled polymer melts. *The Journal of Chemical Physics*, 115(17):7807–7810, 2001.

[52] Jens-Uwe Sommer and Günter Reiter. Polymer crystallization in quasi-two dimensions. ii. kinetic models and computer simulations. *The Journal of Chemical Physics*, 112(9):4384–4393, 2000.

[53] N. Waheed, M. S. Lavine, and G. C. Rutledge. Molecular simulation of crystal growth in n-eicosane. *The Journal of Chemical Physics*, 116(5): 2301–2309, 2002.

[54] M. Muthukumar. *Modeling Polymer Crystallization*, volume 191 of *Advances in Polymer Science*, pages 241–274. Springer Berlin Heidelberg, 2005.

[55] M. Muthukumar. Molecular modeling of nucleation in polymers. *Philosophical Transactions of the Royal Society of London A: Mathematical, Physical and Engineering Sciences*, A361:539–556, 2003.

[56] M. Muthukumar. Commentary on theories of polymer crystallization. *The European Physical Journal E*, 3(2):199–202, 2000.

[57] Chuanfu Luo and Jens-Uwe Sommer. Frozen topology: Entanglements control nucleation and crystallization in polymers. *Physical Review Letters*, 112:195702, May 2014.

[58] Akira Koyama, Takashi Yamamoto, Koji Fukao, and Yoshihisa Miyamoto. Molecular dynamics simulation of polymer crystallization from an oriented amorphous state. *Physical Review E*, 65:050801, May 2002.

[59] Akira Koyama, Takashi Yamamoto, Koji Fukao, and Yoshihisa Miyamoto. Molecular dynamics studies on polymer crystallization from a stretched amorphous state. *Journal of Macromolecular Science, Part B*, 42(3-4): 821–831, 2003.

[60] Marc S. Lavine, Numan Waheed, and Gregory C. Rutledge. Molecular dynamics simulation of orientation and crystallization of polyethylene during uniaxial extension. *Polymer*, 44(5):1771 – 1779, 2003.

[61] Min Jae Ko, Numan Waheed, Marc S. Lavine, and Gregory C. Rutledge. Characterization of polyethylene crystallization from an oriented melt by molecular dynamics simulation. *The Journal of Chemical Physics*, 121(6): 2823–2832, 2004.

[62] T. C. Ionescu, C. Baig, B. J. Edwards, D. J. Keffer, and A. Habenschuss. Structure formation under steady-state isothermal planar elongational flow of n-eicosane: A comparison between simulation and experiment. *Physical Review Letters*, 96:037802, Jan 2006.

[63] I. Dukovski and M. Muthukumar. Langevin dynamics simulations of early stage shish-kebab crystallization of polymers in extensional flow. *The Journal of Chemical Physics*, 118(14):6648–6655, 2003.

[64] Chunggi Baig and Brian J. Edwards. Atomistic simulation of crystallization of a polyethylene melt in steady uniaxial extension. *Journal of Non-Newtonian Fluid Mechanics*, 165(17–18):992 – 1004, 2010. Proceedings

of the 5th International Workshop on Non-Equilibrium Thermodynamics 2009.

[65] C. Baig and B. J. Edwards. Atomistic simulation of flow-induced crystallization at constant temperature. *Europhysics Letters*, 89:36003, 2010.

[66] Günter Reiter and Gert R. Strobl. *Progress in Understanding of Polymer Crystallization, Lect. Notes Phys. 714.* Springer-Verlag Berlin Heidelberg, 2007.

[67] Günter Reiter and Jens-Uwe Sommer. *Polymer Crystallization: Obervations, Concepts and Interpretations.* Springer, Berlin, Heidelberg, 2003.

[68] M. Muthukumar. *Progress in Understanding of Polymer Crystallization*, chapter 1, pages 1–18. Springer-Verlag Berlin Heidelberg, 2007.

[69] Wolfgang Paul, Do Y. Yoon, and Grant D. Smith. An optimized united atom model for simulations of polymethylene melts. *The Journal of Chemical Physics*, 103(4):1702–1709, 1995.

[70] N. Waheed, M.J. Ko, and G.C. Rutledge. Molecular simulation of crystal growth in long alkanes. *Polymer*, 46(20):8689 – 8702, 2005.

[71] H. J. Limbach, A. Arnold, B. A. Mann, and C. Holm. ESPResSo—an extensible simulation package for research on soft matter systems. *Computer Physics Communications*, 174(9):704–727, 2006.

[72] S. Varrette, P. Bouvry, H. Cartiaux, and F. Georgatos. Management of an Academic HPC Cluster: The UL Experience. In *Proc. of the 2014 Intl. Conf. on High Performance Computing & Simulation (HPCS 2014)*, pages 959–967, Bologna, Italy, July 2014. IEEE.

[73] B. J. Alder and T. E. Wainwright. Phase transition for a hard sphere system. *The Journal of Chemical Physics*, 27(5):1208–1209, 1957.

[74] B. J. Alder and T. E. Wainwright. Studies in molecular dynamics. i. general method. *The Journal of Chemical Physics*, 31(2):459–466, 1959.

[75] A. Rahman. Correlations in the motion of atoms in liquid argon. *Physical Review*, 136:A405–A411, Oct 1964.

[76] Frank H. Stillinger and Aneesur Rahman. Improved simulation of liquid water by molecular dynamics. *The Journal of Chemical Physics*, 60(4): 1545–1557, 1974.

[77] Jarošaw Meller. *Molecular Dynamics. eLS.* John Wiley & Sons, Ltd, 2001. ISBN 9780470015902.

[78] Daan Frenkel and Berend Smith. *Understanding Molecular Simulation - From Alogorithms to Applications.* 1996.

[79] Loup Verlet. Computer "experiments" on classical fluids. i. thermodynamical properties of lennard-jones molecules. *Physical Review*, 159:98–103, Jul 1967.

[80] R. W. Hockney. *"The potential calculation and some applications" Methods in Computational Physics.* New York Academic Press, 1970.

[81] William C. Swope, Hans C. Andersen, Peter H. Berens, and Kent R. Wilson. A computer simulation method for the calculation of equilibrium constants for the formation of physical clusters of molecules: Application to small water clusters. *The Journal of Chemical Physics*, 76(1):637–649, 1982.

[82] Philippe H. Hünenberger. Thermostat algorithms for molecular dynamics simulations. *Advances in Polymer Science*, 173(130):105–149, 2005.

[83] E. A. Koopman and C. P. Lowe. Advantages of a lowe-andersen thermostat in molecular dynamics simulations. *The Journal of Chemical Physics*, 124 (20):204103, 2006.

[84] L. V. Woodcock. Isothermal molecular dynamics calculations for liquid salts. *Chemical Physics Letters*, 10(3):257 – 261, 1971.

[85] H. J. C. Berendsen, J. P. M. Postma, W. F. van Gunsteren, A. DiNola, and J. R. Haak. Molecular dynamics with coupling to an external bath. *The Journal of Chemical Physics*, 81(8):3684–3690, 1984.

[86] Hans C. Andersen. Molecular dynamics simulations at constant pressure and/or temperature. *The Journal of Chemical Physics*, 72(4):2384–2393, 1980.

[87] C. P. Lowe. An alternative approach to dissipative particle dynamics. *Europhysics Letters*, 47:145, 1999.

[88] Gary S. Grest and Kurt Kremer. Molecular dynamics simulation for polymers in the presence of a heat bath. *Physical Review A*, 33:3628–3631, May 1986.

[89] P. J. Hoogerbrugge and J. M. V. A. Koelman. Simulating microscopic hydrodynamic phenomena with dissipative particle dynamics. *Europhysics Letters*, 19:155–160, 1992.

[90] Shuichi Nosé. A unified formulation of the constant temperature molecular dynamics methods. *The Journal of Chemical Physics*, 81(1):511–519, 1984.

[91] William G. Hoover. Canonical dynamics: Equilibrium phase-space distributions. *Physical Review A*, 31:1695–1697, Mar 1985.

[92] M. Parrinello and A. Rahman. Polymorphic transitions in single crystals: A new molecular dynamics method. *Journal of Applied Physics*, 52(12): 7182–7190, 1981.

[93] A. Kolb and B. Dünweg. Optimized constant pressure stochastic dynamics. *Journal of Chemical Physics*, 111:4453, 1999.

[94] J. Prost P. G. de Gennes. *The Physics of Liquid Crystals*. Oxford University Press, 1995.

[95] Paul J. Steinhardt, David R. Nelson, and Marco Ronchetti. Bond-orientational order in liquids and glasses. *Physical Review B*, 28(2): 784–805, 1983.

[96] W. Lechner and C. Dellago. Accurate determination of crystal structures based on averaged local bond order parameters. *The Journal of Chemical Physics*, 129:114707, 2008.

[97] Jan Wedekind, Reinhard Strey, and David Reguera. New method to analyze simulations of activated processes. *The Journal of Chemical Physics*, 126 (13):134103, 2007.

[98] Anatolii V. Mokshin and Jean-Louis Barrat. Crystal nucleation and cluster-growth kinetics in a model glass under shear. *Physical Review E*, 82: 021505, Aug 2010.

[99] Anatolii V. Mokshin, Bulat N. Galimzyanov, and Jean-Louis Barrat. Extension of classical nucleation theory for uniformly sheared systems. *Physical Review E*, 87:062307, Jun 2013.

[100] Sarah E. M. Lundrigan and Ivan Saika-Voivod. Test of classical nucleation theory and mean first-passage time formalism on crystallization in the Lennard-Jones liquid. *The Journal of Chemical Physics*, 131(10):104503, 2009.

[101] Joop H. ter Horst and Dimo Kashchiev. Determination of the nucleus size from the growth probability of clusters. *The Journal of Chemical Physics*, 119(4):2241–2246, 2003.

[102] M. Volmer and A. Weber. Keimbildung in übersättigten gebilden (nucleation of supersaturated structures). *ZEITSCHRIFT FUR PHYSIKALISCHE CHEMIE NEUE FOLGE*, 119:277–301, 1926.

[103] Döring W Becker R. Kinetische behandlung der keimbildung in übersättigten gebilden (kinetic theory for nucleation of supersaturated structures). *Annals of Physics*, 24:719–752, 1935.

[104] Jens Lothe and G. M. Pound. Reconsiderations of nucleation theory. *The Journal of Chemical Physics*, 36(8):2080–2085, 1962.

[105] D. Stauffer K. Binder. Statistical theory of nucleation, condensation and coagulation. *Advances of Physics*, 25:343–396, 1976.

[106] Tomáš Němec. The possibility of direct gas-to-solid nucleation m echanism in water vapor. In *Workshop on homogeneous vapor-liquid nucleation in water*, 2008.

[107] Jens-Uwe Sommer. *Progress in Understanding of Polymer Crystallization*, chapter 2, pages 19–47. Springer-Verlag Berlin Heidelberg, 2007.

[108] Wenbing Hu. *Progress in Understanding of Polymer Crystallization*, chapter 3, pages 47–63. Springer-Verlag Berlin Heidelberg, 2007.

[109] Jonathan P. K. Doye and Daan Frenkel. The mechanism of thickness selection in the Sadler-Gilmer model of polymer crystallization. *The Journal of Chemical Physics*, 110:7073–7086, 1999.

[110] M. Muthukumar. *Advances in Chemical Physics*, chapter 1, pages 1–64. JOHN WILEY & SONS, INC, 2003.

[111] Marcus G. Martin and J. Ilja Siepmann. Transferable potentials for phase equilibria. 1. united-atom description of n-alkanes. *The Journal of Physical Chemistry B*, 102 (14):2569–2577, 1998.

[112] David Turnbull and Robert L. Cormia. Kinetics of crystal nucleation in some normal alkane liquids. *The Journal of Chemical Physics*, 34(3): 820–827, 1961.

[113] A. B. Herhold E. B. Sirota. Transient rotator phase induced nucleation in n-alkane melts. *Polymer*, 41:8781–8789, 2000.

[114] H. Kraack, E. B. Sirota, and M. Deutsch. Measurements of homogeneous nucleation in normal-alkanes. *The Journal of Chemical Physics*, 112(15): 6873–6885, 2000.

[115] Bernward A. Mann. *The Swelling Behaviour of Polyelectrolyte Networks*. PhD thesis, Johannes Gutenberg-University, Mainz, Germany, 2005.

[116] Ulf Daniel Schiller. Dissipative particle dynamics - a study of the methodological background. Master's thesis, Condensed Matter Theory Group Faculty of Physics University of Bielefeld, 2005.

[117] W. Paul, Grant D. Smith, and Do Y. Yoon. Static and dynamic properties of a n-c100h202 melt from molecular dynamics simulations. *Macromolecules*, 30(25):7772–7780, 1997.

[118] Toshiaki Miura, Ryoichi Kishi, Masuhiro Mikami, and Yoshikazu Tanabe. Effect of rigidity on the crystallization processes of short polymer melts. *Physical Review E*, 63:061807, May 2001.

[119] Chris H. Rycroft. VORO++: A three-dimensional Voronoi cell library in C++. *Chaos*, 19(4):041111, 2009.

[120] Matthew J. Hamer, Jonathan A. D. Wattis, and Richard S. Graham. Analytic calculation of nucleation rates from a kinetic monte carlo simulation of flow induced crystallization in polymers. *Journal of Non-Newtonian Fluid Mechanics*, 165(19–20):1294 – 1301, 2010.

[121] Richard S. Graham. Molecular modelling of flow-induced crystallisation in polymers. *Journal of Engineering Mathematics*, 71(3):237–251, 2011.

[122] Rajesh H. Somani, Ling Yang, Lei Zhu, and Benjamin S. Hsiaoa. Flow-induced shish-kebab precursor structures in entangled polymer melts. *Polymer*, 46:8587–8623, 2005.

[123] Muhammad Anwar, Joshua T. Berryman, and Tanja Schilling. Crystal nucleation mechanism in melts of short polymer chains under quiescent conditions and under shear flow. *The Journal of Chemical Physics*, 141(12): 124910, 2014.

[124] Florian Muller-Plathe. Reversing the perturbation in nonequilibrium molecular dynamics: An easy way to calculate the shear viscosity of fluids. *Physical Review E*, 59:4894–4898, 1999.

[125] A. W. Lees and S. F. Edwards. The computer study of transport processes under extreme conditions. *Journal of Physics C: Solid State Physics Volume 5 Number 15*, 5, 1972.

[126] A. Chatterjee. Modification to Lees–Edwards periodic boundary condition for dissipative particle dynamics simulation with high dissipation rates. *Molecular Simulation*, 33(15):1233–1236, 2007.

[127] Thomas Soddemann, Burkhard Dünweg, and Kurt Kremer. Dissipative particle dynamics: A useful thermostat for equilibrium and nonequilibrium molecular dynamics simulations. *Physical Review Letters E*, 68:046702, Oct 2003.

[128] Maziar Derakhshandeh and Savvas G. Hatzikiriakos. Flow-induced crystallization of high-density polyethylene: the effects of shear and uniaxial extension. *Rheologica Acta*, 51(4):315–327, 2012.

[129] G. Marrucci and N. Grizzuti. The free energy function of the instabilities in stress relaxation. *Journal of Rheology (1978-present)*, 27(5):433–450, 1983.

[130] Evangelos Manias. *A computer simulation study nanorheology of strongly confined molecular fluids*. PhD thesis, State University of Groningen The Netherlands, 1995.

[131] G. H. Peters and D. J. Tildesley. Computer simulation of the rheology of grafted chains under shear. *Physical Review E*, 52:1882–1890, Aug 1995.

[132] Tan Hongge, Miao Bing, and Dadong Yan. Conformation-assisted fluctuation of density and kinetics of nucleation in polymer melts. *The Journal of Chemical Physics*, 119(5):2886–2891, 2003.

[133] Jian Qin and Scott T. Milner. Counting polymer knots to find the entanglement length. *Soft Matter*, 7:10676–10693, 2011.

[134] Robert S. Hoy, Katerina Foteinopoulou, and Martin Kröger. Topological analysis of polymeric melts: Chain-length effects and fast-converging estimators for entanglement length. *Physical Review E*, 80:031803, Sep 2009.

[135] Gopinath Subramanian and Sachin Shanbhag. On the relationship between two popular lattice models for polymer melts. *The Journal of Chemical Physics*, 129(14):144904, 2008.

[136] M. Tanaka, K. Iwata, and N. Kuzuu. High-precision computer simulations of entangled polymer chains: 1. determination of entanglement parameters of bond-fluctuation model. *Computational and Theoretical Polymer Science*, 10 (3–4):299 – 308, 2000.

[137] J. M. G. Cowie. *Polymers: Chemistry and Physics of Modern Materials*. Chapman & Hall, 1991.